



**HAL**  
open science

# Growth and characterization of single crystals across the BaTiO<sub>3</sub>-CaTiO<sub>3</sub>-BaZrO<sub>3</sub> phase diagram for lead-free piezoelectrics

Cong Xin

► **To cite this version:**

Cong Xin. Growth and characterization of single crystals across the BaTiO<sub>3</sub>-CaTiO<sub>3</sub>-BaZrO<sub>3</sub> phase diagram for lead-free piezoelectrics. Material chemistry. Université de Bordeaux, 2018. English. NNT: 2018BORD0211 . tel-01941079

**HAL Id: tel-01941079**

**<https://theses.hal.science/tel-01941079>**

Submitted on 30 Nov 2018

**HAL** is a multi-disciplinary open access archive for the deposit and dissemination of scientific research documents, whether they are published or not. The documents may come from teaching and research institutions in France or abroad, or from public or private research centers.

L'archive ouverte pluridisciplinaire **HAL**, est destinée au dépôt et à la diffusion de documents scientifiques de niveau recherche, publiés ou non, émanant des établissements d'enseignement et de recherche français ou étrangers, des laboratoires publics ou privés.



PhD-FSTC-2018-74

The Faculty of Sciences, Technology  
and Communication

N° 21528570

The Chemical Sciences Doctoral School

## DISSERTATION

Defense held on 07/11/2018 in Belvaux

to obtain the degree of

DOCTEUR DE L'UNIVERSITÉ DU LUXEMBOURG

EN PHYSIQUE

AND

DOCTEUR DE L'UNIVERSITÉ DE BORDEAUX

EN PHYSICO-CHEMIE DE LA MATIÈRE CONDENSÉE

by

Cong Xin

Born on 8 March 1989 in Shijiazhuang (China)

GROWTH AND CHARACTERIZATION OF  
SINGLE CRYSTALS ACROSS THE  $\text{BaTiO}_3$ -  
 $\text{CaTiO}_3$ - $\text{BaZrO}_3$  PHASE DIAGRAM FOR  
LEAD-FREE PIEZOELECTRICS

## Dissertation defense committee:

Prof. Dr. Jens KREISEL, dissertation supervisor

*Professor, University of Luxembourg*

Dr. Philippe VEBER, co-supervisor

*Research Engineer, Institut Lumière Matière*

Dr. Mario MAGLIONE

*Research Director, Institut de Chimie de la Matière Condensée de Bordeaux*

Dr. Mael GUENNOU, Chairman

*Researcher, Luxembourg Institute of Science and Technology*

Prof. Dr. Isabelle MONOT-LAFFEZ, Deputy Chairman

*Professor, University of Tours*

Prof. Dr. Krystian ROLEDER

*Professor, University of Silesia*

---



## Abstract

Solid solutions belonging to  $\text{BaZrO}_3\text{--BaTiO}_3\text{--CaTiO}_3$  (BCTZ) pseudo-ternary system are promising candidates for lead-free piezoelectrics. This thesis aims at growing and characterizing various single crystals of the BCTZ system: the end members  $\text{BaZrO}_3$  and  $\text{CaTiO}_3$  as well as  $\text{Ba}_{1-x}\text{Ca}_x\text{Ti}_{1-y}\text{Zr}_y\text{O}_3$  solid solution compounds with zirconium (Zr) and calcium (Ca) contents close to  $\text{Ba}(\text{Zr}_{0.2}\text{Ti}_{0.8})\text{O}_3\text{-50}(\text{Ba}_{0.7}\text{Ca}_{0.3})\text{TiO}_3$  composition (BZT-50BCT) where high piezoelectric performances are expected.

$\text{CaTiO}_3$  and  $\text{BaZrO}_3$  single crystals were both grown from high temperature solution by the flux method and from the melt by the optical floating zone technique. In the case of  $\text{CaTiO}_3$  grown with a mirror furnace at  $1975^\circ\text{C}$ , aluminum (Al), magnesium (Mg) and barium (Ba) as main impurities were detected. The Raman spectra of  $\text{CaTiO}_3$  are in good agreement with the spectra referenced in the literature. The growth of  $\text{BaZrO}_3$  was more challenging because of its very high melting point ( $2700^\circ\text{C}$ ).  $\text{BaB}_2\text{O}_4$  flux was successfully used to produce  $150\text{-}200\ \mu\text{m}$ -sized  $\text{BaZrO}_3$  crystals at half its melting point ( $1350^\circ\text{C}$ ) and bulk centimeter-sized  $\text{BaZrO}_3$  boules were grown from the melt. Sr, Hf, Ca and Ti were detected by GDMS and SIMS as main impurities in the range of  $0.3\text{-}0.5\ \text{at.}\%$ . The optical band gap is found to be  $\sim 4.8\ \text{eV}$  and indicates the high quality of the  $\text{BaZrO}_3$  crystals grown with mirror furnace. Low temperature dielectric properties of  $\text{BaZrO}_3$  are displayed and confirmed the absence of structural phase transition. Raman investigations reveal that even though  $\text{BaZrO}_3$  does not have any phase transition at low temperatures, it exhibits a high-pressure phase transition from cubic to tetragonal at  $11\ \text{GPa}$  at room temperature.

In the second part, BCTZ centimeter-sized single crystals have been successfully grown by the top seeded solution growth technique. Ca and Zr content profiles throughout the as-grown boules indicate that their effective segregation coefficients are highly dependent on their initial concentration in the liquid solution. Concentrations evolve substantially during the crystal growth, making the BCTZ crystal growth a tricky issue when a narrow compositions range is targeted, as in the vicinity of the phase convergence region. Furthermore, spinodal decomposition was observed, indicating the coexistence of two solid

---

solutions with close compositions in BCTZ crystals. Dielectric and piezoelectric properties were measured for some crystals, which were found to display a variety of behavior from relaxor to pure ferroelectric. In addition, an abnormal double-like PE hysteresis loop was observed, that was associated to an irreversible effect disappearing upon poling.

---

## Résumé

Les solutions solides appartenant au système quasi-ternaire  $\text{BaTiO}_3\text{-CaTiO}_3\text{-BaZrO}_3$  (BCTZ) sont des candidates prometteuses pour les piézoélectriques sans plomb. Ce travail de thèse expérimental est consacré à la cristallogénèse et à la caractérisation de différents monocristaux dans le système BCTZ :  $\text{BaZrO}_3$ ,  $\text{CaTiO}_3$  ainsi que les solutions solides  $\text{Ba}_{1-x}\text{Ca}_x\text{Ti}_{1-y}\text{Zr}_y\text{O}_3$  présentant des teneurs en zirconium (Zr) et en calcium (Ca) proches de celles de la composition  $\text{Ba}(\text{Zr}_{0.2}\text{Ti}_{0.8})\text{O}_3\text{-}50(\text{Ba}_{0.7}\text{Ca}_{0.3})\text{TiO}_3$  (BZT-50BCT) où les performances piézoélectriques sont exacerbées.

Les monocristaux de  $\text{CaTiO}_3$  et de  $\text{BaZrO}_3$  ont été obtenus à la fois depuis une solution à haute température par la méthode du flux et à partir de leur phase fondue par la technique de la zone flottante optique. Dans le cas de  $\text{CaTiO}_3$  obtenu dans un four à image à  $1975^\circ\text{C}$ , l'aluminium (Al), le magnésium (Mg) et le baryum (Ba) ont été détectés comme étant les principales impuretés. Les spectres Raman de  $\text{CaTiO}_3$  sont en bon accord avec les spectres référencés dans la littérature. La croissance cristalline de  $\text{BaZrO}_3$  est beaucoup plus difficile à cause de son point de fusion très élevé ( $2700^\circ\text{C}$ ). Le flux  $\text{BaB}_2\text{O}_4$  a été utilisé avec succès pour faire croître des cristaux d'environ  $150\text{-}200\mu\text{m}$  à  $1350^\circ\text{C}$ , soit à la moitié de son point de fusion. Des boules de  $\text{BaZrO}_3$  de taille centimétrique ont également été obtenues à partir de la phase fondue en four à image. Les impuretés majoritaires telles le strontium (Sr), l'hafnium (Hf), le calcium (Ca) et le titane (Ti) ont été détectées par GDMS et SIMS dans une gamme de concentration atomique de  $0.3\text{-}0.5\%$ . L'énergie de gap optique est d'environ  $4,8\text{ eV}$  et souligne la grande qualité des cristaux de  $\text{BaZrO}_3$  obtenus en four à image. Les propriétés diélectriques à basse température de  $\text{BaZrO}_3$  confirment l'absence de transition de phase structurale. Les études de Raman révèlent que même si  $\text{BaZrO}_3$  n'a pas de transition de phase à basse température, il présente une transition de phase cubique-quadratique sous haute pression à  $11\text{ GPa}$  à température ambiante.

Dans la deuxième partie de cette thèse, des monocristaux centimétriques de BCTZ ont été obtenus avec succès par la croissance en flux. Les profils de concentrations en Ca et Zr le long des boules indiquent que leurs coefficients effectifs de ségrégation dépendent

---

fortement de leur concentration initiale dans la solution liquide. Ceux-ci évoluent considérablement au cours du processus de cristallogénèse, rendant ainsi la croissance de BCTZ très délicate en vue d'obtenir des compositions constantes et proches de celles de la région de convergence de phases. De plus, une décomposition spinodale a été mise en évidence, indiquant la coexistence de deux solutions solides de compositions proches au sein des cristaux de BCTZ. Les propriétés diélectriques et piézoélectriques des cristaux obtenus ont été déterminées et présentent des caractéristiques allant du ferroélectrique classique au relaxeur. Les mesures diélectriques montrent notamment une double boucle d'hystérésis (PE) anormale qui disparaît après polarisation.

---

## Acknowledgements

The PhD work presented has been carried out with collaborations between the Institute de Chimie de la Matière Condensée de Bordeaux (ICMCB) and Luxembourg Institute of Science and Technology (LIST). First of all, I would like to express my sincere appreciation to Prof. Jens Kreisel and Prof. Mario Maglione for providing the chance to work on this project and continues both in academic and scientific supports with a lot of helps during my PhD.

A very special thanks goes to my two supervisors, Dr. Philippe Veber and Dr. Mael Guennou. I am grateful to my supervisor Dr. Philippe Veber for his great support and valuable comments to my work. All the work of crystal growth was finished under his guidance. I am also grateful to my supervisor Dr. Mael Guennou for his excellent supervision. His insight and complementary perspective as a physicist have been very important to me. More than that, they helped a lot to correct my thesis, paper even posters.

I would like to thank Dr. Daniel Rytz for providing several perovskite crystals. I also want to acknowledge Mr. Eric Lebraud for his support on XRD measurements, Dr. Michel Lahaye on chemical analysis and Dr. Michaël Josse on dielectric measurements. I would like to thank everyone in ICMCB, in particular the entire colleagues in the crystal growth team, Dr. Matias Velazquez, Dr. Stanislav Pechev, Dr. Mythili Prakasam, Mr. Viraphong Oudomsack, Dr. Gabriel Buşe and Dr. Hairui Liu.

I would like to thank Dr. Constance Toulouse, for her continue supports and a lot of helps with Raman measurements. I also want to acknowledge Dr. Nathalie Valle for her support on SIMS measurements, Mr. Jean-Luc Biagi on EDX measurements and Dr. Torsten Granzow on dielectric measurements. A very special thank goes to all members of FMT group for all assistance.

The next acknowledgement goes to Dr. Raphaël Haumont and Dr. Romuald Saint-Martin for the one week very enjoyable days for growing several single crystals at ICMMO. A

---

special thank goes to Prof. Geetha Balakrishnan and Dr. Monica Ciomaga-Hatnean for collaborating on the growth of BaZrO<sub>3</sub> single crystals, who supports our work greatly. I would like to thank Dr. Alain Maillard for providing high-purity BBO powders.

I am so happy to meet all these smart and lovely people in both countries, they make me growing quickly.

Lastly, I also would like to thank European Union's team. This project has received funding from the European Union's Horizon 2020 research and innovation programme under the Mario Sklodowska-Curie grant agreement No 641640.

Finally, I would like to thank my family for their encouragement and support.

---

# Table of contents

1 Introduction.....	1
2 Theory and Literature Review .....	4
2.1 Fundamentals of Ferroelectrics .....	4
2.1.1 Dielectrics .....	4
2.1.2 Piezoelectricity.....	5
2.1.3 Ferroelectricity.....	7
2.1.4 Landau Theory of Ferroelectric Phase Transitions .....	8
2.1.5 Relaxors .....	12
2.2 Fundamentals of Ferroelectric Perovskite.....	13
2.2.1 The Prototype Perovskite.....	13
2.2.2 Example of Ferroelectric Perovskites .....	15
2.2.3 The PZT Solid Solution .....	17
2.2.4 Lead-free Perovskite Piezoelectric Materials .....	18
2.2.5 The BZT-BCT System.....	20
3 Fundamentals of Crystal Growth.....	23
3.1 Crystal Growth from Melts .....	23
3.1.1 Czochralski Method.....	25
3.1.2 Arc-Melting Method .....	28
3.1.3 Skull Melting Technique.....	29
3.2 Growth from High-Temperature Solutions .....	30
3.2.1 Conventional Flux Growth Method.....	31
3.2.2 Top Seeded Solution Growth.....	33
3.3 The Floating Zone Technique .....	34
3.3.1 Optical Floating Zone Technique .....	35

3.3.2 Laser-Heated Pedestal Growth .....	37
3.4 Grown of Perovskite-Type Oxides.....	39
4 Characterization Techniques.....	46
4.1 Structural Characterization.....	46
4.1.1 X-Ray Diffraction .....	46
4.1.2 Laue X-ray Diffraction and Orientation of Single Crystals.....	48
4.2 Chemical Analysis.....	51
4.2.1 Glow Discharge Mass Spectrometry .....	51
4.2.2 Electron Probe Micro-Analysis.....	52
4.2.3 Energy Dispersive X-ray Analysis.....	53
4.2.4 Secondary Ion Mass Spectrometry .....	53
4.3 UV-Visible Spectroscopy.....	54
4.4 Electrical Characterization .....	55
4.4.1 Dielectric Measurement.....	55
4.4.2 Ferroelectric Hysteresis Loop .....	56
4.4.3 Electrical Poling and Piezoelectric Measurement.....	58
4.5 Raman Spectroscopy .....	59
5 Crystal Growth and Characterization of CaTiO <sub>3</sub> .....	62
5.1 Crystal Growth .....	62
5.1.1 Crystal Growth by Flux Method.....	62
5.1.2 Crystal Growth by Optical Floating Zone Furnace.....	63
5.2 Structural Analysis .....	66
5.3 Chemical Analysis.....	67
5.4 Raman Study of a CaTiO <sub>3</sub> Single Crystal .....	69
5.5 Conclusion.....	71

6 Crystal Growth and Characterization of BaZrO <sub>3</sub> .....	72
6.1 Crystal Growth .....	72
6.1.1 Crystal Growth by the Flux Method .....	72
6.1.2 Crystal Growth by the Optical Floating Zone Technique.....	79
6.2 Chemical Analysis.....	80
6.2.1 Energy Dispersive X-ray Analysis.....	80
6.2.2 Glow Discharge Mass Spectrometry Analysis .....	81
6.2.3 Secondary Ion Mass Spectrometry Analysis .....	82
6.3 Physical Properties .....	83
6.3.1 Optical Properties.....	83
6.3.2 Dielectric Properties.....	85
6.3.3 Raman Spectroscopy Analysis.....	87
6.4 Conclusion.....	89
7 Growth and Characterization of BCTZ Crystals .....	90
7.1 Crystal Growth of BCTZ Crystals .....	90
7.1.1 Growth by Top-Seeded Solution Growth Technique .....	90
7.1.2 Initial Compositions and Crystals Growth Results .....	92
7.1.3 Distribution of Elements and Effective Segregation Coefficients .....	95
7.1.4 Periodical Fluctuations of Composition.....	102
7.2 Dielectric and Electromechanical Properties .....	103
7.3 Double Hysteresis Loop in BCTZ Crystal .....	108
7.4 Optical Birefringence .....	110
7.5 Conclusion.....	112
8 Conclusion and Prospects .....	113
References.....	116



# 1 Introduction

---

The piezoelectric material  $\text{Pb}(\text{Zr}_x\text{Ti}_{1-x})\text{O}_3$  (PZT) was discovered in the second half of the 1950's [1, 2] with high piezoelectric response compared to  $\text{BaTiO}_3$ , which was before the record piezoelectric material, including hydrogen-bonded salts. Today, PZT is still one of the most widely used piezoelectric materials in high-performance electromechanical applications [3, 4]. Unfortunately, lead is a heavy metal with a well-known toxicity, e.g. exposure to lead contaminates the brain and central nervous system and can cause convulsions and be lethal. [5]. During the past two decades, environmental protection has significantly gained in awareness and the toxicity of lead-based compounds has been legislated in many regions, such as in Europe through the WEEE (Waste Electrical and electronic Equipment) and REACH (Registration, Evaluation, Authorization and Restriction of Chemicals) directives [6-8], which requires to replace Pb by more environment-friendly Pb-free substitutes. Unfortunately, only few Pb-free materials have been found so far that can compete with the piezoelectric performances of PZT.

The piezoelectric properties of PZT are maximal in a narrow composition range called the Morphotropic Phase Boundary, MPB, where a competition takes place between two different crystal structures: tetragonal on the Ti-rich side vs. rhombohedral on the Zr-rich side. At the MPB, the delicate balance between different possible states gives rise to enhanced responses (dielectric, elastic, piezoelectric) and results in complex structural properties, some of which are still debated today. This scenario is also realized in other lead-based systems, such as  $\text{Pb}(\text{Mg}_{2/3}\text{Nb}_{1/3})\text{O}_3$ - $x\text{PbTiO}_3$  and  $\text{Pb}(\text{Zn}_{2/3}\text{Nb}_{1/3})\text{O}_3$ - $\text{PbTiO}_3$  single crystals where the highest piezoelectric coefficients to date have been measured [9]. The search for lead-free piezoelectrics has been largely inspired by this general picture, and many solid solutions have been explored where such a competition was considered likely to occur:  $\text{Na}_{1/2}\text{Bi}_{1/2}\text{TiO}_3$ - $x\text{BaTiO}_3$ ,  $(\text{K},\text{Na})\text{NbO}_3$  and  $\text{Na}_{1/2}\text{Bi}_{1/2}\text{TiO}_3$ - $(\text{K},\text{Bi})\text{TiO}_3$  etc. These emerging materials are, however, still far from substituting the current commercial PZT due to the lower piezoelectric properties of those new lead-free materials [10, 11].

Recently, a very large piezoelectric response with  $d_{33}$  up to 620 pC.N<sup>-1</sup> has been reported by Liu and Ren [12] for a ceramic system with the chemical formula Ba(Ti<sub>0.8</sub>Zr<sub>0.2</sub>)O<sub>3</sub>-(Ba<sub>0.7</sub>Ca<sub>0.3</sub>)TiO<sub>3</sub> (BCTZ). The authors also predicted that a single crystal of this system may reach a giant piezoelectric coefficient up to 1500 pC.N<sup>-1</sup>. This has not yet been confirmed experimentally. During the past decade, it has been recognized that the phase diagram and instabilities of BCTZ and thus the origin of the outstanding features of this system are different from those of PZT, but the understanding of this difference remains poorly understood.

Most literature work focuses on ceramics to characterize the piezoelectric performance of this system [12-14]. To our knowledge, there are only few studies on single crystals [15-18]. Indeed, regarding the past works performed on lead-based piezoelectrics [9, 19, 20], it is of a major importance to consider single crystals in order to understand the microscopic origins of BCTZ piezoelectric properties, such as phase coexistence, local compositions fluctuations and polarization flexibility. For this purpose, regarding the optimization of the electromechanical response in BCTZ system, past work on lead-based single crystal growth encouraged us to explore the single crystal growth of BCTZ compounds.

This thesis aims at growing and characterizing various single crystals of the BaTiO<sub>3</sub>-CaTiO<sub>3</sub>-BaZrO<sub>3</sub> system: the end members BaZrO<sub>3</sub> and CaTiO<sub>3</sub> as well as Ba<sub>1-x</sub>Ca<sub>x</sub>Ti<sub>1-y</sub>Zr<sub>y</sub>O<sub>3</sub> solid solution compounds with various zirconium (Zr) and calcium (Ca) contents close to the Ba(Zr<sub>0.2</sub>Ti<sub>0.8</sub>)O<sub>3</sub>-50(Ba<sub>0.7</sub>Ca<sub>0.3</sub>)TiO<sub>3</sub> composition (BZT-50BCT) where high piezoelectric performances are expected. Hence, the main objective of this work is to pave the way towards a better understanding of the microscopic mechanisms able to produce a large electromechanical response in the BCTZ system.

In the first part of this work (chapter 2), a brief review on the theoretical background about dielectrics, piezoelectrics and ferroelectrics is presented. The classical perovskite-type structure with several examples and the most widely used piezoelectric system with Pb-based and further lead-free piezoelectric systems are introduced. In chapter 3, the crystal growth techniques used during this work and their particular features for BCTZ related

compounds growth are explained. Moreover, a bibliography study presents an exhaustive list of various perovskite-type crystals that have been grown from various techniques over several decades. Crystal characterization through chemical, structural, optical and electrical experimental techniques are presented in chapter 4.

In chapter 5, the growth of  $\text{CaTiO}_3$  by two techniques (flux method and optical floating zone technique) is presented. Chemical analysis by Glow Discharge Mass Spectrometry (GDMS) is displayed. A Raman study is also presented in order to compare our results with those of the literature.

$\text{BaZrO}_3$  growth attempts are presented in chapter 6 through two techniques never reported so far for this material: flux method and optical floating zone technique. Particular endeavors were devoted to the growth and the characterization of this compound in order to achieve the measurements of its intrinsic properties aiming at a better fundamental understanding of its influence on the piezoelectric properties of the BCTZ solid solution. Hence, we present a detailed study of its chemical and physical properties. Energy Dispersive X-ray (EDX), Glow Discharge Mass Spectrometry (GDMS) and Secondary Ion Mass Spectrometry (SIMS) are investigated. Subsequently, UV-visible spectroscopy, dielectric properties and Raman spectroscopy are also studied.

In the last part of this work (chapter 7), the growth of BCTZ single crystals is finally addressed. Relationship between the initial liquid concentration for both Ca and Zr elements and their effective segregation coefficient are discussed. The dielectric properties, piezoelectric coefficients and optical birefringence of some single crystals with compositions close to BZT-50BCT are presented.

## 2 Theory and Literature Review

---

### 2.1 Fundamentals of Ferroelectrics

---

In this section, an introduction is given to the theoretical background on dielectrics, piezoelectrics, ferroelectrics, Landau theory of ferroelectric phase transitions and relaxors.

#### 2.1.1 Dielectrics

---

A dielectric is an insulator or nonconductor of electricity. When an electric field is applied to a dielectric material, positive charges are displaced in the direction of the electric field and negative charges are shifted in the opposite direction simultaneously, thus generating a polarization. In a first approximation, the polarization  $\vec{P}$  of a dielectric material is proportional to the strength of the electric field  $\vec{E}$  and is given by:

$$\vec{P} = \varepsilon_0 \chi_e \vec{E} \quad (2.1)$$

where  $\chi_e$  is the dielectric susceptibility and  $\varepsilon_0 = 8.854 \times 10^{-12} \text{ F.m}^{-1}$  is known as the dielectric permittivity of vacuum.

The susceptibility of a medium is related to relative permittivity  $\varepsilon_r$  expressed as:

$$\varepsilon_r = 1 + \chi_e \quad (2.2)$$

The overall surface charge density is induced by the applied field in the material and is obtained from by the dielectric displacement defined as:

$$\vec{D} = \varepsilon_0 \vec{E} + \vec{P} = \varepsilon_0 (1 + \chi_e) \vec{E} = \varepsilon_0 \varepsilon_r \vec{E} \quad (2.3)$$

If a time-harmonic electrical field is applied to an atom, the relative permittivity of the medium is described by a complex frequency-dependent quantity defined as:

$$\varepsilon_r(\omega) = \varepsilon_r'(\omega) - j\varepsilon_r''(\omega) \quad (2.4)$$

where  $\varepsilon_r'$  is the real part, known as the dielectric constant.  $\varepsilon_r''$  is the imaginary part, known as the dielectric loss factor,  $\omega = 2\pi f$ . In addition, the ratio  $\varepsilon_r''/\varepsilon_r'$  is called the loss tangent ( $\tan\delta$ ).

Experimentally, a sample can be considered as a parallel plate capacitor. If the capacitance ( $C$ ) and dielectric loss of samples are measured, the dielectric constant, i.e. the real part  $\varepsilon'$ , can be calculated, according to:

$$\varepsilon' = \frac{C \cdot d}{\varepsilon_0 \cdot A} \quad (2.5)$$

where  $C$  is the capacitance,  $d$  is the sample thickness,  $A$  is the electrode area and  $\varepsilon_0$  is the vacuum permittivity.  $\varepsilon_0 = 8.854 \times 10^{-12} \text{ F.m}^{-1}$ .

---

## 2.1.2 Piezoelectricity

---

Piezoelectrics are materials, which can be polarized by inducing electric charge at their surfaces when a mechanical stress is applied. This is called direct piezoelectric effect and it was discovered by Jacques and Pierre Curie in 1880. They also verified that materials showing this phenomenon must also show the converse piezoelectric effect with a deformation of the material when a voltage (an electric field) is applied.

The direct piezoelectric effect is described as:

$$D_i = d_{ikl}T_{kl} \quad (2.6)$$

where  $D_i$  is the electrical displacement and  $T_{kl}$  is the applied stress.

The converse piezoelectric effect is described as:

$$S_{ij} = d_{kij}E_k \quad (2.7)$$

where  $E_k$  is the applied electric field and  $S_{ij}$  is the induced strain.

Finally, taking into account both the electric field and the applied stress, linear constitutive equations of piezoelectricity are given following these two relationships:

$$\begin{cases} D_i = d_{ikl}T_{kl} + \varepsilon_{ik}^T E_k \\ S_{ij} = S_{ijkl}^E T_{kl} + d_{kij}E_k \end{cases} \quad (2.8)$$

where  $S_{ij}$  is the mechanical strain,  $D_i$  is the electrical displacement,  $T_{kl}$  is the mechanical stress,  $E_k$  is the electric field,  $S_{ijkl}^E$  is the mechanical compliance measured at constant electric field,  $d_{ikl}$  is the piezoelectric strain coefficient, and  $\varepsilon_{ik}^T$  is the dielectric permittivity measured at zero mechanical stress.

Among the 32 crystallographic point groups describing all crystalline systems (see Fig. 2.1), the piezoelectric and other effect is by symmetry forbidden in the 11 centrosymmetric groups and the non-centrosymmetric point group 432. Crystals belonging to the 20 other non-centrosymmetric groups can exhibit a piezoelectric effect. Among the piezoelectric point groups, 10 are polar without an external applied electric field. They are designated as pyroelectric and their polarization evolves with temperature. In some pyroelectric materials, the spontaneous polarization can be reversed by an electric field. Those are known as ferroelectrics. Therefore, all ferroelectric crystals belong to one of these 10 polar point groups.

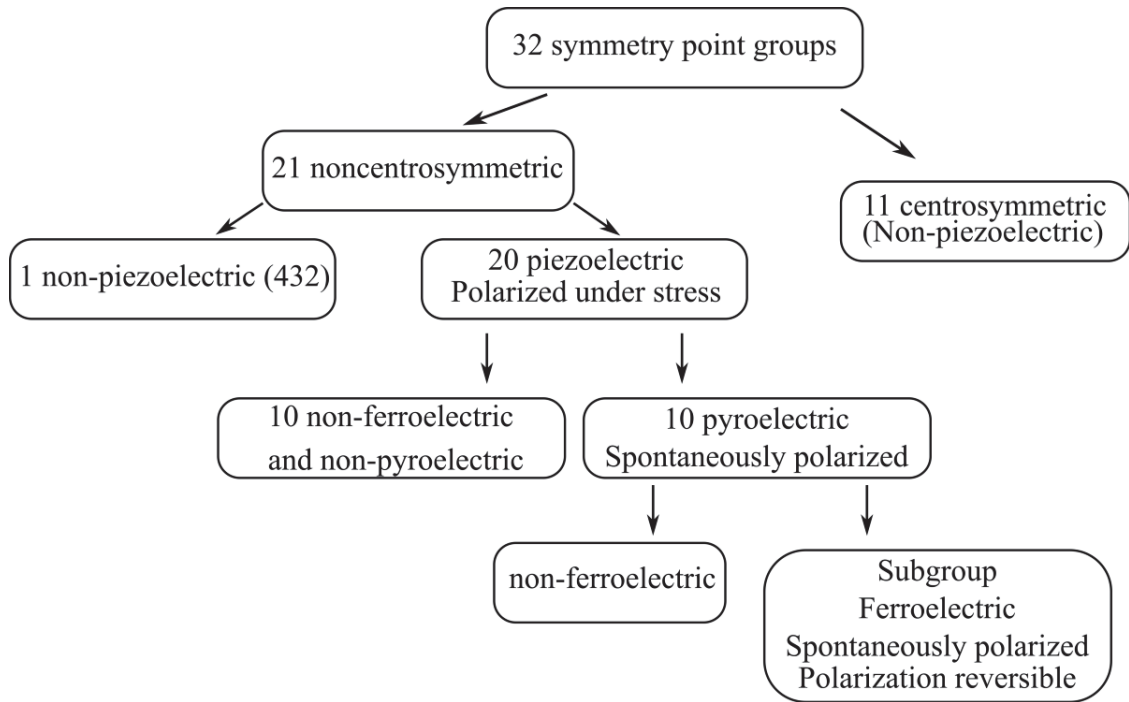


Fig. 2.1 Classification of piezoelectric and subgroups based on symmetry.

---

### 2.1.3 Ferroelectricity

---

Ferroelectricity was first discovered on a single crystal (Rochelle salt) in 1921 [21]. Ferroelectricity is a property of certain materials that exhibit a spontaneous polarization that can be reversed in the opposite direction by an applied electric field [22]. These materials show two or more discrete stable or metastable states with different nonzero electric polarization without applied electric field. Ferroelectric materials display both piezoelectric and pyroelectric properties. A typical ferroelectric hysteresis loop is presented in Fig. 2.2. When an electric field is applied to a virgin crystal, the polarization  $P$  increases linearly with increasing electric field because the applied electric field is not high enough to switch the domains oriented in the opposite direction. This linear region is shown by the curve A-B in Fig. 2.2. Further increase of the electric field leads to domain switching, polarization starts increasing rapidly until all the domains have become oriented along the direction of electric field (curve B-C). The polarization reaches a saturation level  $P_s$ . Then, when the electric field is decreased, the polarization does not return to zero as shown by

curve C-D. When the electric field becomes zero, some of these domains still remain aligned in the positive region and the crystal exhibits a remanent polarization  $P_r$ . In order to change this remanent polarization, a negative electric field has to be applied to polarize the crystal in the opposite direction. The field necessary to bring the polarization back to zero (following the curve D-F) is called coercive field  $E_c$ . Afterwards, when electric field is increased, polarization can eventually reach its maximum value  $-P_s$ , represented by the point G. Decreasing the electric field in the opposite direction reveals similar behavior to that already described previously and is presented by the curve G-H-C.

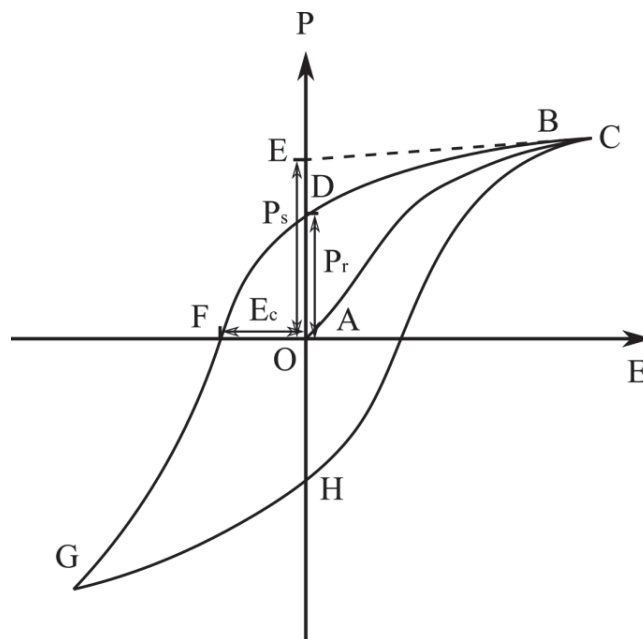


Fig. 2.2 Typical hysteresis loop of a ferroelectric material.

---

### 2.1.4 Landau Theory of Ferroelectric Phase Transitions

---

Ferroelectric phase transitions can be characterized by Landau-Ginzburg-Devonshire theory [23], close to the phase transition temperature. Landau's idea is to analytically distinguish the paraelectric and the ferroelectric phases as a function of the order parameter. It describes the two states with their own equilibrium potential (Gibbs potential) in the vicinity of the critical temperature. The Gibbs free energy  $F_P$  is written as:

$$F_P = \frac{1}{2}aP^2 + \frac{1}{4}bP^4 + \frac{1}{6}cP^6 - EP \quad (2.9)$$

where  $P$  is the order parameter, here the polarization,  $E$  is the external electric field,  $a$ ,  $b$  and  $c$  are expansion coefficients.

The equilibrium configuration is determined by finding the minima of  $F_P$ , expresses as:

$$\frac{\partial F_P}{\partial P} = 0 \quad (2.10)$$

This equation delivers an expression for the electric field  $E$  as a function of the polarization  $P$ :

$$E = aP + bP^3 + cP^5 \quad (2.11)$$

Thus, considering the paraelectric state conditions ( $\frac{\partial F_P}{\partial E} = 0, P = 0$ ), we can obtain the dielectric susceptibility:

$$\chi = \frac{\partial P}{\partial E} = \frac{1}{a} \quad (2.12)$$

Then, we assume that ' $a$ ' is written such as the following equation:

$$a = a_0(T - T_0) \quad (2.13)$$

where  $T_0$  is the phase transition temperature, i.e. the Curie temperature.

Combining the Eq. 2.12 and 2.13, we found that the dielectric susceptibility obeys a temperature dependence known as Curie-Weiss law, and is written as:

$$\chi = \varepsilon_\infty + \frac{C}{T - T_0} \quad (2.14)$$

where  $C$  is Curie constant, where  $\varepsilon_\infty$  is high temperature permittivity at least equal  $n_2$  ( $n$  is the refractive index, of the order of 2 for oxidic  $ABO_3$  perovskites).

Finally, by including the linear temperature dependence of  $a$ , the free energy can be expressed by:

$$F_P = \frac{1}{2}a_0(T - T_0)P^2 + \frac{1}{4}bP^4 + \frac{1}{6}cP^6 - EP \quad (2.15)$$

where based on literature,  $a_0$  and  $c$  are both positive in all known ferroelectrics [22, 24, 25]. If  $T > T_0$ , the energy displays one minimum that corresponds to  $P = 0$  (paraelectric). If  $T < T_0$ , two symmetric minima are obtained that corresponds to  $P \neq 0$  (ferroelectric). Fig. 2.3 displays the free energy as a function of polarization in both states. It is noticed that the sign of the coefficient  $b$  can determine transformation of free energy between these two states, but also can determine either the polarization at  $T < T_0$  develops continuously or discontinuously.

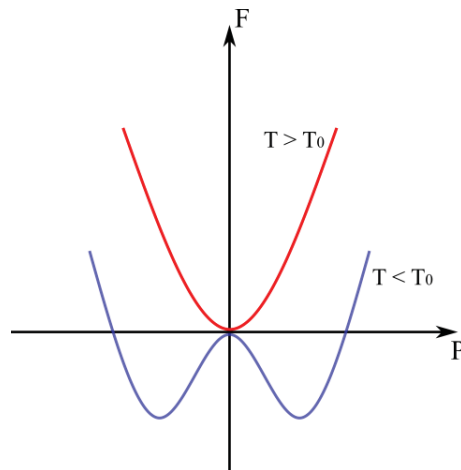


Fig. 2.3 Landau free energy as a function of polarization: in the paraelectric phase (red) and in the ferroelectric phase (blue).

In a continuous transition,  $b > 0$ , and a second-order transition occurs at  $T = T_0$ , the free energy will develop continuously from the paraelectric state to the ferroelectric state as a function of decreasing temperature, that correspond to two minima polarization  $-P_0$  and  $P_0$ . For small value of  $P_S$ , we neglect higher-order terms. The polarization can be estimated when  $E = 0$ , according to Eq. 2.11. So the result is:

$$P_0^2 = \frac{a_0}{b}(T_0 - T) \quad (2.16)$$

According to Eq. 2.15, we obtain the dielectric susceptibility with respect to  $E$ :

$$\chi = \frac{\partial P}{\partial E} = \frac{1}{a_0(T - T_0) + 3bP^2} \quad (2.17)$$

Therefore, we find that:

$$\chi = \frac{1}{a_0(T - T_0)} \quad (T > T_0) \quad (2.18)$$

$$\chi = -\frac{1}{2a_0(T - T_0)} \quad (T < T_0) \quad (2.19)$$

In Fig. 2.4 (a), we plot the spontaneous polarization  $P_0(T)$  as a function of temperature, the polarization changes continuously at the transition temperature. The dielectric susceptibility shows that it is divergent at transition temperature  $T_0$ .

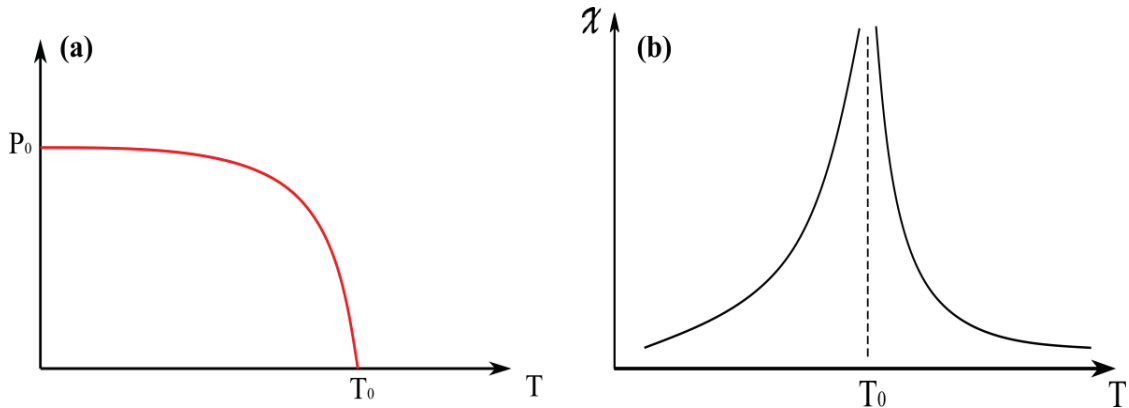


Fig. 2.4 Second-order phase transition. (a) Spontaneous polarization  $P_0(T)$  as a function of temperature. (b) The dielectric susceptibility  $\chi$ .

If the  $b < 0$  with  $c > 0$ , a first-order phase transition happens. Finding the polarization and dielectric susceptibility follows same procedure as before, but we cannot neglect the higher-order terms. The most important feature of this phase transition is that the order parameter jumps discontinuously to zero at  $T_c$  in both the spontaneous polarization and the

dielectric susceptibility at the transition point. More common examples of first-order phase transitions are found in solid-liquid transitions, as shown in Fig. 2.5.

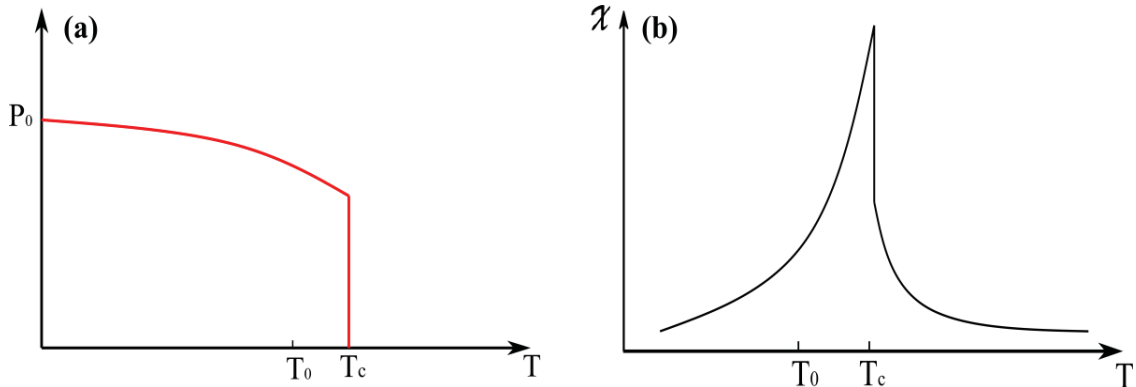


Fig. 2.5 First-order phase transition. (a) Spontaneous polarization  $P_0(T)$  as a function of temperature. (b) The dielectric susceptibility  $\chi$ .

### 2.1.5 Relaxors

Relaxor ferroelectric materials are a subgroup of ferroelectric with diffuse transition. The most well-known are lead-containing systems, such as  $\text{PbMg}_{1/3}\text{Nb}_{2/3}\text{O}_3$  (PMN) [26],  $\text{PbSc}_{1/2}\text{Ta}_{1/2}\text{O}_3$  (PST) [27] and  $(\text{Pb}_{0.92}\text{La}_{0.08})(\text{Zr}_{0.7}\text{Ti}_{0.3})\text{O}_3$  (PLZT) [28] etc., but several lead-free relaxor systems are also known, such as  $\text{BaTiO}_3$ - $\text{BaSnO}_3$  [29] and  $\text{BaTiO}_3$ - $\text{BaZrO}_3$  [30] etc. The characteristic behavior of relaxors is a broad maximum in temperature dependent of the dielectric permittivity, whose position is shifted to lower temperature as the frequency decreases. In Fig. 2.6, we show the temperature dependence of the dielectric permittivity  $\epsilon'$  of the typical relaxor ferroelectric material, PMN.

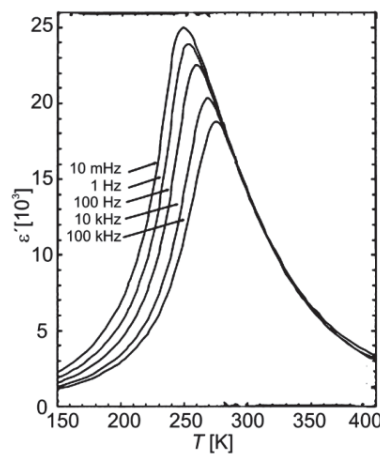


Fig. 2.6 The temperature dependence of the real part of the dielectric permittivity measured at different frequencies for a single crystal of PMN relaxor compound. From [31].

Relaxor ferroelectrics exhibit a larger  $\frac{d\varepsilon}{dT}$  than normal ferroelectrics, thus become a promising candidate as dielectric in capacitors. Moreover, relaxors have great electro-mechanical properties, especially high strains can be achieved with small hysteresis in single crystals.

---

## 2.2 Fundamentals of Ferroelectric Perovskite

---

This section gives a brief review of the prototype perovskites, ferroelectric perovskites, the solid solution  $x\text{PbZrO}_3-(1-x)\text{PbTiO}_3$  binary system, the search for lead-free ferroelectric materials and the solid solution based on  $\text{Ba}(\text{Zr,Ti})\text{O}_{3-x}(\text{Ba,Ca})\text{TiO}_3$  system.

---

### 2.2.1 The Prototype Perovskite

---

The most studied members of ferroelectrics are the perovskite oxides. The mineral perovskite  $\text{CaTiO}_3$  was firstly discovered by Gustav Rose in 1838 and named it after the Russian mineralogist Count Lev Perovski. Nowadays, perovskites are a very large family of materials with chemical formula  $\text{ABO}_3$ , where A and B represent cations, or a mixture of different cations, or vacancies, with oxygen in  $\text{O}^{2-}$  state. The physical and structural properties of the whole perovskite family are highly dependent on chemical composition and cationic ordering [22]. The space group  $Pm\bar{3}m$  is the ideal cubic perovskite structure taken as a reference structure and is adopted at high-temperature paraelectric phase for most ferroelectric perovskite oxides. The following description of the perovskite structure is taken from Rabe *et al.* [22]. Two different perovskite views are shown in Fig. 2.7. In Fig. 2.7 (a), large atom A takes place at the corners of the cube, a smaller atom B is located at the body center and oxygens in the centers of each face. Another view is presented in Fig. 2.7 (b), where the atom B is located at the corners, atom A are in the body center and oxygens are located at the midpoint of each edge. The first view highlights the  $\text{BO}_6$  oxygen octahedron, while the second view highlights the  $\text{AO}_{12}$  cuboctahedron.

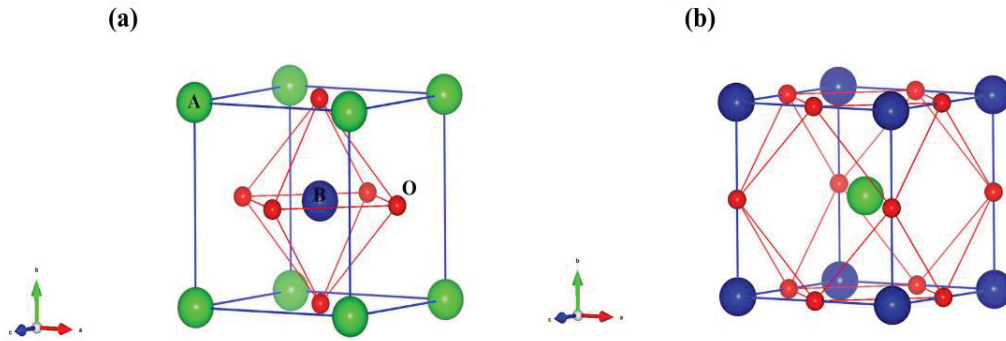


Fig. 2.7 Two different views of the unit cell of the ABO<sub>3</sub> cubic perovskite structure: (a) The atom B (blue) is located at the center surrounded by an octahedron composed of 6 oxygen atoms (red). (b) The atom A (green) is located at center with 12 oxygen first neighbors.

To classify the perovskite structure and the degree of distortion of crystal structures, the empirical rule of Goldschmidt [32] provides a relationship in between ionic radii in order to specify the ion substitutions that can occur in a crystalline structure with respect to its stability. The Goldschmidt factor  $t$  is defined as:

$$t = \frac{r_A + r_O}{\sqrt{2}(r_B + r_O)} \quad (2.20)$$

where  $r_A$ ,  $r_B$  and  $r_O$  are respectively the ionic radius of the A-site cations, B-site cations and oxygen ions. In practice, the structure can crystallize in a perovskite structure for  $0.8 < t < 1.2$ . If  $t > 1$ , the B atom is too small to fill the oxygen cage, and it may move off-center in the octahedron (displacive distortion), leading to the ferroelectric phases as found in BaTiO<sub>3</sub> [22, 33]. If the value of  $t$  is very close to 1, the cubic perovskite phase will be formed, a typical example is SrTiO<sub>3</sub> [33]. If the tolerance factor  $t$  is slightly less than one, tilting of the oxygen and rotations will be highly favored [34, 35] as for instance in the case of CaTiO<sub>3</sub> [36]. This tilting arises because the A atom is small in comparison with the space available between the oxygen octahedra, and hence, it cannot effectively bond with all 12 O atoms neighbors.

Many physical properties are related to the distortion of the ideal and cubic perovskite structure. The distortion of perovskites was studied by H.D. Megaw, A.M. Glazer and others [34, 35, 37-43], who showed how perovskite structure can be distorted. It can be classified into three main types: i)  $\text{BO}_6$  octahedral tilting. ii) Displacement of A or B cations. iii) Distortions of the  $\text{BO}_6$  octahedra units, eg. Jahn-Teller distortion. In fact, 23 simple tilts system were inventoried by Glazer in 1972 [39]. They can be distributed in 15 space groups. Additionally, he developed a new standard notation to describe the octahedra tilt of these perovskite systems.

The octahedral tilting is the most common type of distortion in the perovskite structure. Cation displacement are found in many compounds, namely in ferroelectric materials, as in  $\text{BaTiO}_3$  [44, 45]. Octahedra distortion occurs often in magnetic perovskites such as orthomanganites, orthoferrites or orthochromites. For instance,  $\text{KCuF}_3$  presents octahedra distortions even when there are no displacement or tilts [46].

---

## 2.2.2 Example of Ferroelectric Perovskites

---

The most studied ferroelectric material is barium titanate  $\text{BaTiO}_3$ . The ions valences are +2 for Ba and +4 for Ti, which perfectly balances the negative total valence of oxygen anions. The oxygen octahedron contains a Ti ion at its center. The Ba ions insure stability and neutrality of whole lattice cell, and are located at the corners of the unit cell. The ferroelectric and piezoelectric properties are dominated by the displacement of the Ti ions relative to the oxygen octahedron network.

The paraelectric cubic perovskite structure ( $Pm\bar{3}m$ ) is found at high temperature. Then  $\text{BaTiO}_3$  transforms from the cubic phase to the ferroelectric tetragonal phase ( $P4mm$ ) at 393 K. Additionally, two more phase transitions below the Curie temperature were measured by Merz [47]. One is a ferroelectric phase with orthorhombic symmetry ( $Amm2$ ) occurring at 278 K from the tetragonal phase. The last phase displays a rhombohedral ( $R3m$ ) symmetry and is found below 183 K. These results are shown in Fig. 2.8

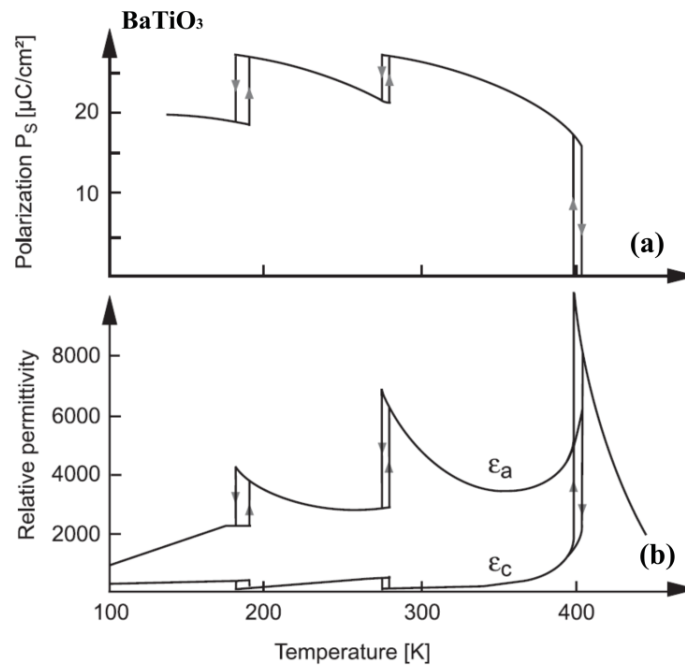


Fig. 2.8 (a) Spontaneous polarization  $P_s$  of  $\text{BaTiO}_3$  as a function of temperature. (b) The temperature dependence of permittivity in  $\text{BaTiO}_3$  [48].

The polar axis is aligned along the (001) (tetragonal), (110) (orthorhombic) and (111) (rhombohedral) directions corresponding to the direction of the atomic displacement from the cubic reference structure [49]. The commonly measured polarizations are  $33 \mu\text{C}\cdot\text{cm}^{-2}$  in rhombohedral symmetry,  $36 \mu\text{C}\cdot\text{cm}^{-2}$  in orthorhombic one and  $27 \mu\text{C}\cdot\text{cm}^{-2}$  in tetragonal one [50]. The central Ti and the O atoms undergo a relative displacement along the polar axis, which makes the structure polar and induces the dipole moment.

Another displacive type of ferroelectric material is lead titanate  $\text{PbTiO}_3$  ( $c/a=1.064$ ). It has a paraelectric to ferroelectric transition at 760 K, which is characterized by a discontinuity in the spontaneous polarization [51, 52]. It has a larger ‘tetragonality’ ( $=c/a$ ) compared to that of  $\text{BaTiO}_3$  ( $c/a=1.01$ ) [53, 54]. A polarization of about  $75 \mu\text{C}\cdot\text{cm}^{-2}$  was measured at room temperature [55]. The displacement of the Pb ions, in addition to that of Ti, is substantial and contributes significantly to the spontaneous polarization [55].

---

### 2.2.3 The PZT Solid Solution

---

The solid solution  $x\text{PbZrO}_3-(1-x)\text{PbTiO}_3$  is one of the most important ferroelectric and piezoelectric materials [56]. Its chemical formula can be also written as  $\text{Pb}(\text{Zr}_x\text{Ti}_{1-x})\text{O}_3$  (with  $0 < x < 1$ ). PZT has the perovskite structure, where  $\text{Pb}^{2+}$  is a divalent A cation that occupies the A site.  $\text{Zr}^{4+}$  or  $\text{Ti}^{4+}$  are tetravalent B cations that occupy the B site. The properties of PZT solid solutions were first described by Shirane and Suzuki [1, 2, 57], and later reviewed by Sawaguchi [58]. The phase diagram of the PZT solid solution is shown in Fig. 2.9.

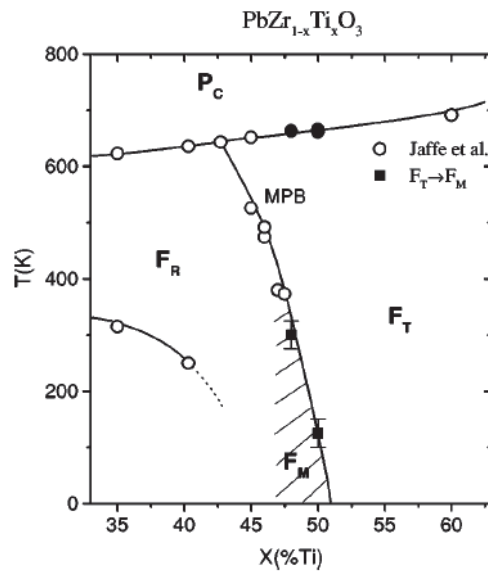


Fig. 2.9 Phase diagram of the  $\text{PbTiO}_3$ - $\text{PbZrO}_3$  solid solution showing the morphotropic phase boundary between rhombohedral and tetragonal phases. From [59].

Although  $\text{PbZrO}_3$  is antiferroelectric, the solid solution with more than 10 mol.%  $\text{PbTiO}_3$  is ferroelectric. A morphotropic phase boundary (MPB) separates the  $\text{PbZrO}_3$ - $\text{PbTiO}_3$  phase diagram into two parts: a tetragonal phase region on the Ti-rich side and a rhombohedral phase on the Zr-rich side. At room temperature, this MPB boundary occurs at a molar ratio  $\text{Zr}/\text{Ti} \sim 53/47$ . In the region where Zr content lies in between 100% and 94%, an antiferroelectric distortion of the perovskite structure was observed, and the polarization is cancelled with no observable piezoelectric effect.

A breakthrough for technological applications was the discovery of very large piezoelectric effects in PZT solid solution by Jaffe *et al* in 1954 [3]. MPB compositions present anomalously high responses as a result of the high polarization flexibility: many physical properties of PZT are extremal at the MPB [3, 4, 60, 61], such as dielectric, elastic, and piezoelectric constants. There are two main descriptions of such a behavior for PZT. The first is that the monoclinic phase is composed of twinned rhombohedral or tetragonal nano-domains. In this “adaptive phase” model, the large electric-field induced strains are extrinsic and also result from switching among of the “nano-twins” component. A high domain-wall-movement explains the ease of polarization rotation. Secondly, at the MPB, monoclinic phases are responsible for large piezoelectric response, because they facilitate polarization rotation at least [62].

---

#### **2.2.4 Lead-free Perovskite Piezoelectric Materials**

---

Lead-based ferroelectrics, as the most important piezoelectric materials, are widely used in actuators, sensors and transducers due to their excellent piezoelectric properties, especially when the composition is close to the MPB [3]. However, the manufacturing of lead oxide is highly toxic and its toxicity is further enhanced due to its volatilization at high temperature during calcination and sintering, causing thus environmental pollution and serious health hazards. In terms of legislation on the EU level, recent directives put severe restrictions on the use of hazardous substances in electronic equipment [6]. According to that, European Union restricts the use of hazardous substances such as lead as well as other heavy metals [63, 64]. However, at present time, there is no substitute for PZT with equivalent properties. Therefore, researchers endeavor to develop alternative lead-free materials in order to replace lead-based materials.

There are two main families of interest for lead-free piezoelectrics, i) perovskites, i.e., BaTiO<sub>3</sub>, KNbO<sub>3</sub> or solid solutions based on these model ferroelectrics etc., ii) non-perovskites, i.e., tungsten-bronze type ferroelectrics, bismuth layer structured ferroelectrics, etc. Usually, perovskites are considered more suitable and stable for many applications.

Moreover, perovskite-based lead-free ceramics have large piezoelectric properties compared to those of non-perovskite types. For instance, perovskite-type ferroelectrics such as BaTiO<sub>3</sub> are well known as efficient lead-free piezoelectric ceramics that show relatively large piezoelectric constants. Their main drawback is a low Curie temperature for BaTiO<sub>3</sub>, and in general, the difficulties of electrical poling or low relative densities for actual piezoelectric applications [10, 63, 65].

The (K<sub>1-x</sub>Na<sub>x</sub>)NbO<sub>3</sub> solid solution (KNN) is considered as one of the most promising candidates for lead-free piezoelectric applications as alternative to PZT. It has been one of the most widely studied lead-free piezoelectric materials since early 2000 [10, 65-76]. This system displays a high Curie temperature ( $T_c > 400$  °C), which makes it capable to be used in piezoelectric applications over a wide temperature range. However, it is very difficult to fabricate efficient devices based on KNN ceramics or single crystals with accurate composition due to the strong volatility of alkali components during their elaboration processes. Recently, KNN systems modified by LiTaO<sub>3</sub> and LiSbO<sub>3</sub> have shown a significantly improved piezoelectric constant with  $T_c = 279$  °C and  $d_{33}$  up to 732 pC.N<sup>-1</sup> after oxygen annealing [74].

Bi<sub>0.5</sub>Ti<sub>0.5</sub>O<sub>3</sub> (BNT) and Bi<sub>0.5</sub>K<sub>0.5</sub>TiO<sub>3</sub> (BKT) are well known lead-free piezoelectric materials with tetragonal phase. BNT was first reported by Smolenskii *et al.* in 1960. BKT was originally synthesized by Popper *et al.* in 1957. The binary system of BNT-BKT solid solution was synthesized by Elkechai *et al.* in 1996 [77]. High piezoelectric properties can be obtained in this system close to its MPB composition due to the high number of possible spontaneous polarization directions and the coexistence of the rhombohedral and tetragonal phases at MPB [78]. The piezoelectric properties of this system was improved by adding other components, such as BaTiO<sub>3</sub> [79]. This system displays also a high Curie temperature ( $T_c > 280$  °C). Nevertheless, major drawbacks remain such as: lower piezoelectric properties compared to those of KNN and highly corrosive environment due to the presence of bismuth and alkali in the sintering temperature range [80].

## 2.2.5 The BZT-BCT System

The solid solution based on  $\text{Ba}(\text{Zr,Ti})\text{O}_3\text{-x}(\text{Ba,Ca})\text{TiO}_3$  (BZT-xBCT) was already investigated for dielectric study by McQuarrie *et al.* in 1954 [81]. Highlights of the high electromechanical properties of this system took off with the work of W. Liu and X. Ren in 2009 who reported the exceptional high piezoelectric properties of  $(\text{Ba}_{0.85}\text{Ca}_{0.15})(\text{Ti}_{0.9}\text{Zr}_{0.10})\text{O}_3$  with  $d_{33}\sim 620$  pC/N [12], within the pseudo-binary solid solution system  $(1-x)\text{Ba}(\text{Ti}_{0.8}\text{Zr}_{0.2})\text{O}_3\text{-x}(\text{Ba}_{0.7}\text{Ca}_{0.3})\text{TiO}_3$  ( $x=0.5$ ). A rhombohedral phase ( $R3m$ ) on the BZT-rich side and a tetragonal phase ( $P4mm$ ) on the BCT-rich side are present in the phase diagram [12, 82]. Initially, the phase diagram shows a Phase Convergence Region (PCR) displaying a triple point at 57 °C and  $x=0.32$  (Fig. 2.10 (a)). Several refined studies revealed an intermediate region between the rhombohedral and tetragonal phases, which is considered to be an orthorhombic phase ( $Amm2$ ) [83-85], as shown in Fig. 2.10 (b) with a characteristic quadruple point in between four phases with the same composition.

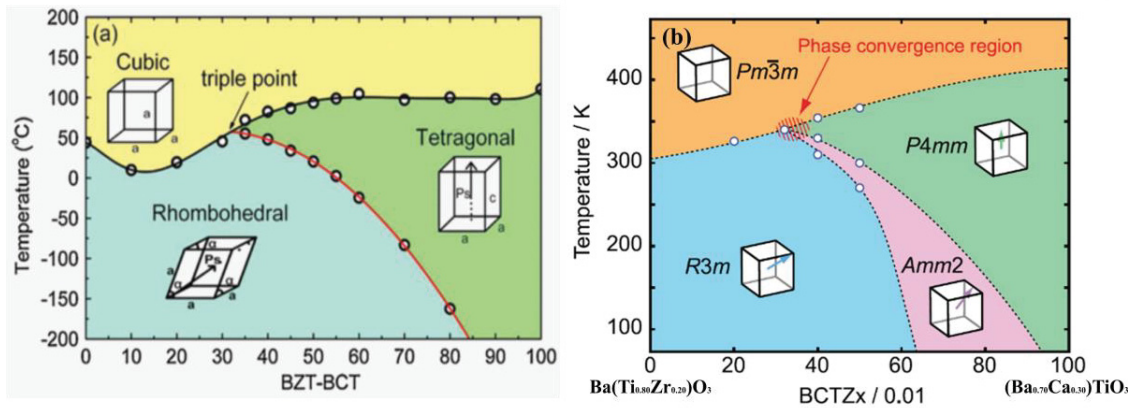


Fig. 2.10 Pseudo-binary phase diagram of the  $(1-x)\text{Ba}(\text{Ti}_{0.8}\text{Zr}_{0.2})\text{O}_3\text{-x}(\text{Ba}_{0.7}\text{Ca}_{0.3})\text{TiO}_3$  system according to (a) Liu and Ren (with triple point), from [12] and (b) Keeble *et al* (with quadruple point). The red region depicts the phase convergence region. From [86].

To the best of our knowledge, the best electromechanical properties at room temperature were reported by Wang *et al.* in 2011 for  $(\text{Ba}_{0.85}\text{Ca}_{0.15})(\text{Ti}_{0.9}\text{Zr}_{0.10})\text{O}_3$  ceramics with  $d_{33}=650$  pC.N<sup>-1</sup>,  $d_{31}=74$  pC.N<sup>-1</sup>,  $k_p=0.53$ ,  $k_t=0.38$ ,  $T_c=85$  °C,  $P_r=11.69$  μC.cm<sup>-2</sup> and  $E_c=190$

V.mm<sup>-1</sup>. It is demonstrated that the calcination and sintering temperature plays a very important role on the microstructure, dielectric and piezoelectric properties of BCTZ ceramics [14]. Acosta *et al.* studied the relationship between different regions of the phase diagram and the measured electromechanical properties [87]. It is reported that the existence of a triple/quadruple point or a general phase convergence region is not the cause of the high electromechanical properties in the BCTZ ceramics system. The phase convergence region leads only to a maximum of polarization. It is suggested that it is due to 180° domain switching and an increasing in transition temperature with electric field. On the other hand, several BCTZ single crystals have been studied since 2009. Zeng *et al.* indicated that it is difficult to obtain single crystals due to the volatilization, segregation and polycrystals occurrence during the growth [18]. BCTZ single crystals have been successfully grown with various compositions such as (Ba<sub>0.857</sub>Ca<sub>0.143</sub>)(Ti<sub>0.928</sub>Zr<sub>0.072</sub>)O<sub>3</sub> and (Ba<sub>0.953</sub>Ca<sub>0.047</sub>)(Ti<sub>0.427</sub>Zr<sub>0.573</sub>)O<sub>3</sub> by Benabdallah *et al.* [15]. It is shown that a continuous cross-over from relaxor to ferroelectric state can be achieved in BCTZ lead-free materials. Recently, excellent piezoelectric properties with d<sub>33</sub>= 496 pC.N<sup>-1</sup> and k<sub>t</sub>= 0.58 were obtained in (Ba<sub>0.794</sub>Ca<sub>0.206</sub>)(Ti<sub>0.911</sub>Zr<sub>0.089</sub>)O<sub>3</sub> polycrystalline BCTZ with mm-sized grains by Buse *et al.*[88]. A spinodal decomposition phenomenon was also observed, indicating that such behavior leads to emergence of two solid solutions of close compositions with tetragonal and orthorhombic structure. At present time, solid solution based on Ba(Zr,Ti)O<sub>3-x</sub>(Ba,Ca)TiO<sub>3</sub> (BZT-xBCT) are one of the most widely studied lead-free piezoelectric materials.

During the past decade, it has been recognized that the phase diagram and instabilities of BCTZ and thus the origin of the outstanding features of this system are different from those of PZT. This is a fundamental question that remains poorly understood. To compare with ceramics compounds, single crystals are expected to enable a better understanding of the microscopic origins of these outstanding properties, such as phase coexistence, local compositions fluctuations or polarization flexibility. For this purpose, in the scope of the optimization of the electrotechnical response in BCTZ system, past works on lead-based single crystal growth encouraged us to explore BCTZ single crystal and related compounds. Furthermore, as a global consideration, the control of stoichiometry in BCTZ system and

optimization of the piezoelectric properties to reach a giant piezoelectric response are still of interested.

## 3 Fundamentals of Crystal Growth

---

Crystal growth is a controlled phase transformation, from a solid, liquid or gaseous phase to a solid phase. The choice of a particular method for growing a desired single crystal critically depends on the physical and chemical properties of substance. Most oxide compounds with high crystallization temperatures, such as BaTiO<sub>3</sub>-type materials, are grown from either a high-temperature solution or a melt. The techniques for crystal growth may range from small and inexpensive devices to very sophisticated ones. In general, three basic steps are involved in the crystallization process [89]:

1. Achievement of solution supersaturation or melt supercooling
2. Formation of the crystal nuclei (nucleation)
3. Growth of the nuclei

In order to satisfy the demand for high quality crystals, a careful selection of the growth conditions is needed for controlling crystal features such as dislocation density, oxygen and cationic vacancies, elemental segregation and inclusion of solvent and impurities that may be present. Therefore, the effect of heating and cooling conditions must be predicted with respect to the presence of impurities on the properties of the as-grown crystal. Based on these factors, the crystal quality can be improved by choosing suitable growth parameters. In the following section, the basic crystal growth methods involving BaTiO<sub>3</sub>-based materials are presented, including: Czochralski, skull melting, conventional flux growth, floating zone crystal growth and arc-melting growth technique.

---

### 3.1 Crystal Growth from Melts

---

Crystal growth from melts is the most widely used method for the preparation of large single crystals with congruent melting. A large variety of materials has been prepared as single crystals grown from melt for many applications such as electronics and optics for

instance. The bulk crystal of a given material is grown by solidification from its own melt. It can be grown without any solvent, very efficiently with a high growth rate, from several millimeters per hour for Czochralski technique (see § 3.1.1) to millimeters per minute for Micro-Pulling Down technique [90]. The applicability of these melt growth methods requires that the materials melt without decomposition, have no polymorphic transitions, and exhibit low chemical activity or manageable vapor pressure at their melting points. In melt growth, crystallization can be carried out under oxidizing atmosphere (air, oxygen), neutral atmosphere (argon, nitrogen), reducing atmosphere (neutral gas with a hydrogen partial pressure) or in vacuum (seldom). Inappropriate combined temperature gradient and pulling rate disturbing the growth may lead to several physical and chemical defects such as growth striations due to constitutional supercooling induced by impurities.

A steady growth can be achieved when the Mullin-Sekerka criterion is fulfilled [91, 92]:

$$\frac{mC_{\infty}(1-k)v}{kD} < \frac{k_{sol}}{k_{sol} + k_{liq}} \left( \frac{dT}{dZ} \right)_{sol} + \frac{k_{liq}}{k_{sol} + k_{liq}} \left( \frac{dT}{dZ} \right)_{liq} \quad (3.1)$$

where  $m$  is the slope of the liquidus between the considered material (or solute if a solution is considered) and the dopant (or solvent),  $C_{\infty}$  is the concentration of impurities (or solvent) in the liquid,  $v$  is the growth rate,  $k_{sol}$  and  $k_{liq}$  are the thermal conductivities of the solid and liquid phases respectively,  $\left( \frac{dT}{dZ} \right)_{sol}$  and  $\left( \frac{dT}{dZ} \right)_{liq}$  are the longitudinal thermal gradients in solid and liquid phase respectively,  $D$  is the diffusion coefficient of the impurity in the liquid,  $k = \frac{n_{sol}}{n_{liq}}$  is the segregation coefficient of the impurity where  $n_{sol}$  and  $n_{liq}$  are the concentrations of impurities in the crystal and in the liquid respectively.

However, several issues of the melt growth methods can be pointed out such as difficulties to control temperature and thermal gradients, reactivity of crucible with the material, and possible difficulties to control the nucleation rate at the seed crystal. Moreover, a very high melting point ( $T > 2000$  °C) of the materials limits the use of melt growth techniques due to some defects that can arise into the as-grown crystals, such as dislocations, oxygen vacancies, thermal stress and fractures. Cation vacancies and impurity inclusions can be

observed where foreign atoms are incorporated into the crystal lattice either at a crystallographic site, or at an interstitial one. Finally, high melting point materials can exhibit a high volatilization rate during the growth process leading to vacancies and it is difficult to avoid contamination of the melt by the crucible.

---

### 3.1.1 Czochralski Method

---

The Czochralski method is one of the most widely used technique to grow large-size single crystals which are impossible to obtain by any other techniques in large quantity. It is devoted to a very large range of compounds, such as semiconductors, oxides, fluorides, etc. The technique was first developed by Jan Czochralski, a polish chemist, who published the first results of his experiments in *Zeitschrift für Physikalische Chemie* in 1918 [93]. He discovered a phenomenon never observed before: crystallization by pulling from the surface of a melt. This new technique allowed him to obtain good quality single crystals of pure metals like Sn, Pb or Zn, grown in air.

The typical steps of the Czochralski growth are depicted in Fig. 3.1. In this technique, the starting materials, which can be either a stoichiometric mixture of components, a pre-synthesized phase in powder form, or a polycrystalline chunk, is taken into a crucible and molten in a resistive or inductive heating furnace. The chemical and physical stability of the crucible in the processing environment is an important factor, and crucible must not contaminate nor stress the crystal. The crucible materials which display different chemical bonds from those of the melt are generally preferred in order to minimize their mutual chemical interactions at high temperatures as far as possible.

For example, for the growth of oxide materials crystals such as BaTiO<sub>3</sub>, KNbO<sub>3</sub> or LiNbO<sub>3</sub>, noble metals give the best compromise between chemical stability and mechanical strength. Platinum (Pt) or Iridium (Ir) crucibles are used, but their use also depends on the melting point of the oxides ( $T_m$ ). A rotating seed, cut in the appropriate crystallographic orientation, is slightly lowered and brought in contact with the melt at the center of the crucible. It is

kept at that position for some time in order to check whether the thermal equilibrium is reached or not. If the crystal starts growing very fast and becomes visible to the naked eyes, then the temperature of the melt needs to be increased. On the contrary, if the seed is melting too fast, the temperature of the melt must be decreased. In this case, the thermal equilibrium is achieved by cooling the melt until the crystallization occurs. The crystal growth starts by decreasing the temperature to values slightly below the melting point step by step as the pulling is processing. The size of the growing crystal is controlled by the temperature gradient, the pulling rate and the rotation speed. With suitable parameters, the Czochralski method can yield high quality and large single crystals with lengths greater than 1 meter in the case of silicon single crystal growth.

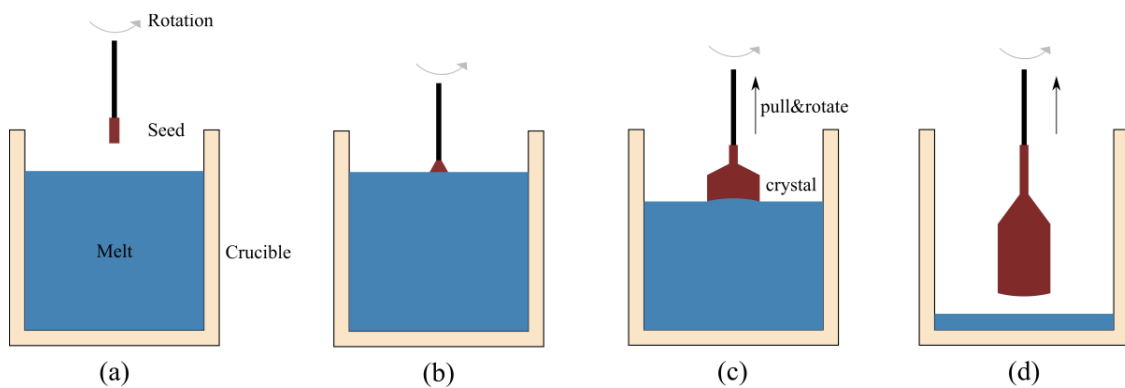


Fig. 3.1 Schematics of the Czochralski process: (a) Introduction of the seed crystal. (b) Seed contact with melt and beginning of the crystal growth. (c) Crystal pulling. (d) Crystal extraction from the melt and boule cooling.

The Czochralski growth as schematized in Fig. 3.1 has been in practice realized through the use of a system called “Czochralski Oxypuller” at ICMCB. The system has been designed and fabricated in France by Cyberstar (Fig. 3.2). The Oxypuller machine consists in a gas proof chamber containing an inductive cylindrical heating coil where the iridium crucible is set into. A Hüttinger generator of 30 kVA produces Eddy currents in the crucible about a few tens of kHz which are dissipated via Joule effect causing the temperature increasing. The rotation and pulling devices allow, respectively, a rotation speed up to 100 rpm and a translation speed in between  $0.01 \text{ mm.h}^{-1}$  and  $100 \text{ mm.min}^{-1}$ . An accurate

Sartorius electronic balance measures the weight of the growing crystal with an accuracy of 1 mg over a scale of 6 kg. The temperature of the furnace can reach up to 2100-2200 °C, which is actually the maximum temperature of use of Iridium crucible. Temperature is measured by a bi-chromatic CHINO infrared pyrometer. The crystal weight and the electrical power as a function of time are recorded via a personal computer.

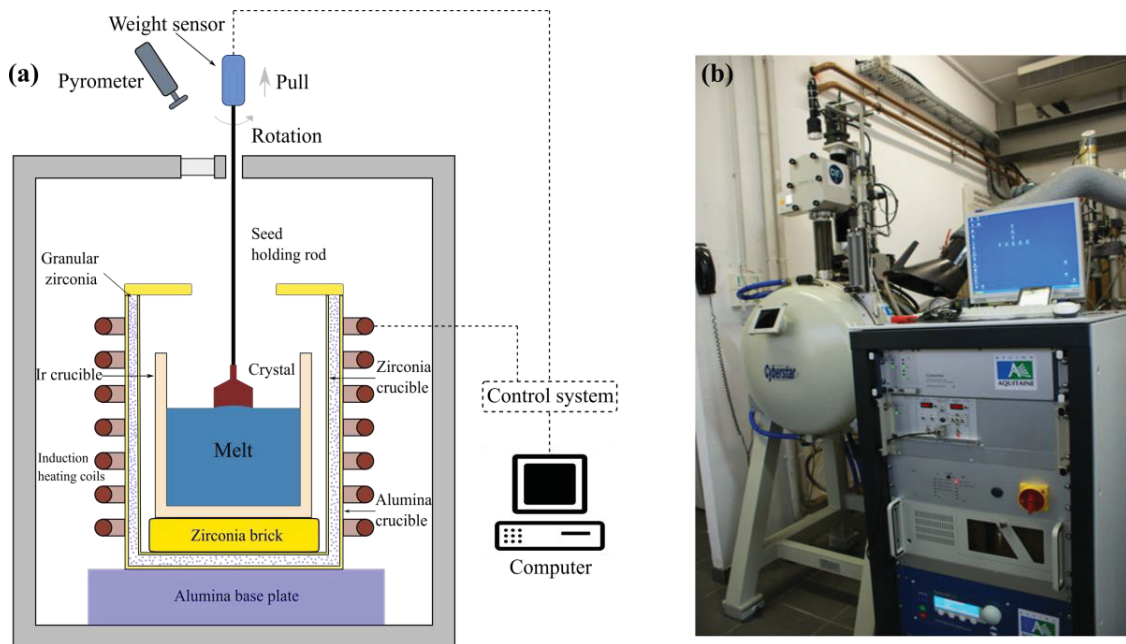


Fig. 3.2 (a) Schematic of a typical Czochralski puller system. (b) Experimental Czochralski Oxypuller from Cyberstar.

As a well-developed method for crystal growth, the Czochralski technique is important and widely used in fundamental and applied research. It is essential to investigate the growth of new materials with excellent quality as single crystals. However, this method generally involves a hot crucible, and it is often difficult to avoid contamination of the melt by the crucible material, especially if the crystal to be grown displays a high melting point. It should be mentioned that possible segregation of the elements could occur during the crystal growth of solid solutions.

---

### 3.1.2 Arc-Melting Method

---

As commonly known, high temperature processes make the hot crucible polluting the melt or the solution through diffusion of its constitutive elements (Ir), especially when the crystal to be grown displays a very high melting point. Radiation-heated or radio-frequency heated Czochralski skull-melting techniques have been developed to overcome this problem. A special furnace has also been developed which uses the technique of arc melting on a cooled crucible in order to permit the Czochralski growth without a hot crucible.

In 1968, Reed and Pollard designed a cold-crucible tri-arc-melting furnace [94]. In their approach, a polycrystalline sample was melted by three electric arcs, which were ignited between tungsten cathodes and the sample placed on a water-cooled copper anode. Since thermal contact between the hearth and the sample was poor, the sample was molten, while the anode remained cold. A sketch of a tri-arc Czochralski furnace with these features is shown in Fig. 3.3. We note that BaZrO<sub>3</sub> crystals (see § 6.1.2) purchased by Crystal Base Co.Ltd. company has been grown by this technique. Unfortunately, the company did not supply us more information about the growth process of BaZrO<sub>3</sub>.

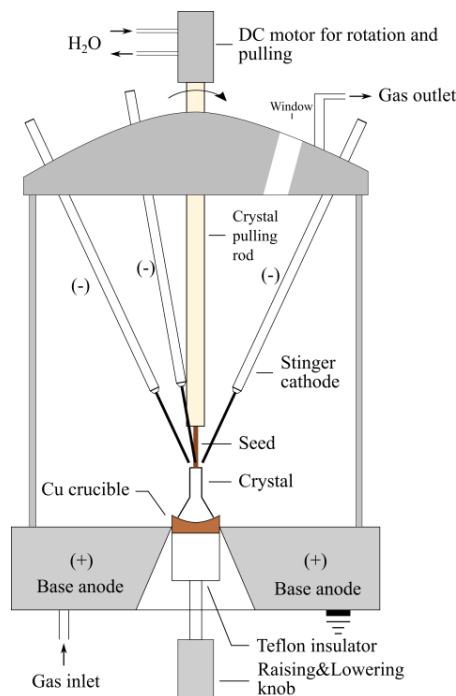


Fig. 3.3 Schematic of tri-arc Czochralski crystal growing furnace.

---

### 3.1.3 Skull Melting Technique

---

Some materials melt at very high temperatures, well above 2500 °C such as BaZrO<sub>3</sub>, and cannot be melted in any of the conventional refractory crucibles. Also, there are no commercial materials that can handle the temperature of the melt. In 1974, Russian scientists at the Lebedev Physical Institute reported [95] the development of a new process for melting large quantities of refractory materials without crucible or electrode contamination called “skull melting”. This process works with a cold crucible. It is based on two main principles: first, keeping the melt in a solid shell (skull) with a chemical composition identical to that of the melt, secondly an inductive method for heating the materials.

The skull melting technology is an industrial technology of growth and production of crystals with a high melting point, such as ZrO<sub>2</sub>-based materials [96]. The most important economic application of the skull melting technology is the production of cubic zirconia. The system consists of a high radio-frequency induction heater, which is generated from a direct current in an oscillating circuit and a water-cooled crucible. The single crystal is achieved through directional crystallization of the melt. The zirconia powder is contained in a water-cooled crucible. As the zirconia powder is electrically conductive at high temperature, the bulk of the zirconia powder is heated by absorption of radio-frequency energy and melts. When the powder has become molten, it is kept below the melting point by the water-cooled crucible, usually made of copper. After several hours, the radio-frequency heating power is slowly reduced, the zirconia powder close to the water-cooled walls remains solid, thus forming a dense sintered shell, is named “skull”. When the rest of the zirconia liquefies, to induce crystallization, the melt is lowered slowly from the heating coil, as shown in Fig. 3.4. Crystal growth begins at the base of the melt, and large zirconia columnar crystals can be produced. It should be noted that there are two important factors for growing crystals from the melt in a cold crucible: first, the power delivered in the melt should be accurately determined and correlated with the volume of the melt, and second, there is a need for proper control of the heat removal through the bottom of the cold crucible and via the surface of the melt.

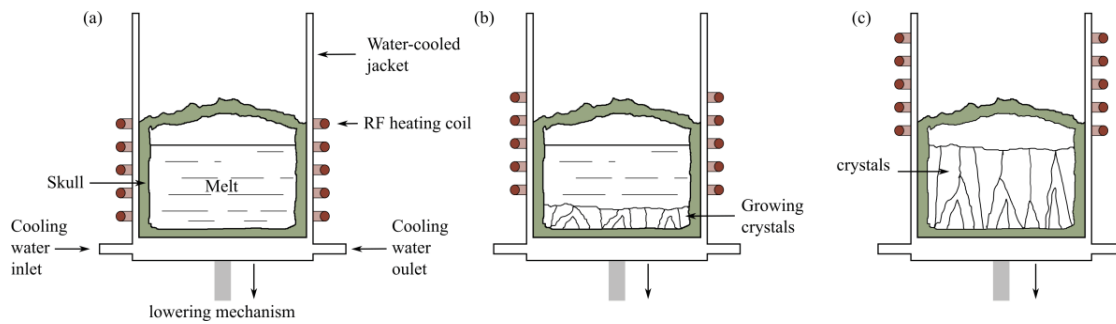


Fig. 3.4 Skull melting process: (a) Start melting and formation of the main volume of the melt. (b) Homogenization and start crystallization. (c) Crystallization of the melt.

---

### 3.2 Growth from High-Temperature Solutions

---

High-temperature solution growth is defined as a growth from solutions between 300 °C and 1800 °C. When compared with growth from the melt, crystal growth from solution produces remarkable improvements in the quality of the grown crystals, due to a much lower crystallization temperature and crystallization kinetics. Using a lower temperature during the growth process means a lower density of structural defects and less contamination in the liquid phase from the crucible. The materials to be crystallized are dissolved in a suitable solvent. Crystallization occurs when the solution becomes critically supersaturated. It is promoted either by the evaporation of the solvent, or by cooling the solution or by a transport process in which the solute is made to flow from a hotter to a cooler region. It should be noted that “*The principal advantage of using a solvent is that crystal growth occurs at a lower temperature than that required for growth from the pure melt*” [97].

Reducing the crystallization temperature is especially valuable for materials in the following categories:

- a) Materials with incongruently melting, which decomposed before melting so that crystallization from the melt results in some other phase.

- b) Materials with phase transitions. Since phase transitions may result in fracture or strain, this type of materials should be grown at temperatures below this transition.
- c) Materials with a very high vapor pressure at the melting point.
- d) Materials with very volatile elements. Volatility may induce changes in chemical composition during the process close to melting point.
- e) Highly refractory materials, such as  $\text{BaZrO}_3$ , which are very difficult to grow from the melt.

---

### 3.2.1 Conventional Flux Growth Method

---

The most widely used method is the “*flux growth*”, where the solvent (flux) is a molten salt or oxide compound, or a mixture of both. Generally, a solution is a homogeneous mixture of a solute in a solvent, where finding a suitable solvent is the key for solution-based crystal growth. The solvent must be chosen by taking into account several important factors: low melting point, high solubility for the given solute, appreciable change of solubility with temperature, low viscosity, low volatility, low reactivity with container material and no element can substitute into the desired crystal structure [98]. If the solubility is too high, it is difficult to grow bulk single crystal. If it is too low, solubility restricts the size and the growth rate of the crystals. Solubility data at various temperatures are essential to determine the level of supersaturation. That is why the solubility of the solute in the suitable solvent must be determined before starting the growth process as far as possible. Hence, the crystallization occurs by decreasing the temperature and by following liquidus curves of solute-solvent phase diagram at thermodynamically stable state until the solidus curve such as an eutectic point. Fig. 3.5 (a) presents the phase diagram of the  $\text{BaTiO}_3$ - $\text{BaB}_2\text{O}_4$  system [99] to grow  $\text{BaTiO}_3$  crystals in the melt.

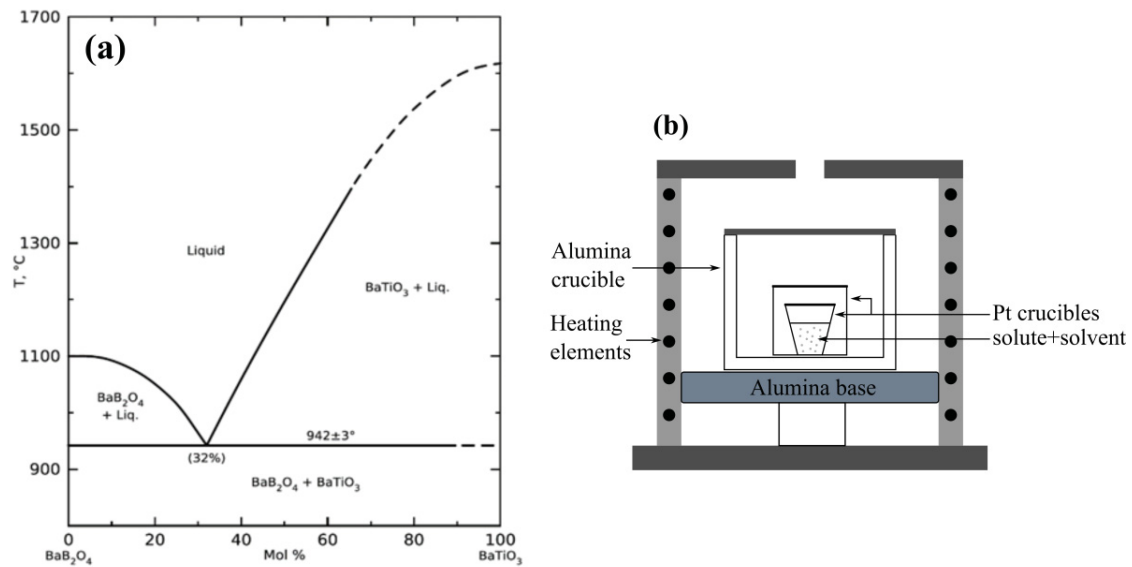


Fig. 3.5 (a) Phase diagram of the BaTiO<sub>3</sub>-BaB<sub>2</sub>O<sub>4</sub> system. (b) Schematic of the conventional setup for crystal growth by the flux method.

Fig. 3.5 (b) gives the schematic of the conventional setup for crystal growth by the flux method used for our flux growth attempts of BaZrO<sub>3</sub>. Starting raw materials as the solute mixed with a suitable solvent are loaded into a Pt crucible, covered by a lid (made of platinum) and placed into a sealed Pt crucible, then set into a sealed alumina crucible to avoid the volatilization of the solution. The solution is heated up to a temperature higher than the liquidus temperature of the solution and kept at this temperature for 24 hours in order to make the solution undersaturated, homogenous and stable. The growth process is initiated by lowering the temperature slowly, typically 0.01-1 °C.h<sup>-1</sup>, depending on the solubility of chosen material. The complete crystallization process may take from one to several weeks. It should be noticed that the as-grown crystals are not taken out of the solution then cooled down slowly, so that the crystals grown in the liquid solution.

Finally, the quality of the crystals depends on various growth parameters such as the solubility for a given molar fraction in between the solute and the solvent, the growth temperature, the temperature lowering rate, etc. These parameters have to be optimized for each attempt. In addition, it is very difficult to grow large crystals due to absence of a seed and random spontaneous nucleation at the crucible.

---

### 3.2.2 Top Seeded Solution Growth

---

The Top Seeded Solution Growth (TSSG) was first introduced by Linz *et al* in 1965 [100], and was described in detail by Belruss *et al* in 1971 [101]. It is becoming increasingly popular. The TSSG method represents an improvement of crystal growth from high temperature methodologies as it restricts and forces crystal growth only at a point of the free surface of the solution, i.e., on a crystal seed in contact with the surface of the solution that can be rotated and pulled. The main difference between TSSG and conventional flux growth method is that only one crystal grows onto a crystal seed placed in contact with the surface of the solution and it can be extracted from the solution without thermal shock.

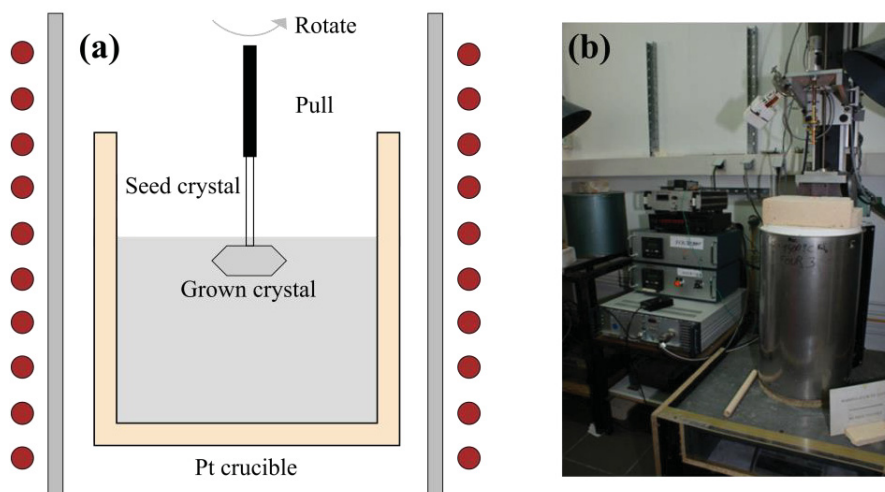


Fig. 3.6 TSSG method: (a) Scheme of the experimental configuration. (b) Experimental set-up at ICMCB.

Fig. 3.6 shows a scheme of the TSSG setup. The mixture of raw materials of the desired composition is loaded into a Pt crucible and placed into a vertical furnace with a low gradient ( $G < 1 \text{ } ^\circ\text{C}\cdot\text{cm}^{-1}$ ). After 12-24 hours heating, depending on the materials and the volume of the solution above the saturation temperature, we can get a homogeneous undersaturated solution with small undercritical-sized nuclei which cannot grow. Usually a high speed stirring with a spatula is applied to the undersaturated solution in order to

reduce the size of undercritical-sized nuclei for getting the most homogeneous solution. Then, after decreasing the temperature, a seed crystal with the desired orientation is dipped into the solution at the saturation temperature. When the solution is cooled-down slowly, the solution becomes supersaturated and the crystal starts to grow and continues to grow while the temperature decreases steadily, following thus the liquidus curve of the solute-solvent phase diagram. Optionally, one can pull the crystal while it grows in order to obtain larger crystals with interesting crystallographic direction. The TSSG feature a slow decreasing thermal ramp, for example  $0.05\text{ }^{\circ}\text{C}\cdot\text{h}^{-1}$ , so that the crystal grows more slowly than for Czochralski process. At the end of the growth, the as-grown crystal is pulled out of the liquid solution and then the cooling-down to room temperature with a higher cooling rate in the range of  $5\text{ }^{\circ}\text{C}\cdot\text{h}^{-1}$ - $30\text{ }^{\circ}\text{C}\cdot\text{h}^{-1}$  is applied.

Actually, the properties of solution (solubility of the solute to be grown, viscosity, thermal conductivity and surface tension) affect the size and the quality of as-grown crystal. While the geometrical set-ups of TSSG and Czochralski methods are similar, the growth issues are different. For TSSG method, the crystal is grown from a supersaturated solution with slow pulling velocity and low thermal gradient whereas for Czochralski method the crystal is grown from a supercooled melt with higher pulling velocity and higher thermal gradient.

---

### **3.3 The Floating Zone Technique**

---

The Floating Zone Technique was invented by W.G. Pfann at Bell Laboratories in 1951 [102]. The word “floating” indicates that there is no need for a crucible to hold the charge, the “zone” is the small portion of charge which is actually made of melt and grows as a single crystal from the seed. It is also called zone-levelling method where two solid-liquid interfaces are present. The charge used in this technique is a cylindrical polycrystalline sintered rod. The floating zone crystal grows from the molten lower solid-liquid interface by pulling both the seed and the feed rod. A stationary molten zone between rod and crystal has to be produced by contactless heating. This technique can be subdivided

in different variants with respect to the method used to heat the rod in the zone. Induction coils, resistive and optical heating are some examples.

---

### 3.3.1 Optical Floating Zone Technique

---

The optical floating zone technique uses halogen or xenon arc lamps as an energy source and ellipsoidal mirrors for focusing. It has been employed for crystal growth of a wide range of materials, from metals to semiconductors through oxides including high temperature superconductors and new magnetic materials [103-107]. Optical floating zone furnaces can be very energy efficient. With a suitable optical absorption spectrum of the considered compound to be grown with respect to that of lamp emission, oxides with melting temperatures as high as 2500 °C can be grown according to the type of lamps used and their power. Different image furnaces have been developed within the last 30 years for floating zone and similar applications [108]. Commercial systems specially designed for optical floating zone growth are available from the following companies: NEC (single and double-ellipsoid mirror furnaces) and Crystal Systems, Inc. (four mirror furnace) in Japan, MPEI in Russia (open vertical ellipsoid configuration with aperture), ScIDre GmbH in Germany (vertical configuration) and Cyberstar in France (single and double ellipsoid mirror furnaces).

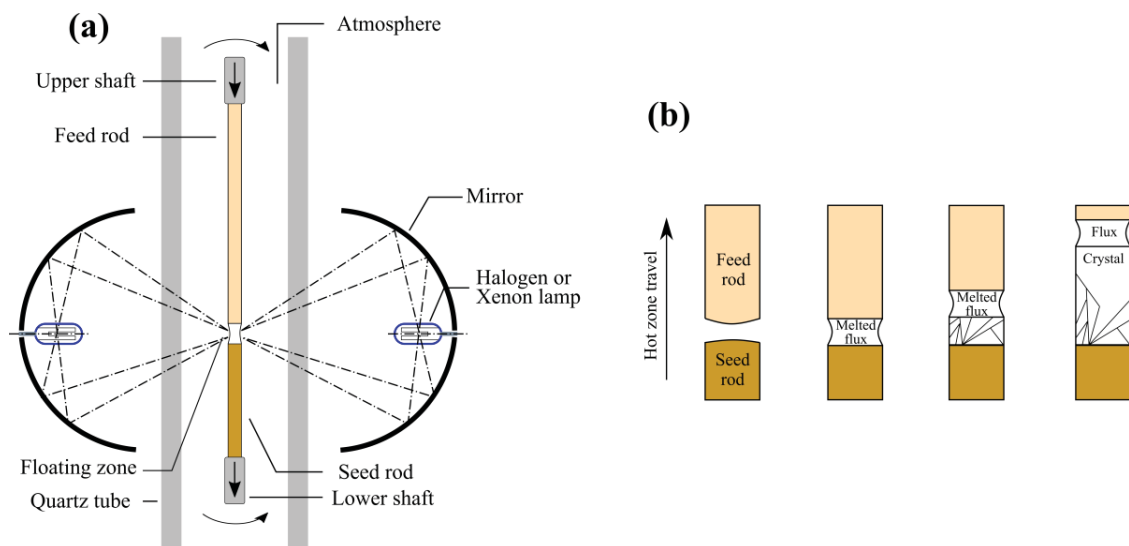




Fig. 3.7 (a) Schematic diagram of optical floating zone apparatus. (b) Stages of nucleation on ceramics rods. (c) Experimental set-up of a mirror furnace at ICMCB.

The schematic drawing of the optical floating zone furnace is presented in Fig. 3.7. In a typical crystal growth process, two polycrystalline “feed” and “seed” rods are prepared and aligned in a two- or four-mirror furnace in such a way that the tips of both rods meet at the common focal point of the semi-ellipsoidal mirrors. The halogen or xenon lamps are located at the other distinct focus point of each semi-ellipsoidal mirrors. The growth chamber is enclosed by a quartz tube, which allows the control of the growth atmosphere, such as inert, oxidizing, or reducing atmospheres, depending on the purpose of the experiment. The growth is started by melting the tips of the feed and seed rods, establishing a molten interface called the *floating zone*. Once the zone is created, the floating zone is moved either by moving the mirrors upward or by moving the rods downward. During the translation, the melt cools down and the material crystallizes on the seed rod. In the meantime, both rods (feed and seed) are made to rotate either in opposite directions. It is also important to note that many grains are formed at the beginning of the process. Finally, after a certain pulled length, one grain overcomes over the others and grows as a single crystal. The visual control of the molten zone and the growing crystal during the growth process is monitored with a CCD camera, equipped with a filter, connected to a computer. That allows to optically control and to record the shape of the zone.

The stability of the growth process and the quality of the crystal obtained depend strongly on the quality of the ceramic rod, which acts as the source of material for crystallization. Another important aspect is the alignment of the lamp and mirrors before starting the process. Several additional parameters can be controlled. The pulling rate can be adjusted in order to control the average growth rate. Indeed, as the feed rod is polycrystalline and as a single crystal is growing, the feed rod has usually a slightly higher speed of translation than that of the as-grown single crystal. Moreover, the rotation speed of both rods is important as it is responsible for mixing of the materials, for the shape of the crystallization, and for the defects resulting from it.

There are some limitations to the growth of crystals by the optical floating zone technique. It is not suitable for materials which are too much transparent (no light absorption enough), or with a high vapor pressure, or a low surface tension or high viscosity. Besides, for materials that undergo a 1<sup>st</sup> order phase transition during cooling, the crystals may crack during the cooling down or after growth. We note that it depends on the temperature at which the 1<sup>st</sup> order phase transition occurs. With this technique, for BaTiO<sub>3</sub> which exhibit a cubic-hexagonal phase transition around 1460 °C, we can grow and stabilize directly the high temperature hexagonal phase without any cracks and without growing the cubic phase due to the high thermal gradient (up to 300 °C.cm<sup>-1</sup>) and high pulling velocities (cm.h<sup>-1</sup>).

---

### **3.3.2 Laser-Heated Pedestal Growth**

---

The Laser-Heated Pedestal Growth (LHPG) technique is a modified floating zone melting process that uses a laser beam as the heating source. It is a relatively new crystal growth technique that produces 50-800 μm wide fibers. Using this technique, single crystal fibers such as BaTiO<sub>3</sub> [109], CaTiO<sub>3</sub> [110], and doped or undoped LiNbO<sub>3</sub> [111-113] have been successfully grown. Haggerty [114] *et al.* developed the LHPG technique in 1972 and later this was improved by Feigelson [115] at Stanford University.

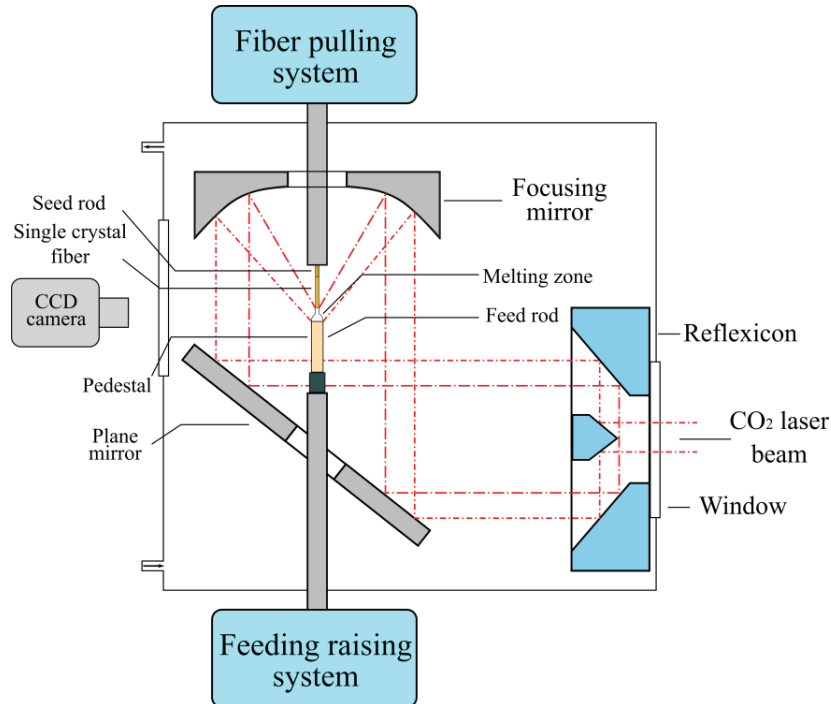


Fig. 3.8 Schematic drawing of the laser-heated pedestal growth (LHPG) technique.

A schematic illustration of LHPG is given in Fig. 3.8. In the setup based on the Stanford version of the LHPG technique, the heating laser is a high-power CO<sub>2</sub> continuous laser (200 W) emitting at 10.6  $\mu\text{m}$ . The laser beam is guided into a closed chamber through a window and hit the reflexicon [116], where they are converted into a cylinder shell and guided to a spherical or parabolic mirror and focused over the source material. The focusing mirror has a hole in center allowing the seed holder to be placed in its optical axis as well as to avoid vapor material deposition onto the optical mirrors during fiber pulling. A growth chamber allows for a controlled growth atmosphere. This technique can easily melt oxide compositions up to 2 mm in diameter at temperatures as high as 2800 °C. In general, the pulling process consists in four steps. The first step is to align the seed and the pedestal mechanically, both centered in the optical axis of the laser beam. The second step is to create a small molten zone on top of pedestal, by turning on the plane mirror to adjust the laser beam and slowly increasing laser power. In the third step, the seed is introduced into the liquid and a molten zone is formed. Finally, the motors start the fiber pulling and rotation.

---

### 3.4 Grown of Perovskite-Type Oxides

---

A single crystal can be grown by various techniques. For example, BaTiO<sub>3</sub> crystal can be grown by flux growth, laser heated pedestal growth or floating zone technique. The flux growth is a widely used method for growth of BaTiO<sub>3</sub> crystals. However, the disadvantages of this method are substantial. Examples include interstitial incorporation of solvent ions into the crystal, microscopic and macroscopic inclusions of solvent or impurities, container problems, or a slow growth rate. It should be noticed that there is no perfect technique to obtain high quality crystals.

Herein, we discuss a list of the perovskite-type crystals which have been prepared from various techniques over several decades. This table is not only devoted to the crystal growth information with an extensive list of references to previous works, but also to present a summary of the growth techniques and particular issues related to the crystals. Most information on the crystals are related to the end members of the BCTZ system: BaTiO<sub>3</sub>, CaTiO<sub>3</sub> and BaZrO<sub>3</sub> crystals. Many other perovskite crystals have also been investigated, for instance PbTiO<sub>3</sub>, SrTiO<sub>3</sub> or SrZrO<sub>3</sub>. For instance, PbTiO<sub>3</sub> is one of the end members of the lead zirconate titanate (PbZr<sub>x</sub>Ti<sub>1-x</sub>O<sub>3</sub> 0 ≤ x ≤ 1, PZT) system, which is technologically one of the most important ferroelectric and piezoelectric materials.

Table 3.1 is organized as follows: the crystallized materials are listed in the order of the element which is conventionally used as the first symbol in the formula for the compound. The second column lists the employed temperature or temperature range. Column 3 lists the technique used in the experiment, and the abbreviations used are explained at the beginning of the table. Columns 4 and 5 presents the crystal properties and issues used by this growth technique. The size in mm of the largest crystals grown or alternatively the largest dimension is given in column 6. In the final column, the reference to the source publication is given.

AM: Arc-melting

CZ: Czochralski

EV: Evaporation

FG: Flux growth

FZ: Floating zone

LHPG: Laser heated pedestal growth

SC: Slow cooling

SM: Skull-melting

TSFZ: Travelling solvent floating zone

TSSG: Top seeded solution growth

**Table 3.1 Perovskite-type compounds grown by various technique**

Crystal	Temp.range (°C)	Technique	Properties	Issues	Crystal size (mm)	Reference
BaTiO <sub>3</sub>	900-1200	FG (SC) Solvent KF	Large clear single crystals	Twin plates "butterfly wings"; Contaminated with flux		Remeika (1953)[117]
BaTiO <sub>3</sub>	950-1000	FG (SC) Solvent KF	Growth from non-stoichiometric melts	A narrow temperature range; Impurity (K, F, Pt and Fe); A slow growth rate	5×5×5	Eustache (1957)[118]
BaTiO <sub>3</sub>	~1650	CZ	A mixed of hexagonal, cubic, tetragonal phases	0.36 wt.% Rh and 0.02 wt.% Ir in crystal	Φ12.7×6.3	Nassau <i>et al.</i> (1962)[119]
BaTiO <sub>3</sub>	1500-1600	FZ	Crucible-free; Atm: O <sub>2</sub> /Ar 1:1	Containing 1.5% SrTiO <sub>3</sub> ; Be careful minimize thermal shock	Φ3.2×25	Brown <i>et al.</i> (1964)[120]
BaTiO <sub>3</sub>	1275-1500	FG (SC) Solvent BaCl <sub>2</sub>	High-purity BaTiO <sub>3</sub>	Main impurity (Al); Oxygen deficiency; Transition to hexagonal form at 1325°C		Arend <i>et al.</i> (1969)[121]
BaTiO <sub>3</sub>	~1390	TSSG (modification from CZ)	Non-stoichiometric melts; Low thermal gradients	Low solubility; Low growth rate (1mm/day); Imperfect temp. control (solvent inclusion)	10×10×10	Belruss <i>et al.</i> (1971)[101]
BaTiO <sub>3</sub>		LHPG	Rapid solidification; Stoichiometric melt; Rapid growth rates	High temperature gradient affect crystal growth kinetics	Φ0.1×100	Saifi <i>et al.</i> (1986)[109]
BaTiO <sub>3</sub>	1322-1400	TSSG (modification from CZ)	Large commercial photorefractive crystals; Low thermal gradients	Stresses introduced during crystal growth; Low levels of transition-metal impurities	20×20×25	Schunemann <i>et al.</i> (1988)[122]
BaTiO <sub>3</sub>		TSEZ	Slightly opaque yellow; Doped with Sr (1.0-3.0 mol%)	Destruction of the crystals due to tetragonal-orthorhombic transition near room temp. for practical application	3×4×5	Furukawa <i>et al.</i> (1991)[123]
BaTiO <sub>3</sub>		LHPG	Single ferroelectric domain tetragonal fiber; Photorefractive effect	Some cracks induced in the electrical poling	Φ0.25×2	Ito <i>et al.</i> (1992)[124]

Crystal	Temp.range (°C)	Technique	Properties	Issues	Crystal size (mm)	Reference
BaTiO <sub>3</sub>		LHPG	Larger crystal diameter; Higher growth rates	Cracks at the crystal surface; High temperature gradient 2050°C/mm	Φ0.4-Φ1.0	Lee <i>et al.</i> (1999)[125]
BaZrO <sub>3</sub>		AM (Crystal Base Co. Ltd)	Transparent		3×3×1	Helal <i>et al.</i> (2015)[126]
BaZrO <sub>3</sub>		SM	Orange color	Regulate efficiently the temp. of the melt	0.53×0.25×0.13	Paun (2015)[96]
BiFeO <sub>3</sub>	820-860	FG (SC+EV) Solvent Bi <sub>2</sub> O <sub>3</sub>	Low polarization (3.5 μC/cm <sup>2</sup> ) for [100]	Volatilization of Bi <sub>2</sub> O <sub>3</sub> and reaction with a nickel crucible	1-2	Teague <i>et al.</i> (1970)[127]
BiFeO <sub>3</sub>	<837	FG (SC) Solvent Bi <sub>2</sub> O <sub>3</sub> -Fe <sub>2</sub> O <sub>3</sub>	Monodomain single crystal	Size not usable for physical investigations	0.166×0.140×0.032	Kubel <i>et al.</i> (1990)[128]
BiFeO <sub>3</sub>	750-850	FG (SC) Solvent Bi <sub>2</sub> O <sub>3</sub> -Fe <sub>2</sub> O <sub>3</sub>	Highly pure single crystal; Black platelet; High electrical resistivity; P <sub>[012]</sub> ~60 μC/cm <sup>2</sup>	Millimeter-sized	1.4×1.6×0.04	Lebeugle <i>et al.</i> (2007)[129, 130]
BiFeO <sub>3</sub>	790-900	FG (SC) Solvent Bi <sub>2</sub> O <sub>3</sub> -Fe <sub>2</sub> O <sub>3</sub>	Dark purple-grey; Centimeter high- quality	Need to work more precisely to choose a composition of flux	10×3×1	Haumont <i>et al.</i> (2008)[131]
BiFeO <sub>3</sub>		FZ	Bulk single crystal without external strains; High quality; Stoichiometric mixed polarization (~50 μC/cm <sup>2</sup> ) for [100]	Impurity phases (Bi <sub>2</sub> Fe <sub>4</sub> O <sub>9</sub> , Bi <sub>25</sub> FeO <sub>40</sub> , Bi <sub>24</sub> Fe <sub>2</sub> O <sub>39</sub> ); Excess oxygen led to conduction in the crystals	Φ4×50	Ito <i>et al.</i> (2011)[132]
CaTiO <sub>3</sub>	1150	FG (SC) Solvent BaCl <sub>2</sub> +CaCl <sub>2</sub>	Orthorhombic (still at 900 °C) Space group <i>Pcmn</i>	Sample twinned	~1	Kay and Bailey (1957)[133]

Crystal	Temp.range (°C)	Technique	Properties	Issues	Crystal size (mm)	Reference
CaTiO <sub>3</sub>	1170	FG (SC) Solvent KF or CsF	Transparent, straw-coloured (KF as flux); Dark brown (CsF as flux)	Impurity 0.1%K and 0.1%F; cracks (CsF as flux); Difficult to obtain reproducibly good result	2×2×2 (KF as flux); 5×5×3 (CsF as flux)	Watts <i>et al.</i> (1989)[134]
CaTiO <sub>3</sub>		LHPG	Single crystal fiber; No unusual behavior with phase transition	A simple twinned structure	Φ0.5-Φ0.7×20	Jiang <i>et al.</i> (1998)[110]
PbTiO <sub>3</sub>	~500-900	FG(SC) Solvent PbCl <sub>2</sub>	Large polydomain crystals	Thick and opaque crystal	~1	Nomura and Sawada (1952)[135]
PbTiO <sub>3</sub>	1040-1300	FG(SC) Solvent PbO	Small, high purity, single crystal	The crystal was single above the Curie point, but fractured on passing through the transition; Existence of twinning planes	3×1.5×0.2	Rogers (1952)[136]
PbTiO <sub>3</sub>	600-920	FG(SC) Solvent KF	Thin, transparent, light yellow	Coercive force of crystal extremely large; Slow growth rate	9×7×0.05	Kobayashi (1958)[137]
PbTiO <sub>3</sub>	900-950	FG(SC) Solvent KF	Flat plates	The conductivity of crystal shows an anomalous variation near Curie temperature	20×20×2.5	Bhide <i>et al.</i> (1962)[138]
PbTiO <sub>3</sub>	700-1100	TSSG Solvent PbO	High resistivity (> 10 <sup>10</sup> ohm·cm); T <sub>c</sub> = 492±5 °C	0.1 wt.% U	5×3×1	Remeika and Glass (1970)[139]
PbTiO <sub>3</sub>		CZ	Transparent single crystal, brownish yellow	PbO evaporation; Pt impurities ~0.01 wt.%	Φ20×3	Grabmaier (1976)[140]
PbTiO <sub>3</sub>		TSSG Solvent PbO+B <sub>2</sub> O <sub>3</sub>	Large polarization ~200 μC/cm <sup>2</sup>	Less than 11 mol% of TiO <sub>2</sub> in the PbO-TiO <sub>2</sub> solution. PbTiO <sub>3</sub> Single crystal are not obtained; PbO volatilization in the TSSG process	32×32×6	Oka <i>et al.</i> (1996)[141]
PbTiO <sub>3</sub>		FZ O <sub>2</sub> pressure approx.2-3 atm	High chemical and phase purity; Large specific heat anomaly;Extremely sharp phase transition	Large single crystals were not obtained due to instabilities of the molten liquid zone; Cracks	Φ5	Maffei and Rossetti (2011)[142]

Crystal	Temp.range (°C)	Technique	Properties	Issues	Crystal size (mm)	Reference
PbZrO <sub>3</sub>	1250	FG Solvent PbF <sub>2</sub>	Transparent, light brown color	Sample twinned; To control the evaporation of PbF <sub>2</sub> was unsuccessful	0.3	Jona <i>et al</i> (1955)[143]
PbZrO <sub>3</sub>	800-1280	FG Solvent PbF <sub>2</sub> +PbO+ B <sub>2</sub> O <sub>3</sub>	High-purity single crystal; P <sub>S</sub> ~24 μC/cm <sup>2</sup> ;	Highly twinned	1-3	Scott and Burns (1972)[144]
PbZrO <sub>3</sub>	950-1170	FG Solvent PbO	Pb ion displacements and ZrO <sub>6</sub> octahedral tilts in the antiferroelectric	The effect of etching the surfaces of crystals	1-2	Whatmore and Glazer (1979)[145]
PbZrO <sub>3</sub>	900-1040	FG Solvent B <sub>2</sub> O <sub>3</sub>	Transparent light grey crystals and thin plates	A transient phase does not exist spontaneously below Currie temperature	3×1×0.024	Roleder and Dec (1988)[146]
PbZrO <sub>3</sub>	900-1100	FG Solvent B <sub>2</sub> O <sub>3</sub>	Transparent light grey thin rectangular plates; One phase transition from the paraelectric to antiferroelectric	No able to grow large bulk crystal	0.07×0.07×0.03	Glazer <i>et al</i> (1993)[147]
SrTiO <sub>3</sub>	770-1200	FG(SC) Solvent KF+LiF	Pale yellow, translucent, cube	Often contained flux inclusions, inferior quality	7×7×7	Sugai <i>et al</i> (1968)[148]
SrTiO <sub>3</sub>	850-1250	FG(SC) Solvent KF+K <sub>2</sub> MoO <sub>4</sub>	Colorless, cube, platy; Free from inclusions and superior in quality	When much K <sub>2</sub> MoO <sub>4</sub> was added the solubility became very low, producing only fine crystals	4×4×4	Sugai <i>et al</i> (1968)[148]
SrTiO <sub>3</sub>	900-1410	FG(SC) Solvent SiO <sub>2</sub>	Clear, colorless to pale brown, of good optical quality, free from inclusions		2.5	Robbins (1968)[149]
SrTiO <sub>3</sub>	~1530	TSSG Solvent TiO <sub>2</sub>	Large crystal; “capping” effect	Low solubility led to low growth rate and solvent inclusions due to imperfect temp. control.	~7.5 g	Belruss <i>et al</i> (1971)[101]

Crystal	Temp.range (°C)	Technique	Properties	Issues	Crystal size (mm)	Reference
SrTiO <sub>3</sub>		CZ	monocrystals	Crystal colouring due to non-controlled impurities in the initial burden;	Φ15×30	Aleksandrov <i>et al</i> (1983)[150]
SrTiO <sub>3</sub>		LHPG	Transparent and colorless; High quality stoichiometric single crystal fiber	Effect of oxygen vacancies was not negligible	Φ0.5×30	Ardila <i>et al</i> (1998)[151]
SrTiO <sub>3</sub>	~1600	FZ	Crack-free cylindrical boules; Colorless crystals (annealing at 1000 °C for 1-2h)	Small impurity levels indicated may be excluded as a reason for the crystal color; Annealing or growth of the crystals in oxygen atmosphere resulted in dark brown or black crystals	Φ15-20×40-80	Nabokin <i>et al</i> (2002)[152]
SrZrO <sub>3</sub>		FZ	Colorless, transparent, crack-free	Instability of the crystal growth at low growth rates; Composition changes of the molten zone due to evaporation of SrO; Non-axisymmetrical growth at high crystal rotation rates	Φ5×40	Souptel <i>et al</i> (2002)[153]

## 4 Characterization Techniques

---

In this chapter, the various techniques used in the characterization of our grown crystals are discussed.

---

### 4.1 Structural Characterization

---

---

#### 4.1.1 X-Ray Diffraction

---

X-ray diffraction is a non-destructive analytical technique which provides detailed information about the lattice of crystalline substance, including unit cell dimensions, bond lengths, bond angles, and details of site ordering.

When a monochromatic X-ray beam falls into a crystal lattice, a regular periodic arrangement of atoms, a diffracted beam will result in certain directions. It is necessary that the waves emitted by the individual atoms are in phase with each other in the direction of observation. Usually a crystal lattice is drawn as a set of parallel lines at a distance  $d$  where all atoms are situated in these planes, as shown in Fig. 4.1. For achieving the diffraction, the incident beam, the diffracted beam and the normal to the reflecting planes wave vectors must satisfy the phase matching condition. The plane matching condition is thus illustrated through the Bragg's law:

$$n\lambda = 2d_{hkl}\sin\theta_{hkl} \quad (4.1)$$

where  $n$  is the diffraction order,  $\lambda$  represents the wavelength of the X-ray used,  $\theta_{hkl}$  is Bragg's angle and  $d_{hkl}$  is the interplanar spacing.

Therefore, if  $\lambda$  and  $\theta_{hkl}$  are known, then the spacing between lattice planes  $d_{hkl}$  and consequently, the unit cells dimensions and the indices h, k, l of those crystal planes, can be determined.

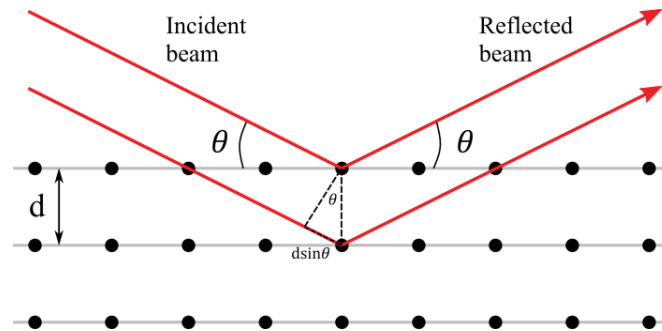


Fig. 4.1 Schematic of Bragg's law.

The relationship between the lattice parameters and  $d_{hkl}$  are given in Table 4.1 for the seven crystallographic systems. For instance, some BaTiO<sub>3</sub> different structures are given in Fig. 4.2 [154, 155] where the sequence of phase transitions with respect to the temperature is rhombohedral to orthorhombic phase transition at -90 °C, orthorhombic to tetragonal phase transition at 0 °C, tetragonal to cubic phase transition at 130 °C and cubic to hexagonal at around 1460 °C. In some cases, a monoclinic phase is reported [156].

Table 4.1 Seven crystallographic systems and the relationships between  $d_{hkl}$  and the corresponding lattice parameters

Crystal System	Axis System	Relationship
Cubic	$a=b=c,$ $\alpha=\beta=\gamma=90^\circ$	$\frac{1}{d^2} = \frac{h^2 + k^2 + l^2}{a^2}$
Tetragonal	$a=b \neq c,$ $\alpha=\beta=\gamma=90^\circ$	$\frac{1}{d^2} = \frac{h^2 + k^2}{a^2} + \frac{l^2}{c^2}$
Orthorhombic	$a \neq b \neq c,$ $\alpha=\beta=\gamma=90^\circ$	$\frac{1}{d^2} = \left(\frac{h}{a}\right)^2 + \left(\frac{k}{b}\right)^2 + \left(\frac{l}{c}\right)^2$
Hexagonal	$a=b \neq c, \alpha=\beta=90^\circ$ $\gamma=120^\circ$	$\frac{1}{d^2} = \frac{4(h^2 + hk + k^2)}{3a^2} + \frac{l^2}{c^2}$
Rhombohedral	$a=b=c,$ $\alpha=\beta=\gamma \neq 90^\circ$	$\frac{1}{d^2} = \frac{(1 + \cos \alpha)[(h^2 + k^2 + l^2) - (1 - \tan^2 \frac{1}{2} \alpha)(hk + kl + lh)]}{a^2(1 + \cos \alpha - 2 \cos^2 \alpha)}$

Monoclinic	$a \neq b \neq c, \alpha = \gamma = 90^\circ$ $\beta \neq 90^\circ$	$\frac{1}{d^2} = \frac{h^2}{a^2 \sin^2 \beta} + \frac{k^2}{b^2} + \frac{l^2}{c^2 \sin^2 \beta} - \frac{2hl \cos \beta}{ac \sin^2 \beta}$
Triclinic	$a \neq b \neq c,$ $\alpha \neq \beta \neq \gamma \neq 90^\circ$	$\frac{1}{d^2} = \frac{1}{V^2} (s_{11}h^2 + s_{22}k^2 + s_{33}l^2 + 2s_{12}hk + 2s_{23}kl + 2s_{13}hl)$ $V^2 = a^2b^2c^2(1 - \cos^2 \alpha - \cos^2 \beta - \cos^2 \gamma + 2 \cos \alpha \cos \beta \cos \gamma)$

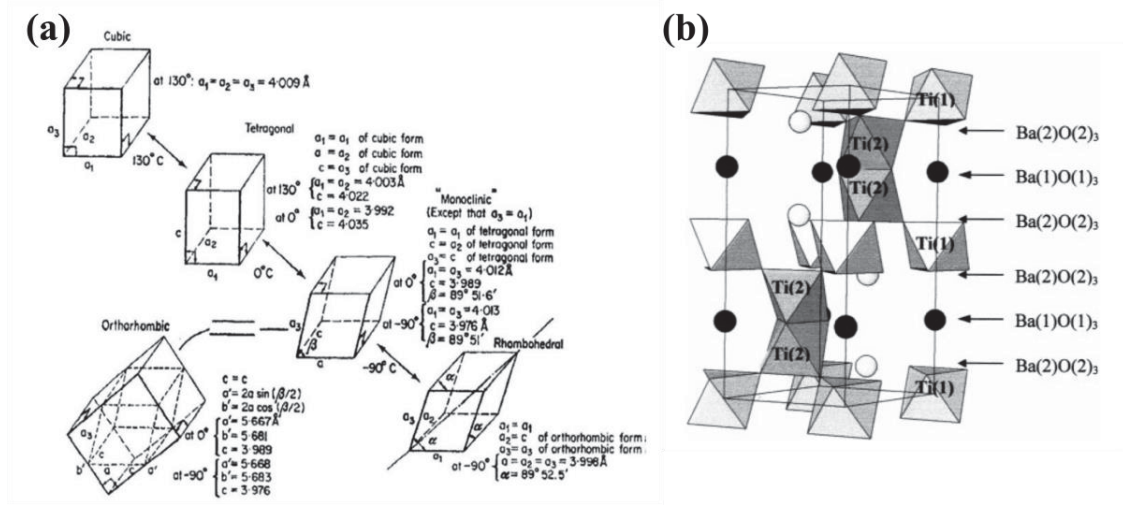


Fig. 4.2 (a) The different structures of BaTiO<sub>3</sub> at low temperature. (b) Structure of hexagonal BaTiO<sub>3</sub>.

Powder XRD data of crushed single crystals were recorded to determine the crystallographic structure and crystallized phases purity. XRD measurements at room temperature were carried out with a PANalytical X'pert Pro MPD diffractometer using a Cu K $\alpha$  radiations ( $\lambda_{K\alpha 1} = 1.5406 \text{ \AA}$  and  $\lambda_{K\alpha 2} = 1.5444 \text{ \AA}$ ), and Bragg-Brentano geometry.  $2\theta$  was in the range between  $8^\circ$  and  $80^\circ$  with a step size of  $0.02^\circ$ . All XRD measurements were carried out by Mr. Eric Lebraud at ICMCB.

#### 4.1.2 Laue X-ray Diffraction and Orientation of Single Crystals

The Laue diffraction is a frequently used method for aligning bulk crystals in a desired orientation with respect to the crystallographic axes or planes. Typically, there are two common configurations of optics used, one is called “back-reflection” and the other

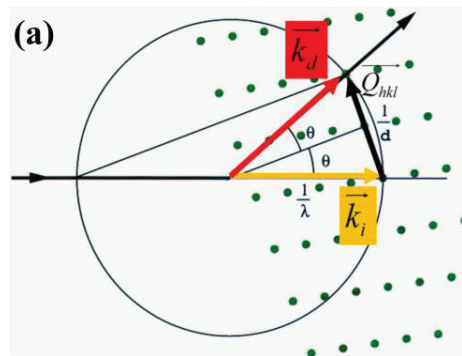
“transmission Laue”. At ICMCB, due to the high thickness of the crystals ( $>0.5$  mm), we use back-reflection Laue configuration with the X-ray CCD detector placed between the X-ray source and the crystals (see Fig. 4.4 (c)).

In this method, the crystal sample is mounted on a goniometer head set on a 6-degree of freedom rotation and translation stages (see Fig. 4.4 (c)). An X-ray beam from an anticathode radiates on a crystal through a capillary collimator at the center of a CCD screen where the incident beam is perpendicular to the surface of the screen. When the diffraction condition is fulfilled, the X-ray beam diffracted from a plane family in the crystal results in a Bragg spot on the screen. While multiple sets of planes fulfill the Laue condition at the same time, a diffraction pattern of corresponding spots can be observed (see Fig. 4.4 (a)). The diffraction spots themselves correspond to reciprocal lattice points, which are represented by reciprocal vectors corresponding to crystallographic directions. Indeed, from an optical point of view, the reflected beam wave vector  $k_d$ , the incident beam wave vector  $k_i$  and the reciprocal space vector  $Q_{hkl}$  of the considered  $hkl$  plane are satisfying the phase matching related to energy and momentum conservation of the X-ray photons:

$$\begin{cases} \Delta E = \hbar\Delta\omega = 0 \\ \Delta\vec{p} = \hbar\Delta\vec{k} = \vec{0} \end{cases} \quad (4.2)$$

$$\Rightarrow \vec{Q}_{hkl} = \vec{k}_i - \vec{k}_d \quad (4.3)$$

through the Ewald sphere construction depicted in Fig. 4.3 (a)



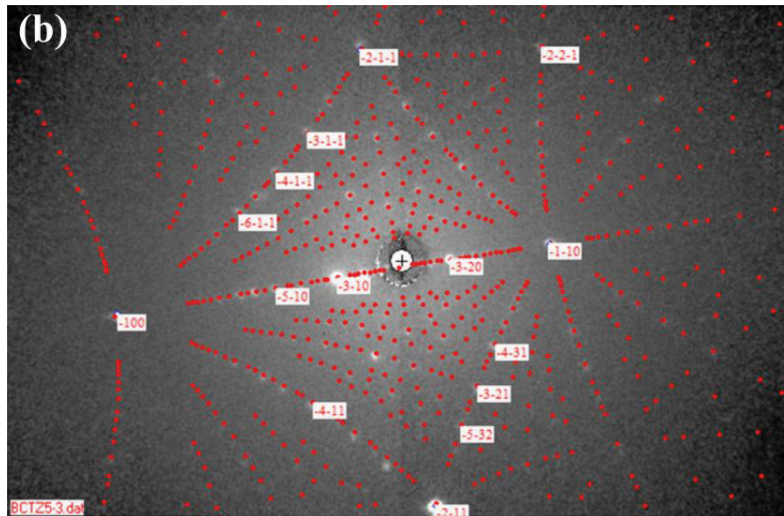


Fig. 4.3: (a) Ewald sphere construction showing phase matching in between incident and reflected beams. The phase matching is fulfilled when a dot is on the Ewald sphere so that  $\Delta k=0$ . (b) Example of a back scattered Laue pattern performed on a BCTZ single crystal.

At ICMCB, the molybdenum (Mo) tube produces enough polychromatic radiation (Bremsstrahlung) in the range 0.5-2.5 Å (see Fig. 4.4). To orient a crystal with the desired crystallographic directions, the relative position of the crystal was changed by adjusting the goniometer. Then, the crystal was cut with a diamond wire saw with less than 1° of accuracy along these desired crystallographic directions. All the work of the orientation crystals was performed at ICMCB with a PSL Laue setup (Dual lens coupled X-ray Laue system, Photonic Science Ltd., Robertsbridge, UK) and the OrientExpress software[157] (Institut Laue-Langevin, Grenoble, France).

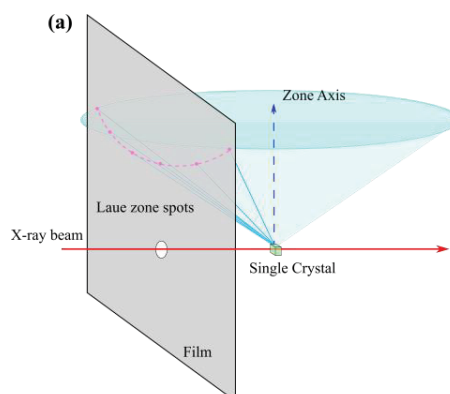




Fig. 4.4 (a) Scheme of the principle of the Laue technique in the back-reflection mode. (b) and (c) Experimental set up with 6-degree of freedom rotation and translation stages.

---

## 4.2 Chemical Analysis

---



---

### 4.2.1 Glow Discharge Mass Spectrometry

---

Glow discharge mass spectrometry has been recognized to provide reliable quantitative concentrations for most elements down to levels around 0.01 ppm. GDMS is an efficient direct solid-state analysis method without any chemical process[158]. In GDMS, an argon gas glow discharge at low pressure is used as an ion source. The  $\text{Ar}^+$  ions are accelerated towards a cathode consisting of the sample material. The sample surface is sputtered and evaporated neutral particles are ionized in a glow discharge plasma by Penning and/or electron impact ionization and charge exchange process. After that, the positive ions are separated in a double-focusing mass spectrometer due to their mass to charge and energy to charge ratios and finally detected by ion detector. The impurity contents of  $\text{BaZrO}_3$  crystals were measured by the commercial glow discharge mass spectrometry VG-9000 (VG-Elemental, Thermo Instruments) from EAG Laboratories. The pressure of the plasma cell is around  $10^{-4}$  or  $10^{-5}$  mbars. The sample is cooled down to liquid nitrogen temperature (around  $-196$  °C). GDMS measurements were performed by Mr. Jérémy Berot-Lartigue from EAG laboratories.

---

## 4.2.2 Electron Probe Micro-Analysis

---

Electron Probe Micro-Analysis (EPMA) is a technique for chemical analyses of small selected areas of solid samples. EPMA is a fully quantitative method for non-destructive elemental analysis of micron-sized volumes at the surface of materials through Wavelength Dispersion Spectrometry (WDS). Detection limit ranges from 0.005 wgh.% (heavier elements) to 0.1 wgh. % (lighter elements). Under normal conditions, spatial resolution is limited to about  $1 \mu\text{m}^3$  by the spread of the beam within the sample. The spatial distributions of specific elements can be recorded in the form of line profiles or two-dimensional maps [159]. EPMA works by bombarding a micro-volume of a sample with a focused electron beam and collecting the X-ray photons emitted by the various elemental species. Because the wavelength of these X-rays is characteristic of the emitting species, the sample composition can be easily identified by recording wavelength dispersive spectroscopy (WDS) spectra. WDS spectrometers operate based on Bragg's law and use various moveable, shaped monocrystals as monochromators.

All BCTZ crystals were analyzed with a carbon coated polished sample using a CAMECA SX-100 EPMA instrument (Gennevilliers, France) working at 15 kV with a WDS spectrometry system. The measurements were performed by Dr. Michel Lahaye from PLACAMAT – UMS 3626. EPMA reference samples [76] used to determine element concentrations with less than 0.3 mol.% of accuracy are described in Table 4.2.

Table 4.2 EPMA reference samples for accurate quantitative analysis of elements.

Elements	EPMA References
Ba	BaTiO <sub>3</sub> single crystal
Ca	CaF <sub>2</sub> single crystal
Ti	BaTiO <sub>3</sub> single crystal
Zr	ZrO <sub>2</sub> sintered ceramics (4N)

---

### 4.2.3 Energy Dispersive X-ray Analysis

---

Energy dispersive X-ray analysis (EDX) is an X-ray technique used to identify qualitatively the elemental composition of materials. The EDX systems consists in a Scanning Electron Microscopy (SEM), where the imaging capability of the microscope identifies the specimen of interest through Energy Dispersion Spectrometry (EDS). Detection limit ranges from 0.1 wgh. % (heavier elements) to 1 wgh. % (lighter elements). All the elements from atomic number Be to U can be detected in principle but the resolution is lower than for WDS. When the sample is bombarded by the SEM's electron beam, electrons are rejected from the atoms from the sample surface. The resulting electron vacancies are filled by electrons from a higher state, and an X-ray is emitted to balance the energy difference between the two electron states. The X-ray energy is characteristic of the element from which it was emitted. The EDX technique detects X-rays emitted from sample during bombardment by an electron beam to characterize the elemental composition of the analyzed volume.

EDX was achieved using a Quanta FEG 200 (FEI) coupled with an EDS GENESIS XM 4i (EDAX) for both BaZrO<sub>3</sub> and BCTZ crystals. The measurements were performed by Jean-Luc Biagi from LIST.

---

### 4.2.4 Secondary Ion Mass Spectrometry

---

Secondary Ion Mass Spectrometry (SIMS) uses ions for bombardment and detection and has a much higher sensitivity (ppm to ppb) than other techniques, such as EDX. In a conventional SIMS experiment, an energetic primary ion beam, with ions such as Ga<sup>+</sup>, Cs<sup>+</sup>, or Ar<sup>+</sup>, is focused onto a solid sample surface under ultra-high vacuum conditions. The interaction of the primary ion beam with the sample results in the sputtering and the ejection of secondary ions from the surface of the material. These secondary ions are

subsequently extracted into a mass analyzer, resulting in the creation of a mass spectrum that is characteristic of the analyzed surface, and yield elemental, isotopic, and molecular information simultaneously, with sensitivities in the parts per million to parts per billion range. SIMS also can be utilized for both surface (at low primary ion doses) and in-depth profiles analysis (at high primary ion doses) [160]. SIMS quantification should be achieved with standards. The advantages of this technique are high depth resolution and high sensitivity over periodic table. However, the disadvantages are that it is a destructive technique, subject to many mass interferences, and that quantification require secondary standards [161].

All BaZrO<sub>3</sub> samples were analyzed using a CAMECA SC Ultra SIMS instrument with O<sub>2</sub><sup>+</sup> primary ion beam to enhance the ionization of the impurities studied. Impact energy for O<sub>2</sub><sup>+</sup> was 1 keV with incidence angle of 64°. A beam current of 50 nA was set over a 250 μm<sup>2</sup> area and ions detected from a 30 μm diameter region at the center of the crater. Analyses were performed under high vacuum conditions with chamber pressure of approximately 1 × 10<sup>-8</sup> mbar. They were carried out at low mass resolution. This caused in particular interferences for Ti detection at mass 48 due to the presence of <sup>48</sup>Ca. This could be corrected for by considering the <sup>40</sup>Ca concentration and taking into account the natural abundance of the isotope 48. Samples were sputtered up to the depth of 1 μm. Sputtering rate was determined by sputtering a region for an extended span of time so that the crater was sufficient to be measured despite the surface roughness. The sputtering rate obtained was 0.08 nm.s<sup>-1</sup>. SIMS measurements were performed by Dr. Nathalie Valle at LIST.

---

### 4.3 UV-Visible Spectroscopy

---

The optical transmission spectra of BaZrO<sub>3</sub> single crystals were measured by UV-Visible spectrometers (Cary 5000, Agilent, Santa Clara, USA) at ICMCB. The absorption can be determined by using relation [162]:

$$T \approx (1 - R)^2 \exp(-\alpha d) \quad (4.4)$$

where  $T$  is the transmittance,  $R$  is the reflectivity,  $\alpha$  is the absorption coefficient and thickness of  $d$  of the samples. We neglect reflectivity. Hence, the value of the band gap in principle be determined by Tauc plot, i.e plotting  $(\alpha \cdot hv)^{1/r}$  as the function of the energy  $hv$ , where  $h$  is Planck's constant and  $r$  equals  $\frac{1}{2}$  or  $2$  for a direct or indirect gap, respectively.

---

## 4.4 Electrical Characterization

---

---

### 4.4.1 Dielectric Measurement

---

Different setups were used for dielectric measurements. For BaZrO<sub>3</sub>, the specific capacitance of the single crystals were measured as a function of temperature using a Quantum Design - Physical Property Measurement System (PPMS M6000, San Diego, USA), from 4.2 K to room temperature (298 K). The BaZrO<sub>3</sub> samples for capacitance measurements were prepared by deposition of gold electrodes on the surface, silver wires were attached to the sample. Measurement cables were hold by silver paint and measurements were performed at various selected frequencies. The temperature during the capacitance measurements was controlled by the PPMS system.

For BCTZ crystals, the first part of this work on the temperature-dependent dielectric properties was carried at ICMCB out using a HP4194 impedance analyzer (Hewlett Packard, Palo Alto, CA, USA). Electrodes were deposited on both sides of the sample by gold sputtering. The sample was placed between two copper plates and the whole structure was mounted inside a homemade cell (a quartz tube), equipped with a heater resistor. The two copper plates were connected to the HP4194 impedance analyzer, which allows dielectric measurements at selected frequencies (100 Hz-1 MHz). Liquid nitrogen can be used to cool down to the desired temperature (around 90 K with this setup). A thermocouple was placed near the sample and connected to a Eurotherm 902 (Schneider Electric, Lyon, France). The Eurotherm device also controlled the heating power through

a resistor (see Fig. 4.5). The heating or cooling rate was set to with  $1 \text{ K.mn}^{-1}$  in the temperature range from 90 K to 470 K.

The other part of this work was carried out at LIST with a Novocontrol Alpha-A high performance frequency analyzer (Novocontrol technologies, Montabaur, Germany). The system was equipped with a cryostat in the temperature range from 130 K to 470 K. The heating or cooling rate was set to  $2 \text{ K.mn}^{-1}$ .

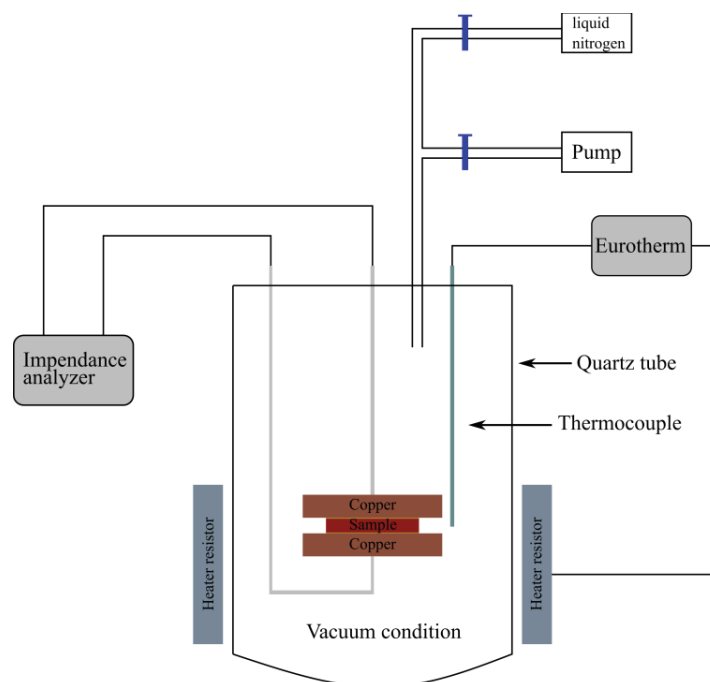


Fig. 4.5 Schematic of dielectric measurement setup at ICMCB.

---

#### 4.4.2 Ferroelectric Hysteresis Loop

---

A ferroelectric hysteresis loop is the direct proof of ferroelectricity. The classic electrical circuit for ferroelectric hysteresis loop measurement is called the Sawyer-Tower circuit [163]. The measurement circuit can be simplified like Fig. 4.6. The voltage was supplied by a function generator (Agilent, 33210A, Agilent Technologies, Böblingen, Germany). The applied voltage and the voltage across to the reference capacitor were

recorded by an oscilloscope (Agilent DSO5014A, Agilent Technologies Böblingen, Germany) and amplified by a high voltage amplifier (Trek, model 20/20C, Medina, NY, USA).

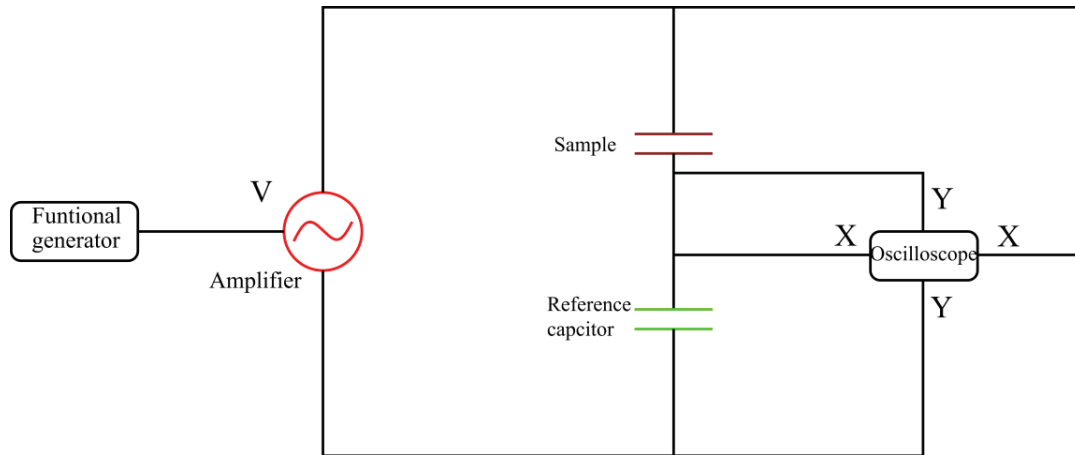


Fig. 4.6 Sawyer-Tower electric circuit for ferroelectric hysteresis loop measurement.

In the Sawyer-Tower circuit, the sample capacitor and the reference capacitor are in series. The value of capacitance of the reference capacitor ( $C_R$ ) should be much higher than that of the sample ( $C_S$ ). The polarization ( $P$ ) of the measured sample and the applied electric field ( $E$ ) can be calculated by the following equations:

$$P = \frac{Q_S}{A} = \frac{Q_R}{A} = \frac{C_R \cdot U_R}{A} = \frac{C_R}{A} \cdot U_Y \quad (4.5)$$

$$E = \frac{U_S}{d} = \frac{1}{d} \cdot U_X \quad (4.6)$$

where  $C_R$  is the capacitance of the reference capacitor,  $C_S$  is the capacitance of the sample.  $Q_S$  and  $Q_R$  represent the collected charges of the sample and the reference capacitor, respectively.  $U_S$  is the voltage drop across the sample.  $U_R$  is the voltage drop across the reference capacitor.  $U_X$  and  $U_Y$  are the voltages recorded by the oscilloscope in the X and Y channels. The typical triangular waveform with a 10 Hz frequency were selected.

---

### 4.4.3 Electrical Poling and Piezoelectric Measurement

---

In a microscopic crystalline structure that includes several such unit cells, the dipoles are by default found to be randomly oriented. When the material is subjected to an electric field, each dipole rotates from its original orientation toward a direction that minimizes the overall electrical and mechanical energy stored in the dipole. It is important to create an initial state in the materials such that most dipoles will be oriented in the same direction. This process of forcing the dipoles to orient themselves in a particular direction is called poling (see Fig. 4.7). During the poling, the sample is applied a very high electric field in order to all the dipoles followed the direction of the filed. Most dipoles are roughly oriented in the same direction when switching off the electric field.

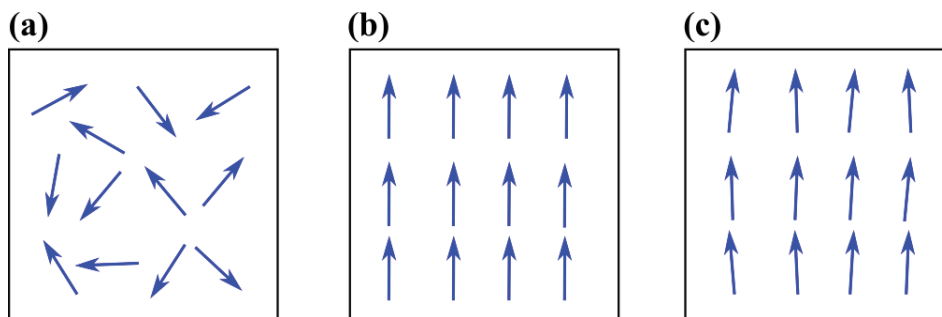


Fig. 4.7 Schematic of poling process of a crystal (a) Unpoled. (b) During poling. (c) Dipoles towards same direction after poling.

The BCTZ samples were first sputter-coated with gold electrodes. The sample was connected to electrodes with the power supply (TTi, EL-301R, Emona Instruments) switched off. The power supply was connected to a high voltage amplifier (Trek, model 20/20C, Medina, NY, USA), which provided precise control of output voltages. An Eco thermostat system (Lauda Eco Gold Re 415) was used for heating or cooling the samples in a silicone oil bath. The specified electric field was applied in the temperature range from above Curie point ( $T_c$ ) down to room temperature. The various BCTZ samples were poled at different electrical field amplitudes with a constant poling time of 30 minutes. The electric field was then set to zero. The samples were subsequently removed from the oil

bath. After poling process, the longitudinal direct piezoelectric coefficient  $d_{33}$  was measured using a Berlincourt  $d_{33}$  meter (PM3500, KCF Technologies, State College, PA).

---

## 4.5 Raman Spectroscopy

---

The Raman effect was discovered by C.V. Raman and K.S. Krishnan in 1928 [164]. Raman scattering is a fundamental form of molecular and solid state spectroscopy [165]. It is used to obtain information about the structure and properties of molecules from their vibration transitions [166].

The origin of Raman spectroscopy is an inelastic scattering effect through a photon-in photon-out process. In such case, the excitation radiation source is monochromatic. Both elastic and inelastic scattering by the sample are observed in a Raman experiment. In elastic scattering (Rayleigh scattering), the crystal is excited to a virtual state, and then relaxes to the original vibrational state by re-emitting a photon at the same frequency as the incident light ( $\hbar\omega_s = \hbar\omega_i$ ). There is no energy exchanged with the incident radiation in this case (see Fig. 4.8).

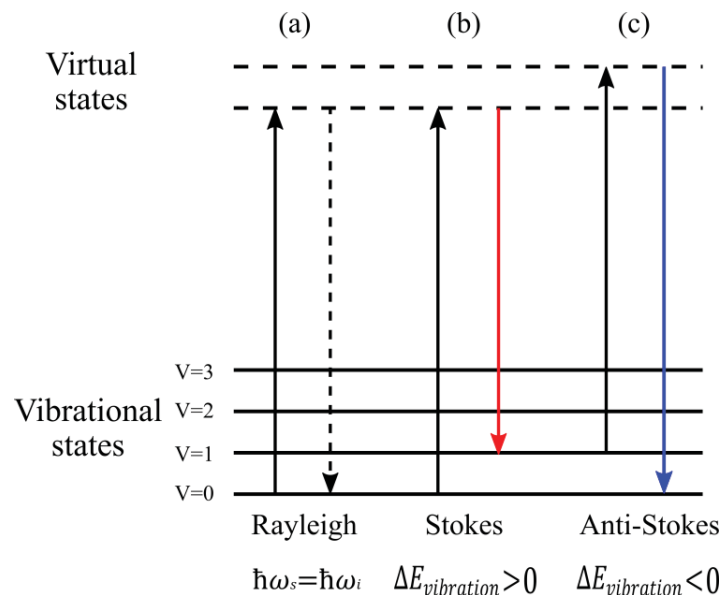


Fig. 4.8 Rayleigh and Raman scattering (a) Rayleigh scattering (b) Stokes Raman scattering (scattered photon has less energy than the incident photon) and (c) anti-Stokes Raman scattering (scattered photon has more energy than the incident photon).

Only a very small fraction of the light undergoes inelastic scattering (Raman scattering). When Raman scattering occurs, the excited crystal relaxes to a different vibrational level, rather than the initial state. The energy of the inelastically scattered photon is different from that of the incident light. In a Raman spectrum, the energy difference between the incident and scattered lights appears as a frequency shift between the scattered light ( $\omega_s$ ) and the incident light frequency ( $\omega_i$ ). Those two frequencies are related to the vibrational energy by the following equation:

$$h\omega_i = h\omega_s + \Delta E_{vibration} \quad (4.7)$$

In Raman experiments, the final vibrational state of the crystal can be either higher or lower in energy than the original state. In such case where the final vibrational state is higher in energy than the original state, the scattered photon will exhibit a lower frequency than the incident radiation. Thus, a red shift from the excitation frequency is observed. Raman bands of this type are called Stokes Raman scattering ( $\Delta E_{vibration} > 0$ ). Similarly, a blue shift from the incident radiation is observed when the final state exhibits lower energy than the initial state; these Raman bands are referred to as anti-Stokes Raman scattering ( $\Delta E_{vibration} < 0$ ). Since most of the molecules are at ground vibrational state ( $v=0$ ) at room temperature, the Stokes scattering exhibit higher Raman intensity than the corresponding anti-Stokes scattering, which originate from an excited vibrational state, for example  $v=1$ . Thus, the Stokes scattering are more commonly measured.

Porto's notation is a way to indicate the configuration of the Raman scattering experiment. It expresses the orientation of the crystal with respect to the polarization of the laser in both the excitation and analyzing directions [167]:

$$A(BC)D \quad (4.8)$$

where A and D present the directions of propagation of the incident light ( $k_i$ ) and scattered light ( $k_s$ ), respectively. B and C present the directions of polarization of the incident light ( $E_i$ ) and scattered light ( $E_s$ ), respectively. In a backscattering geometry, indicated that the incident and scattered light propagate in opposite direction, as shown in Fig. 4.9. The scattered light is analyzed by positioning an analyzer in front of the entrance of the spectrometer. The analyzer is oriented either along the Y-axis (parallel polarization) or the X-axis (crossed polarization).

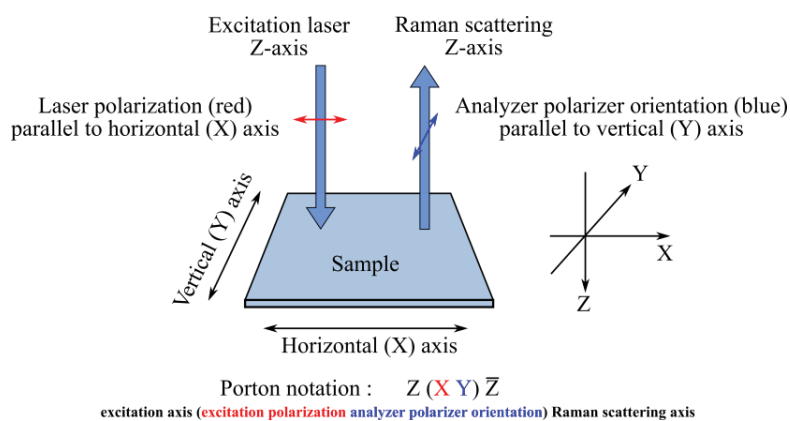


Fig. 4.9 Schematic of Porto notation.

Wavelength dependent Raman spectroscopy were carried out by using a Renishaw inVia Reflex Raman Microscope (Renishaw, UK) at room temperature. The monochromatic light is provided by four laser excitation sources: a Helium-Cadmium laser (325/442 nm), a frequency doubled Nd: YAG (532 nm) laser, a Helium-Neon (633 nm) laser, and a diode laser (785 nm). Raman spectra were recorded in backscattering geometry.

Temperature dependent Raman spectroscopy were performed with a Cryostat (Microstat Hires, Oxford Instruments, UK), which allows a temperature range from 4K to room temperature. The cryostat is connected with a MercuryTC temperature controller (Oxford Instruments, UK). The cell is cooled with liquid helium for low temperature.

# 5 Crystal Growth and Characterization of CaTiO<sub>3</sub>

---

## 5.1 Crystal Growth

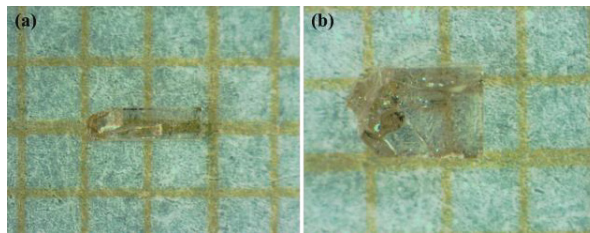
---

The mineral perovskite CaTiO<sub>3</sub> is an end member of BCTZ system. There was a significant amount of research works reported on CaTiO<sub>3</sub> [36, 110, 133, 134, 168-172]. Bulk crystals can be grown by various techniques, such as flux method [134], optical floating zone technique [171] and laser heater pedestal growth [110], etc. Hence, owing to its high melting point, the growth of CaTiO<sub>3</sub> was both investigated by flux method and by mirror furnace.

### 5.1.1 Crystal Growth by Flux Method

---

The CaTiO<sub>3</sub> single crystals were grown at FEE GmbH by the flux technique using a LiF-KF solvent as previously reported [173]. A starting mixture consisting of 100.8 g KF, 45.0 g LiF, 11.85 g CaO, and 12.85 g TiO<sub>2</sub> was set in a platinum crucible and heated to 1250 °C in air. Following a 4-hour soaking at this temperature, the system was cooled at a rate of 1 °C.h<sup>-1</sup> down to 875 °C. Single crystals of CaTiO<sub>3</sub> were obtained by spontaneous nucleation and were found trapped in the solidified LiF-KF mixture flux. Crystals were easily extracted from the flux, which is soluble in hot water. Crystal faces were naturally orientated along (100)<sub>pc</sub> direction as displayed on Fig. 5.1. As-grown single crystals were millimeter-sized and were colored probably due to fluor-based impurities as previously observed in BaTiO<sub>3</sub> crystals grown from KF solutions by Remeika method [117, 174, 175]. No further characterization was possible on these crystals.



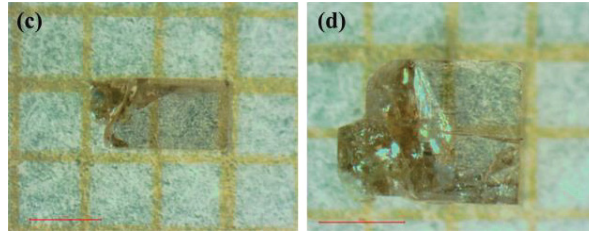


Fig. 5.1: As-grown  $\text{CaTiO}_3$  single crystal grown from LiF-KF solution. Natural flat faces are oriented along  $(100)_{\text{pc}}$  crystallographic direction. Scale bar: 1 mm.

---

### 5.1.2 Crystal Growth by Optical Floating Zone Furnace

---

The starting materials used for the preparation of feed rods for  $\text{CaTiO}_3$  were  $\text{CaCO}_3$  and  $\text{TiO}_2$  with high-purity (99.99%). Stoichiometric amounts of the raw materials were thoroughly ground together ( $\text{CaCO}_3 + \text{TiO}_2$ ) and then synthesized in a horizontal furnace at  $500\text{ }^\circ\text{C}$  for 6 hours in air to remove  $\text{CO}_2$  at first. Then the mixture was calcined at  $1300\text{ }^\circ\text{C}$  for 24 hours, with intermediate grinding. After phase identification using XRD, calcined powders were used for feed rod preparation. To make polycrystalline rods for the floating zone growth, approximately 10 g of calcined powders was packed into a thin rubber tube and sealed in the metallic tube while being evacuated using a vacuum pump. The powder was compacted into a rod, typically 6mm in diameter and 50mm long, by placing the sealed tube containing the powder in a hydraulic press under an isostatic pressure ( $P = 50\text{ MPa}$ ) (see Fig. 5.2(a)). After removal from the rubber tube, the compacted rod was sintered in a horizontal alumina container at  $1400\text{ }^\circ\text{C}$  for 12 hours in air. Finally, the rod was drilled at one end and hung to a platinum wire (see Fig. 5.2 (b)).

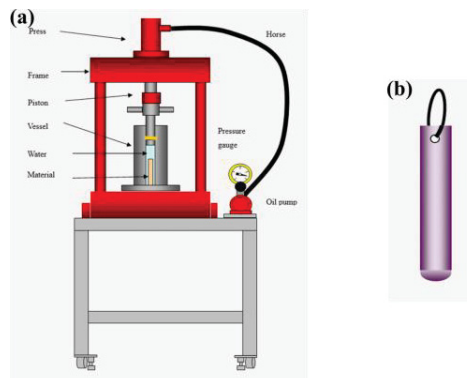


Fig. 5.2: (a) Preparation of the compacted rod. (b) Feed rod with a platinum wire after sintering.

Growth attempts of  $\text{CaTiO}_3$  crystals have been carried out at ICMMO (Institut de Chimie Moléculaire et des Matériaux d'Orsay, Paris, France), with Dr. Raphaël Haumont and Dr. Romuald Saint-Martin. The apparatus employed for the floating zone crystal growth was an image furnace from Crystal System Inc, (model FZ-T-4000-H-II-PP, Kobuchisawa, Japan) (see Fig. 5.3(a)). In this system, the four halogen lamps minimize the temperature gradient and allow the achievement of the most uniform temperature profile around the sample compared to a one- or a two-mirror furnace. (see Fig. 5.3 (b)).

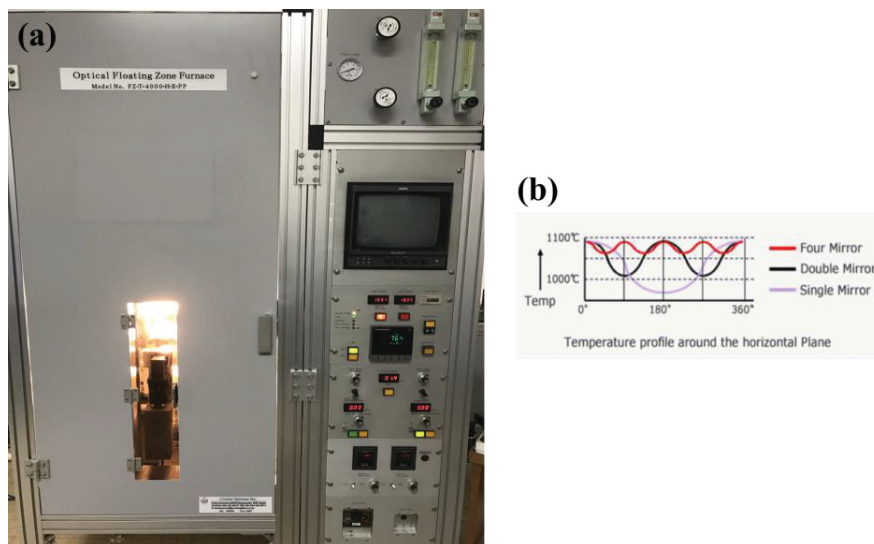


Fig. 5.3: (a) Experimental device from Crystal System Inc. (b) Schematic temperature profile in one-, two-, and four-mirror furnace.

Initially, a polycrystalline rod was used as seed and once good quality boules were obtained, a crystal seed was used for subsequent growths. The sample feed rod was hung from the upper shaft and the seed rod was fastened to the lower shaft. The two rods (feed and seed) were contra-rotated at a rate of 18 rpm (upper) and 10 rpm (lower), respectively. The lamps were moved as well as their power was adjusted so that the feed rod's tip was melted, and then connected to the seed rod's tip (see Fig. 5.4).

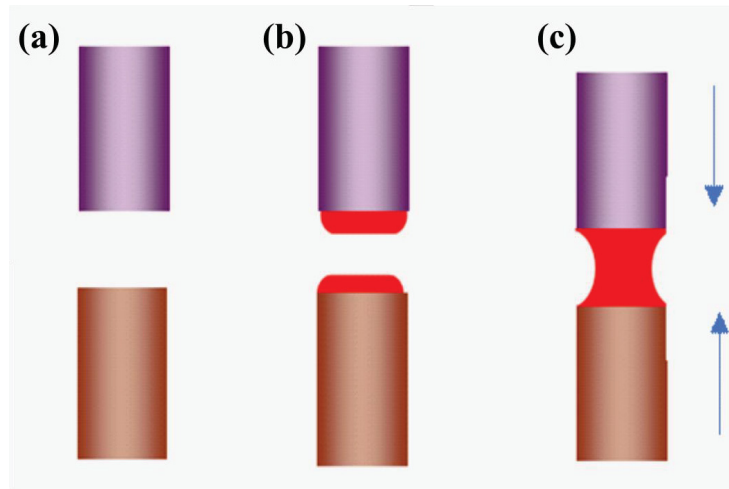


Fig. 5.4: (a) Feed and seed rods. (b) Beginning of melting of the rods before connection. (c) Connected rods.

The molten region was stabilized and becomes a “floating zone” (see Fig. 5.5 (a)), which was a section of the molten material suspended between the two rods by surface tension. The lamps were moved up to create the molten zone leveling along the sample. All the crystals were prepared using a growth rate in the range of 2-4 mm.h<sup>-1</sup> under air condition based on the previous works performed at ICMMO [176]. The as-grown CaTiO<sub>3</sub> crystals were transparent and red-brownish colored (see Fig. 5.5 (b)).

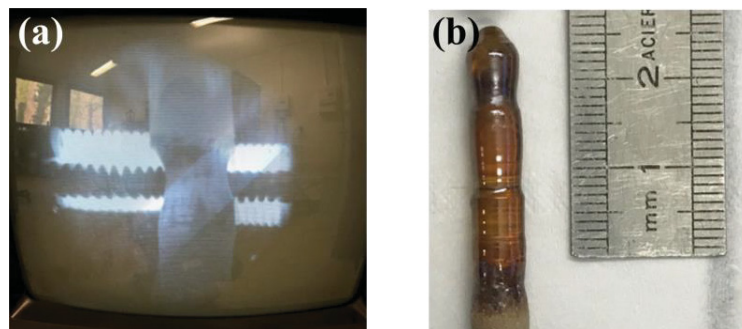


Fig 5.5 (a) Initial stage of the process: the feed and seed rod are brought into contact by careful melting. (b) Large CaTiO<sub>3</sub> single crystal grown by the optical floating zone technique.

---

## 5.2 Structural Analysis

---

Fig. 5.6 shows the Le Bail fit obtained by X-ray powder diffraction performed on a crushed as-grown  $\text{CaTiO}_3$  single crystal. The  $\text{CaTiO}_3$  sample has an orthorhombic structure with space group  $Pbnm$  ( $n^\circ 62$ ). The lattice parameters are  $a = 5.377 \text{ \AA}$ ,  $b = 5.439 \text{ \AA}$  and  $c = 7.637 \text{ \AA}$ . It is noted that X-ray powder diffraction of as-grown  $\text{CaTiO}_3$  crystal is consistent with previously reported results in ICSD #62149 ( $\text{CaTiO}_3$ ).

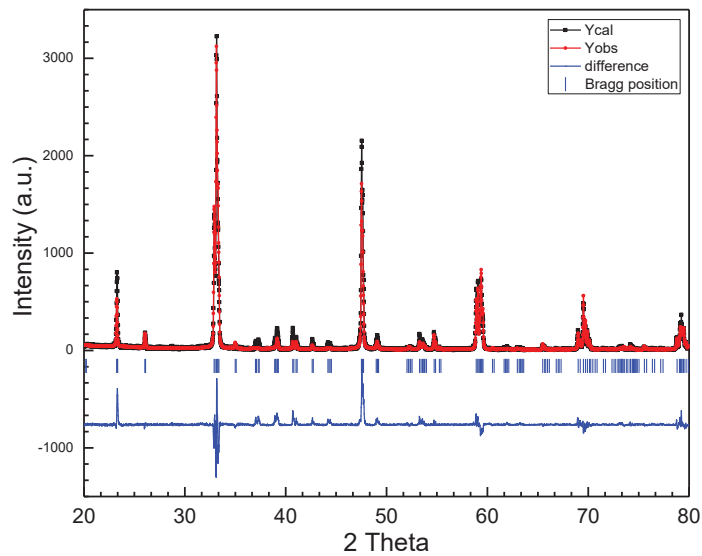


Fig. 5.6 XRD powder diffraction diagram of the grown  $\text{CaTiO}_3$ .  $Y_{\text{obs}}$  and  $Y_{\text{cal}}$  correspond to the observed and calculated data, respectively. A plot of differences ( $Y_{\text{obs}} - Y_{\text{cal}}$ ).

A piece of  $\text{CaTiO}_3$  crystal was cut from the  $\text{CaTiO}_3$  single crystal rod. Fig. 5.7 shows the Laue diffraction pattern of the  $\text{CaTiO}_3$  single crystal. The pattern shows diffraction spots which indicate the single crystal nature of the material since no diffraction rings can be observed. In addition, no splitting spots was observed, indicating thus the apparent good crystallinity of the material. By using the Orientexpress software [157] which simulates theoretical Laue patterns, we have generated  $\text{CaTiO}_3$  theoretical pattern that we make match perfectly over the Laue experimental pattern.  $\text{CaTiO}_3$  is oriented roughly towards

the  $(100)_{pc}$  direction, which is also indicated the natural growth direction of  $\text{CaTiO}_3$  when using a polycrystalline seed.

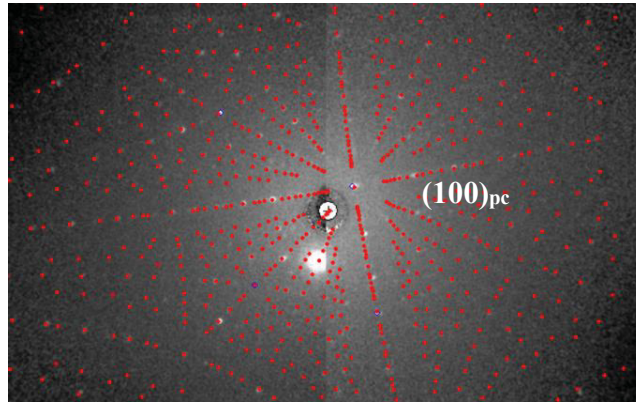


Fig. 5.7 Laue diffraction pattern of the grown  $\text{CaTiO}_3$  single crystal. Red spots corresponding to theoretical pattern match with white experimental spots.

---

### 5.3 Chemical Analysis

---

The impurity content of the  $\text{CaTiO}_3$  crystal was determined by GDMS. The measured the final as-grown concentration are listed in Table 5.1.

Table 5.1 Values of impurities measured by GDMS in ppm at. (mol).

Element	Concentration ppm at. (mol)
Li	16.7
<b>O</b>	<b>X</b>
Na	3.3
<b>Mg</b>	<b>179.0</b>
<b>Al</b>	<b>221.7</b>
Si	7.7
P	0.8
S	3.6
Cl	0.2
<b>Ca</b>	<b>X</b>
Sc	0.4
<b>Ti</b>	<b>X</b>

V	2.3
Cr	31.4
Fe	29.2
Co	1.2
Ni	1.3
Cu	3.4
Zn	1.9
Rb	1.0
Zr	14.6
<b>Ba</b>	<b>99.0</b>
La	0.2
Ce	2.3
Nd	0.2
Sm	0.2
Eu	0.3
Gd	1.2
Tb	0.7
Yb	0.1
Lu	0.1

From the results, we found that the dominant impurities of CaTiO<sub>3</sub> single crystal were Al, Mg and Ba.

EPMA was complementally performed to determine average elemental composition (mol%) of as-grown CaTiO<sub>3</sub> crystal (Table.5.2). A piece of CaTiO<sub>3</sub> crystal about 6 mm in diameter, cut from the CaTiO<sub>3</sub> single crystal rod, was used.

Table 5.2 Average atomic composition of as-grown crystal.

<b>Crystal</b>	<b>Ca (%)</b>	<b>Ti (%)</b>	<b>O (%)</b>
CaTiO <sub>3</sub>	20.28	19.83	59.90
Theory	20	20	60

At this scale of analysis, EPMA indicated that chemical ratio between the different cations Ca, Ti and O are very close to the expected ones. This gives an evidence of homogenous chemical composition inside the crystal.

---

## 5.4 Raman Study of a CaTiO<sub>3</sub> Single Crystal

---

We cut and polished a plate of CaTiO<sub>3</sub> with 0.5 mm thickness and 6 mm in diameter in order to carry out the Raman measurements. The excitation wavelength was 633 nm from a He-Ne laser source. Power of 9.2 mW was incident on the sample in a 0.86  $\mu\text{m}$  diameter spot through a standard microscope objective lens with magnitude  $\times 100$ . The spectra were collected with 50s data point acquisition time over a spectral range of 100 – 800  $\text{cm}^{-1}$ , as shown in Fig. 5.8

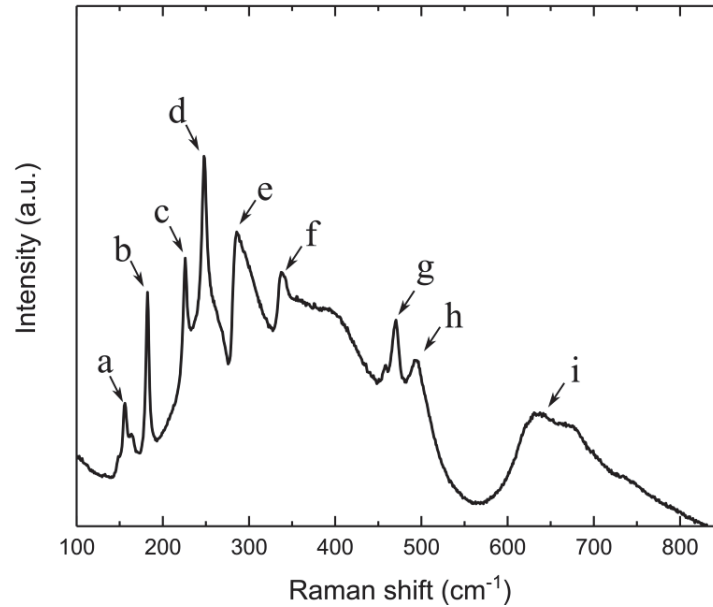


Fig. 5.8 Raman spectrum (unpolarized) of CaTiO<sub>3</sub> single crystal at room temperature.

The Raman active phonon modes of crystallographic phase were predicted by factor group analysis, and the results are presented in Table 5.3. As mentioned before, CaTiO<sub>3</sub> single crystal is orthorhombic with space group  $Pbnm$ . Theoretically, the total 60  $\Gamma$ -point phonon modes, 24 ( $7A_g + 5B_{1g} + 7B_{2g} + 5B_{3g}$ ) [177-179] are Raman-active, 25 ( $9B_{1u} + 7B_{2u} + 9B_{3u}$ ) are infrared-active, 8 ( $8A_u$ ) are silent, and 3 ( $B_{1u} + B_{2u} + B_{3u}$ ) are acoustic modes.

Table 5.3 Factor group analysis and selection rules for the zone-center vibrational modes.

Atom	Number of equivalent positions (Wyckoff notation)	Site symmetry	Irreducible representations
Ca	4(c)	$C_s$	$2A_g + B_{1g} + 2B_{2g} + B_{3g} + A_u + 2B_{1u} + B_{2u} + 2B_{3u}$
Ti	4(b)	$C_i$	$3A_u + 3B_{1u} + 3B_{2u} + 3B_{3u}$
O1	4(c)	$C_s$	$2A_g + B_{1g} + 2B_{2g} + B_{3g} + A_u + 2B_{1u} + B_{2u} + 2B_{3u}$
O2	8(d)	$C_1$	$3A_g + 3B_{1g} + 3B_{2g} + 3B_{3g} + 3A_u + 3B_{1u} + 3B_{2u} + 3B_{3u}$

#### Modes classification

$$\Gamma_{\text{Raman}} = 7A_g + 5B_{1g} + 7B_{2g} + 5B_{3g} \quad A_g: \sigma_{xx}, \sigma_{yy} \text{ and } \sigma_{zz}$$

$$\Gamma_{\text{IR}} = 9B_{1u} + 7B_{2u} + 9B_{3u} \quad B_{1g}: \sigma_{xy}$$

$$\Gamma_{\text{acoustic}} = B_{1u} + B_{2u} + B_{3u} \quad B_{2g}: \sigma_{xz}$$

$$\Gamma_{\text{silent}} = 8A_u \quad B_{3g}: \sigma_{yz}$$

The Raman spectrum of  $\text{CaTiO}_3$  (see Fig. 5.8) shows a number of sharp peaks superimposed to a lower broad feature between  $150$  and  $550 \text{ cm}^{-1}$ , and a second broad band between  $600 \text{ cm}^{-1}$  and  $800 \text{ cm}^{-1}$ . This is in accordance with the spectra obtained by McMillan and Ross [180] and Gillet *et al.* [170], also similar to the band position reported by Balachandran and Eror [181] and Hirata *et al.* [182]. Here, 9 Raman modes are observed in Table 5.4. Fewer bands are observed in the Raman spectrum than those which were predicted by the factor group analysis. This is due to i) band overlapping of the numerous Raman modes, ii) small distortions from the cubic perovskite which may result in narrow splittings and low intensities for some Raman modes, and iii) an intense background scattering [171]. Guennou *et al.* [171] showed a similar spectrum of  $\text{CaTiO}_3$  at room temperature where assigned the two broad bands to a second-order scattering processes, by analogy with cubic perovskite  $\text{SrTiO}_3$  [170, 180, 183] in which a very similar background is observed although first-order Raman modes are forbidden by symmetry.

Table 5.4 Frequencies ( $\text{cm}^{-1}$ ) of unpolarized Raman bands and their assignments for  $\text{CaTiO}_3$  perovskite.

Bands assignment	Ref. 78	Ref. 79	Ref. 80	Ref. 81	This work	Labels correspond to Fig. 5.4
Ca- $\text{TiO}_3$ lattice mode	154	155	155		156	a
O-Ti-O bending modes	181	181	180	175	182	b
	225	226	226	224	226	c
	246	248	247	244	248	d
	284	290	286	286	286	e
	337	340	337	336	337	f
Ti- $\text{O}_3$ torsional modes	469	470	471	471	470	g
	493	496	495	492	493	h
Ti-O symmetric stretching		640	639		638	i

## 5.5 Conclusion

$\text{CaTiO}_3$  single crystals were grown by both flux technique and optical floating zone technique. GDMS reveals Al, Mg and Ba as main impurities in as-grown  $\text{CaTiO}_3$  crystal grown by optical floating zone furnace. Furthermore, EPMA analysis indicated that chemical ratio between them are very closed to the expected. The Raman spectra of  $\text{CaTiO}_3$  is in good agreement with the spectra referenced in the literature.

# 6 Crystal Growth and Characterization of BaZrO<sub>3</sub>

---

## 6.1 Crystal Growth

---

Owing to its large lattice constant, high melting point, low thermal expansion coefficient, low dielectric loss, and low thermal conductivity [184-186], BaZrO<sub>3</sub> has become very attractive and popular for fundamental research and device applications. More particularly, BaZrO<sub>3</sub> is known to be used in lead-free BaTiO<sub>3</sub>-based (BCTZ) [187] solid solution which exhibits, unexpectedly, high piezoelectric response [12] because the polarization mechanisms impacted by BaZrO<sub>3</sub> remains poorly understood at the phase convergence region of this system [86]. Hence, for a better understanding of the giant piezoelectric response of BCTZ solid solution, it is of great importance to measure the intrinsic properties [186] of BaZrO<sub>3</sub> in order to comprehend and to model more accurately BaTiO<sub>3</sub>-CaTiO<sub>3</sub>-BaZrO<sub>3</sub> phase diagram as previously reported [188-190].

In this chapter, the growth of BaZrO<sub>3</sub> single crystals by two methods, the flux method and the optical floating zone technique were investigated. The properties of the crystals obtained by the optical floating zone technique were compared to those of commercial crystals with same orientation.

### 6.1.1 Crystal Growth by the Flux Method

---

The flux method from high temperature solution is investigated in order to decrease the crystallization temperature of BaZrO<sub>3</sub>. As suggested by the BaTiO<sub>3</sub>-BaB<sub>2</sub>O<sub>4</sub> phase diagram referenced by Goto *et al.* [99] and since B ions cannot be inserted into the BaTiO<sub>3</sub> lattice as a foreign element, BaB<sub>2</sub>O<sub>4</sub> (BBO) could be used as a suitable self-flux [191] to grow BaTiO<sub>3</sub> down to 942 °C, which is more than 650 °C below the BaTiO<sub>3</sub> melting point (T<sub>F</sub>=1618 °C). Although the detailed BaZrO<sub>3</sub>-BBO phase diagram remains unknown, we

assumed that BaZrO<sub>3</sub>-BBO system exhibits the same phase diagram feature than that of BaTiO<sub>3</sub>-BBO because of the chemical similarity of Ti<sup>4+</sup> and Zr<sup>4+</sup> cations. Therefore, BaZrO<sub>3</sub>:BBO mixtures were investigated for different molar ratios such as 10:90, 20:80, 30:70, 35:65, 40:60 and 50:50, in order to characterize the solubility of BaZrO<sub>3</sub> in BBO. BBO flux was prepared by solid state reaction [192] by mixing BaCO<sub>3</sub> (Alfa Aesar, 99.95 %) and B<sub>2</sub>O<sub>3</sub> (Alfa Aesar, 99.98 %). Then, BBO was mixed with BaZrO<sub>3</sub> commercial powder (Fox-Chemicals GmbH, 99.9 %). 10 g ball-milled mixtures were placed into a platinum crucible tightly covered with a platinum lid and placed in a large alumina crucible. A two-heating-resistive-zone furnace was used to achieve a 1 °C.cm<sup>-1</sup> longitudinal thermal gradient. The process was performed in the following steps: i) an increasing temperature ramp of 120 °C.h<sup>-1</sup> up to 1350 °C, with a 1-hour dwelling time at this temperature, ii) a decreasing ramp with 1 °C.h<sup>-1</sup> down to 1250 °C, and finally, iii) the mixtures were cooled down at a rate of 30 °C.h<sup>-1</sup> down to room temperature. The mass of the crucible containing the mixtures was monitored all along the thermal process.

In all cases, a strong volatilization as well as flux creeping outside of the crucible were observed with a loss of approximately one half of the total weight of the loads (see Fig. 6.1).

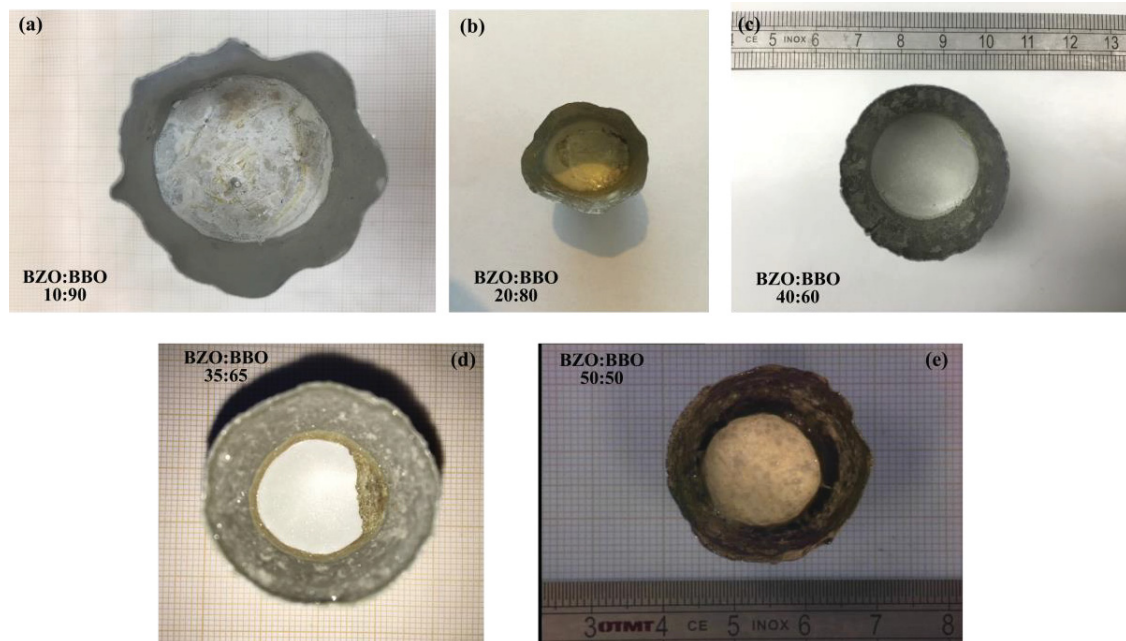


Fig. 6.1 BaZrO<sub>3</sub>:BBO mixtures with different molar ratios (a) 10:90 (b) 20:80 (c) 40:60 (d) 35:65 (e) 50:50. No picture was taken for BaZrO<sub>3</sub>:BBO mixture with a molar ratio 30:70 but it looks similar than that of 20:80.

In the lower-BaZrO<sub>3</sub>-content solutions corresponding to 10:90, 20:80 and 30:70 BaZrO<sub>3</sub>-BBO mixtures, no BaZrO<sub>3</sub> crystallites were detected. In the particular case of 10:90 BaZrO<sub>3</sub>-BBO solution, millimeter-sized yellow single crystals, with (111)-natural facets corresponding to rhombohedral BaZr(BO<sub>3</sub>)<sub>2</sub> (BZB) phase, were extracted from the solidified solution (Fig. 6.2 (d)).

Higher-BaZrO<sub>3</sub>-content solutions corresponding to 35:65, 40:60 and 50:50 BaZrO<sub>3</sub>-BBO mixtures displayed two solidified zones with white and brown colors (Fig. 6.2 (a)). In the brown zone, BaZrO<sub>3</sub> single crystals were successfully obtained (Table 6.1) and their structure has been confirmed by single crystal XRD with space group  $Pm\bar{3}m$  and  $a=4.18$  Å.

The largest BaZrO<sub>3</sub> crystals with size up to 150-200 μm (Fig. 6.2 (b)) were found in the brown zone from the 35:65 BaZrO<sub>3</sub>-BBO solution whereas crystallites with micrometric-sized were detected with 40:60 and 50:50 BaZrO<sub>3</sub>-BBO solutions.

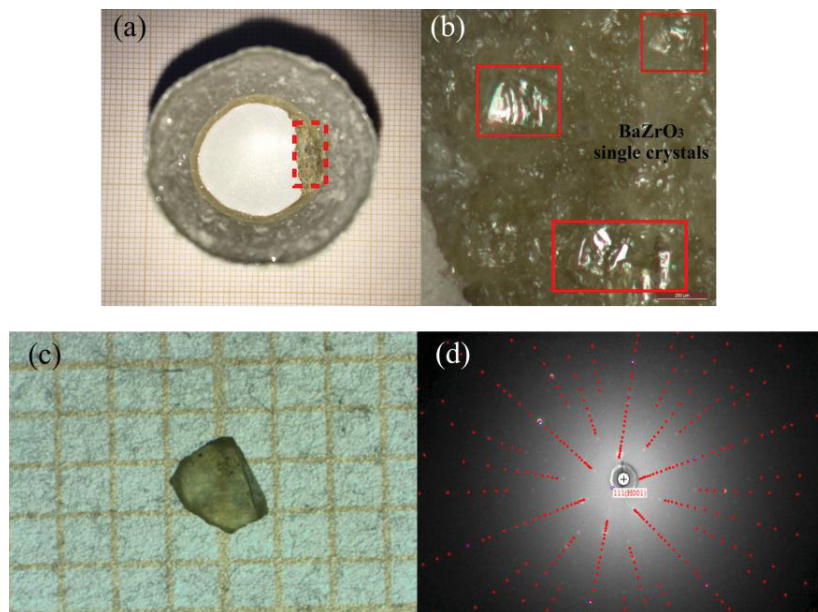


Fig. 6.2: Flux growth with 35:65 BaZrO<sub>3</sub>-BBO solution: (a) Crucible containing the solution (white zone) and the BZO crystals (brown zone). (b) Zoom on BZO single crystals (brown region); (c) BaZr(BO<sub>3</sub>)<sub>2</sub> single crystals grown from 10:90 BaZrO<sub>3</sub>-BBO solution with (d) (111)-natural faces highlighted in a Laue pattern (red dots correspond to theoretical pattern whereas white dots correspond to experimental pattern). (111) rhombohedral faces correspond to (001) hexagonal face, noted (H001).

Table 6.1 Mixtures of BaZrO<sub>3</sub>-BaB<sub>2</sub>O<sub>4</sub> with different molar ratio regarding the typical size of BZO crystals grown in the tightly lid-covered crucible.

Mixture BaZrO <sub>3</sub> :BBO (mol%)	Presence of BZO	BZO crystals typical size
10 : 90	×	×
20 : 80	×	×
30 : 70	×	×
35 : 65	✓	~150μm
40 : 60	✓	~10μm
50 : 50	✓	~10μm

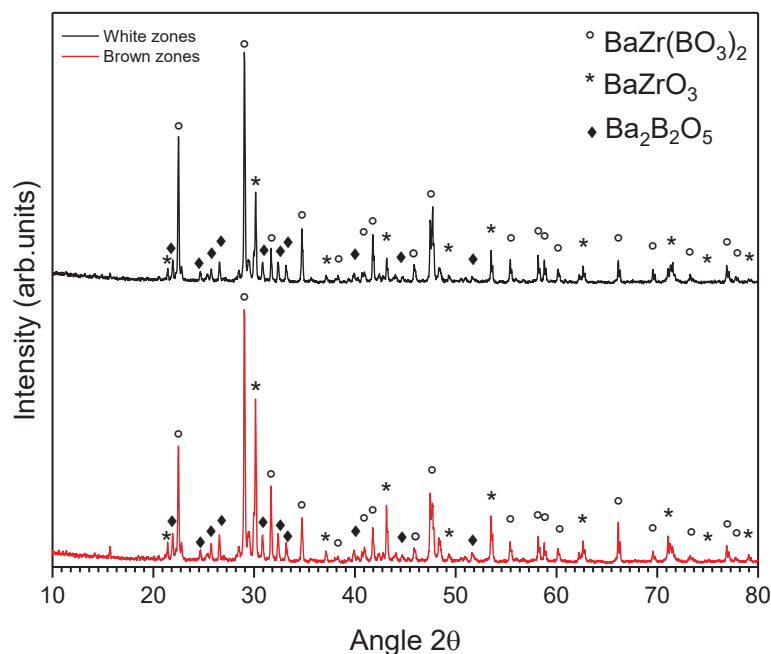


Fig. 6.3: XRD patterns of crushed sample extracted from the brown zone (red pattern) and the white zone (black patterns) obtained from the flux growth attempt into a tightly lid-covered platinum crucible with 35:65 BZO-BBO solution.

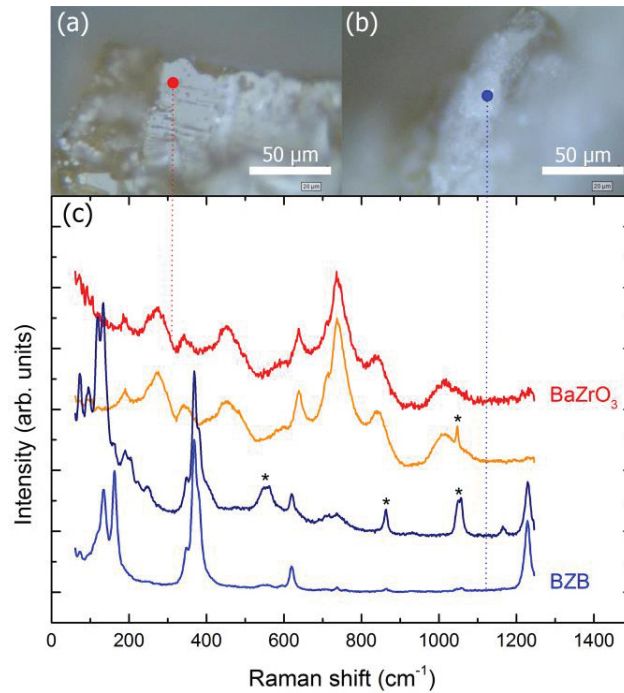
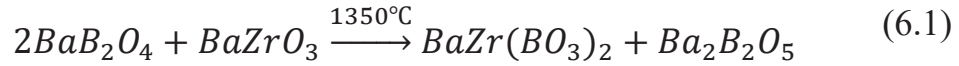


Fig. 6.4. Selected Raman spectra recorded in different parts of the flux grown crystals. (a) and (b) show two representative spots where the spectra of BaZrO<sub>3</sub> and BZB can be observed as indicated in (c), together with other spectra showing mixed cases and Raman bands (marked with a star) that are tentatively assigned to Ba<sub>2</sub>B<sub>2</sub>O<sub>5</sub>.

XRD diffractograms (Fig. 6.3) display BaZrO<sub>3</sub>, Ba<sub>2</sub>B<sub>2</sub>O<sub>5</sub> and BZB phases in both white and brown zones with a higher proportion of BaZrO<sub>3</sub> in the brown zone where single crystals were detected and collected. Micro-Raman spectroscopy was performed on the as-grown crystals from the 35:65 BaZrO<sub>3</sub>-BBO solution (Fig. 6.4). Crystals with large flat facets exhibit a spectrum that matches previously reported Raman spectra of BaZrO<sub>3</sub> [193-195]. The spectrum of BZB [195] was also confirmed, consistently with the XRD analysis. Some additional spectral features are observed but cannot be conclusively identified. In particular, they do not match the Raman spectrum expected from the BBO flux [196] or ZrO<sub>2</sub> [197]. We may tentatively attribute it to the Ba<sub>2</sub>B<sub>2</sub>O<sub>5</sub> detected in XRD, but no

reference Raman spectrum is available in the literature to confirm this hypothesis. We conclude that a chemical reaction occurs between BZO and BBO at 1350 °C and it is described by the following equation:



Furthermore, in order to increase the crystal size by avoiding the flux creeping and its volatilization from the solution, a crystal growth was performed with BaZrO<sub>3</sub>-BBO 35:65 molar ratio under controlled atmosphere in a sealed and gas-proof platinum assembly for saturating the vapor pressure as previously reported by Albino *et al.*[198]. The same thermal protocol was performed as above-mentioned. After thermal process, XRD analysis revealed the presence of BaZrO<sub>3</sub>, BBO and BZB compounds in the solidified solution (see Fig. 6.5) without any visible BaZrO<sub>3</sub> single crystal under microscope (X64). This confirms that the solubility of BaZrO<sub>3</sub> in BBO is very low and below the XRD detection limit. In addition, this suggests that the flux volatilization was the driving force governing the growth of BaZrO<sub>3</sub> obtained in the tightly lid-covered crucible.

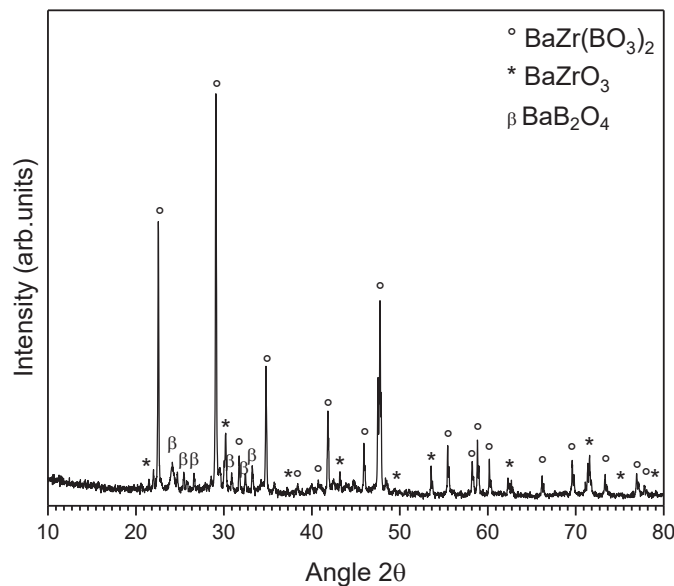


Fig. 6.5: XRD pattern of crushed sample from the flux growth attempt into a sealed platinum crucible with 35:65 BZO-BBO solution.

Finally, we noted that the formation of BZB is systematically observed, whatever the platinum assembly used. The chemical reaction in between BBO and  $\text{BaZrO}_3$  decreases the amount of the latter in the BBO-based solution, partly impeding then its growth at 1350 °C. Hence, a growth attempt was performed with BZB as a self-flux with  $\text{BaZrO}_3$ -BZB 50:50 molar ratio. BZB was synthesized by solid state reaction [199] and mixed to  $\text{BaZrO}_3$  commercial powder. The load was held in an open iridium crucible under argon atmosphere, for 12 hours at a temperature ranging in between 1550 °C - 1640 °C measured through pyrometric measurement. A strong volatilization of the solution was observed, prohibiting the growth of  $\text{BaZrO}_3$  single crystal from BZB flux. Indeed, XRD analysis (Fig. 6.6) revealed the presence of only  $\text{BaZrO}_3$  and  $\text{ZrO}_2$  phases resulting likely from the decomposition of BZB at high temperature. We infer that the high thermal chemical stability of  $\text{BaZrO}_3$  makes it difficult to dissolve in the investigated Ba-based flux of the present work.

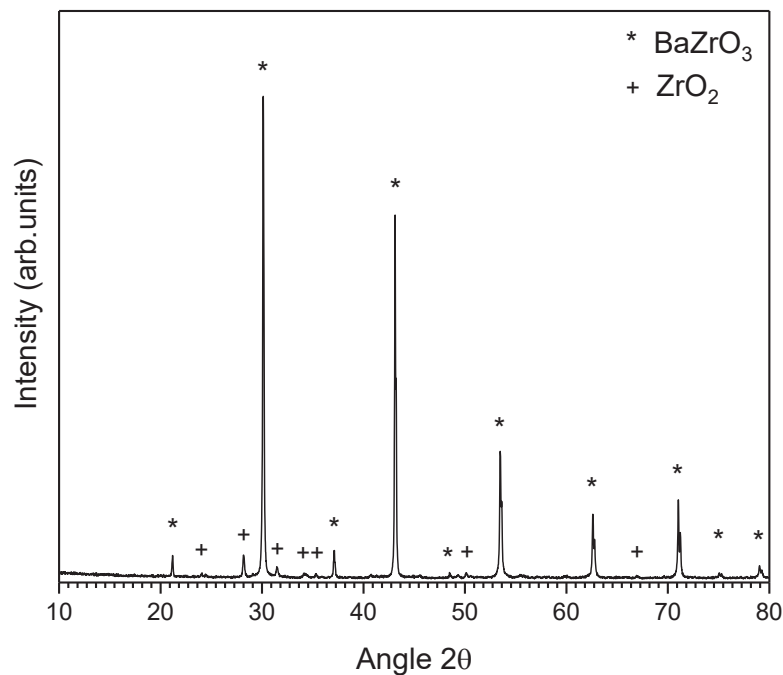


Fig. 6.6: XRD pattern of crushed sample from the flux growth attempt into an open iridium crucible with 50:50 BZB-BZO solution.

---

## 6.1.2 Crystal Growth by the Optical Floating Zone Technique

---

Feed rods were prepared with BaZrO<sub>3</sub> commercial powder (Fox-Chemicals GmbH, 99.9 %). The powder was sealed in a rubber tube and pressed under hydrostatic pressure around 50 MPa. Compacted cylindrical rods were then sintered in a horizontal furnace at 1200 °C for 24 hours under air atmosphere leading to sintered feed rods about 6.5 mm in diameter and 65 mm in length. X-ray diffraction performed on crushed pieces of sintered rods confirmed the presence of the cubic perovskite BaZrO<sub>3</sub> phase without any other secondary phases.

BaZrO<sub>3</sub> was grown using a four-mirror furnace equipped with xenon arc lamp (3 kW) (CSI FZ-T-12000-X\_VI-VP, Crystal Systems Incorporated, Japan) in collaboration with Warwick University (England). The crystal growths were carried out under dynamic argon atmosphere with pressure in the range 5-6 bars. A polycrystalline BaZrO<sub>3</sub> sintered rod was used as seed. Once a good quality boule was obtained, a crystal seed was used for subsequent growths. The crystal boules were obtained with a growth rate of 18-25 mm.h<sup>-1</sup>. The two rods, the feed rod and the seed, were counter rotated at a rate of 5–15 rpm.

Despite the use of a high gas pressure, a white colored deposition was observed on the quartz tube surrounding the feed and the seed rods, indicating the evaporation of BaO during the growth process as usually observed in zirconia-based systems [200-202] at high temperature. The as-grown BaZrO<sub>3</sub> boules were polycrystalline and mostly opaque and white colored (Fig. 6.7 (a)) close to the seed, at the beginning of the growth. As the growth progressed, the boules produced single crystals and developed facets. Without any post-treatment annealing, as-grown single crystals are transparent to light, colorless and size up to 6 mm long (Fig. 6.7 (b)). A single crystal, namely BZO#1, about 1.99 × 1.80 × 0.6 mm<sup>3</sup> (Fig. 6.7 (c)) oriented along (100) (Fig. 6.7 (d)) was extracted from the grown boule and optically polished for further investigations. Its properties were compared to those of two commercial samples, namely BZO#2 and BZO#3, (Fig. 6.7 (e) and (f)) purchased from Crystal Base company (Japan).

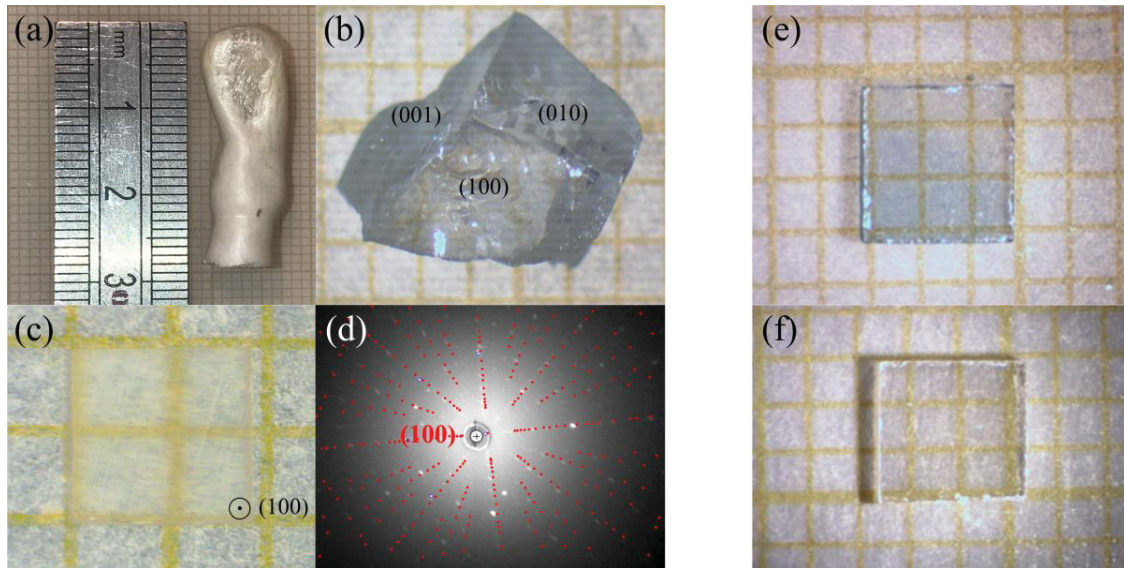


Fig. 6.7: (a) Chunk of the end of a BaZrO<sub>3</sub> boule grown by floating zone method. (b) 6-mm long BaZrO<sub>3</sub> single crystal extracted at the end of the boule. (c) Cut and (100)-oriented BaZrO<sub>3</sub> single crystal (BZO#1)  $\sim 1.99 \times 1.80 \times 0.6 \text{ mm}^3$  (d) Back-scattered Laue diffraction pattern of BaZrO<sub>3</sub> single crystal with (100) orientation. Red dots correspond to the theoretical Laue pattern. (e) BZO#2 commercial sample (top right here). (f) BZO#3 commercial sample (bottom right here).

---

## 6.2 Chemical Analysis

---

### 6.2.1 Energy Dispersive X-ray Analysis

---

We have performed Energy Dispersive X-ray Analysis (EDX) to analyze the possible existence of local variations of chemical compositions. These results are shown in Table 6.2.

No significant variations can be detected between the three BZO samples, at this scale of analysis. Oxygen content is slightly less in BZO#1 compared to that of BZO#2 and BZO#3 samples. Moreover, Hf impurities was detected in all samples. On the other hand, the BZO#2 commercial sample exhibits a blue color gradient. However, EDX analysis

performed on two different areas do not reveal significant composition variations. Because of the detection limit of EDX, other impurities have not been detected.

Table. 6.2 Atomic composition obtained by EDX analysis, performed on BZO samples.

Sample	O %	Ba %	Zr %	Hf %
BZO#1	48.11	21.83	29.72	0.35
BZO#2 (Blue area)	52.92	20.94	25.85	0.3
BZO#2 (colorless area)	53.42	20.39	25.87	0.34
BZO#3	52.97	20.57	26.18	0.28

## 6.2.2 Glow Discharge Mass Spectrometry Analysis

The concentration of impurities in a 0.269 g-BZO#1 single crystal was measured by GDMS. The result of main impurities contents is summarized in Table 6.3. Dominant impurities in BZO#1 were found to be Ca, Ti, Sr and Hf. It is worth mentioning that Fe content is very low compared to what is usually measured in oxide single crystals [203-205] grown from crucible-based techniques with a highly polluting refractory material environment at high temperature.

Table 6.3: GDMS analysis results of the impurity content in a 0.269 g BZO#1 single crystal (ppm at.)

Element	B	Mg	Al	Si	P	S	Cl	K	Ca	Fe	Ti	Sr	Hf
BZO#1	0.8	3.4	6.2	47.3	1.5	7	15.6	4.5	179.4	1.3	370	1420	3001

---

### 6.2.3 Secondary Ion Mass Spectrometry Analysis

---

Fig. 6.8 shows the secondary ion yield variations observed as a function of sputtering time  $t_s$  under oxygen bombardment into  $\text{BaZrO}_3$  samples BZO#1, BZO#2 and BZO#3.  $t_s$  is directly proportional to the distance  $z$  normal to the samples surface (about 120 nm in Fig. 7). From the results shown in Fig. 6.8, the intensities of most ions stabilize quite rapidly, except Ti and Ca in BZO#2 and BZO#3 single crystals. Comparison of the Ca and Ti secondary ion intensity obtained from BZO#1 single crystal with those obtained from BZO#2 and BZO#3 single crystals indicated that the Ca and Ti concentrations are at a prominent level, inversely to Sr concentration. The prominence of Sr, Ca, Ti and Hf impurity elements observed by GDMS is thus confirmed by SIMS analysis.

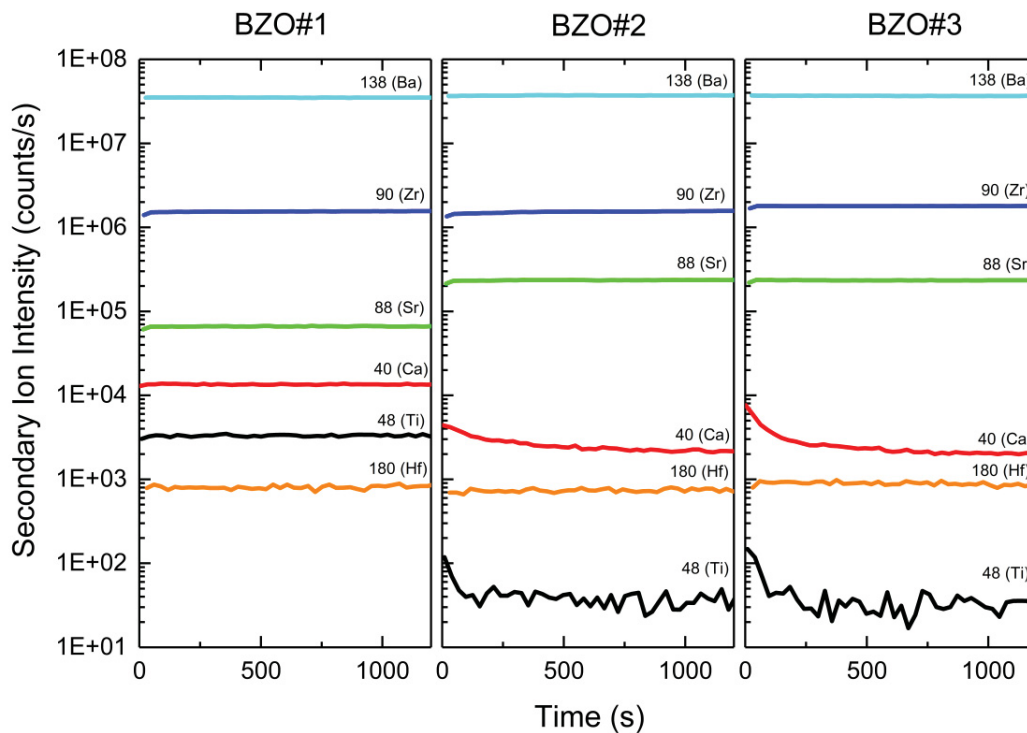


Fig. 6.8: SIMS depth profile (raw data) analysis of all samples.

The GDMS and SIMS measurements can be combined in order to estimate the absolute concentrations of the main impurities in BZO#2 and BZO#3 samples. Under the

assumption that the concentration of the main elements Ba, Zr and O is identical between all samples (identical matrices for the three samples studied), the secondary ion intensity for impurities scales linearly with concentration. Therefore, we can use the GDMS/SIMS measurements on BZO#1 as a calibration probe to determine the concentrations in BZO#2 and BZO#3. Hence, we determined the concentrations for the main impurities (Hf, Sr, Ca and Ti) by rescaling their SIMS intensity with respect to the Zr intensity. The results are reported in Table 6.4.

Table 6.4: Summary of the main impurity contents (ppm at.) for the three single crystals by combining GDMS and SIMS measurements.

Sample	Hf	Sr	Ca	Ti
BZO#1	3001	1420	179	370
BZO#2	2791	5157	32	4
BZO#3	2937	4426	28	3

---

## 6.3 Physical Properties

---



---

### 6.3.1 Optical Properties

---

Fig. 6.9 shows the transmittance of the three samples BZO#1, #2 and #3. BaZrO<sub>3</sub> single crystals are essentially transparent in the visible and NIR regions and exhibit a sharp absorption edge in the near-UV. BZO#2 is remarkably different from the other crystals. It exhibits a strong absorption band in the lower part of the visible spectrum, with a main peak around 800 nm, which is consistent with the blueish color of the crystal (see photo Fig. 6.7 (e)). This blueish color and the absorption band can likely be attributed to differences in oxygen stoichiometry, as previously shown previously for example on La<sub>0.5</sub>Na<sub>0.5</sub>TiO<sub>3</sub> [206]. The absorption edges are significantly different for the three crystals. BZO#1 grown by the floating zone technique, exhibits the sharpest and highest edge, while

the BZO#2 and BZO#3 grown by the tri-arc method show edges which are shifted to lower energies and are significantly smoother.

BaZrO<sub>3</sub> is expected to have an indirect gap according to most electronic structure calculations reported in the literature [207-210], with a conduction band minimum at the  $\Gamma$  point (0,0,0) and a valence band maximum at the R point ( $\frac{1}{2}, \frac{1}{2}, \frac{1}{2}$ ), where the phonon energies can be as high as 100 meV [186, 211]. These computations also suggest a relatively flat valence band, with a local maximum at  $\Gamma$  only 250 meV lower than the absolute maximum, where direct transitions would be allowed. One study even reports a direct band gap at  $\Gamma$  [212].

Experimentally, the nature and the value of the band gap can in principle be determined by the Tauc plot, i.e. plotting  $(\alpha \cdot hv)^{1/r}$  as the function of the energy  $hv$ , where  $\alpha$  is the absorption coefficient and  $r$  equals  $\frac{1}{2}$  or 2 for, respectively, a direct or indirect gap. The absorption can be determined from the transmittance  $T$ , reflectivity  $R$ , and thickness  $d$  of the samples using the relation  $T \approx (1-R)^2 \exp(-\alpha d)$  [162]. We neglect reflectivity in the following. The absorption edge is expected to exhibit a linear regime for  $r=1/2$  or  $r=2$ , depending on the character of the gap. Fig. 6.9 (b) and (c) show the Tauc plots for the three crystals, whereby the blueish BZO#2 appears very different from the two others. Colorless BZO#1 and BZO#3 exhibit a linear region in both plots, and extrapolations of this linear region gives gap values that are very similar for the two samples: 4.89/4.86 eV for  $r=2$  (hypothesis of the direct gap) and 4.76/4.74 eV for  $r=1/2$  (hypothesis of the indirect band gap) for BZO#1/#3 respectively. In addition, these both crystals show a pronounced Urbach tail linked to near-edge defects states. In BZO#2, this appears so dominant that no linear region can be identified.

In the present work, the value of  $\sim 4.8$  eV matches the 4.1-4.8 eV reported in a study dealing with BaZrO<sub>3</sub> powders prepared with various degrees of disorder [209], and the 5.0 eV found on a similar study with powder prepared by solid state reactions [213]. On the other hand, it is much higher than that the 3.8 eV reported [214] in a study of the BZT solid

solution, where the powders were obtained by the sol-gel route. As commonly observed, many computations underestimate the band gap value (3.2 eV in Refs. [196, 208, 210]).

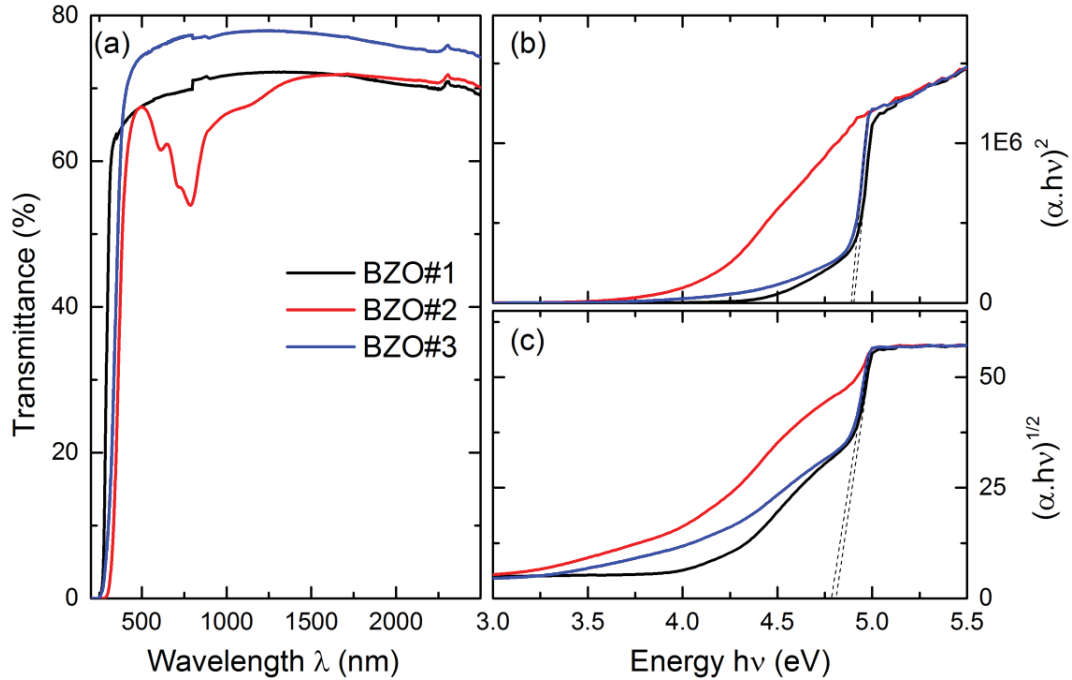


Fig. 6.9: (a) Optical transmission spectra of BaZrO<sub>3</sub> single crystal of BZO#1, BZO# 2, BZO#3 in a wide wavelength range. (b) and (c) Tauc plots with  $r=2$  (top right) and  $1/2$  (bottom right).

### 6.3.2 Dielectric Properties

Fig. 6.10 shows the experimental determination of the real part of the dielectric response and dielectric loss, versus temperature for different frequencies.  $\epsilon'$  is almost frequency independent at all temperatures. The static dielectric constant reaches approximately 40 to 50, a value that is very close to the previous report for BaZrO<sub>3</sub> powder samples [186, 215]. The real part of the dielectric response of BaZrO<sub>3</sub> increases steadily as the temperature decreases from 300 K for any given frequency. Furthermore, our measurements show the existence of two loss anomalies in all samples, namely a peak in  $\tan \delta$  around 50 K and a continuously increasing  $\tan \delta$  when decreasing temperature below around 25 K. These two

anomalies are correlated with the humps seen in  $\epsilon'$  since they occur at similar temperature and since they behave in a similar trend. For instance, both peaks in  $\tan \delta$ , occurring around 25 K and 50 K at low frequency, shift to higher temperature when increasing the frequency. The existence of such behavior has been reported already by Akbarzadeh *et al.* [186]. According to the report of Akbarzadeh *et al.*, we believe that the dielectric responses occurring at temperature around 25 K, is due to the activation of the oxygen octahedral rotation in BaZrO<sub>3</sub>. Regarding the second dielectric anomaly around 50 K, it seems realistic that a frequency-dependent peak has already been reported for  $\tan \delta$  in several other perovskite systems, such as KTaO<sub>3</sub>: Nb [216, 217], KTaO<sub>3</sub>: Fe, SrTiO<sub>3</sub>: Ca, KTaO<sub>3</sub>: Mn [218] near a similar temperature. Moreover, the chemical analysis shows that four major impurities were found in the crystals. In such case, these peaks should become more exacerbated when doping the sample with impurities. However, additional anomalies were observed in BZO#1 and BZO#3 around 125 K and 170 K without clear reasons of their presence.

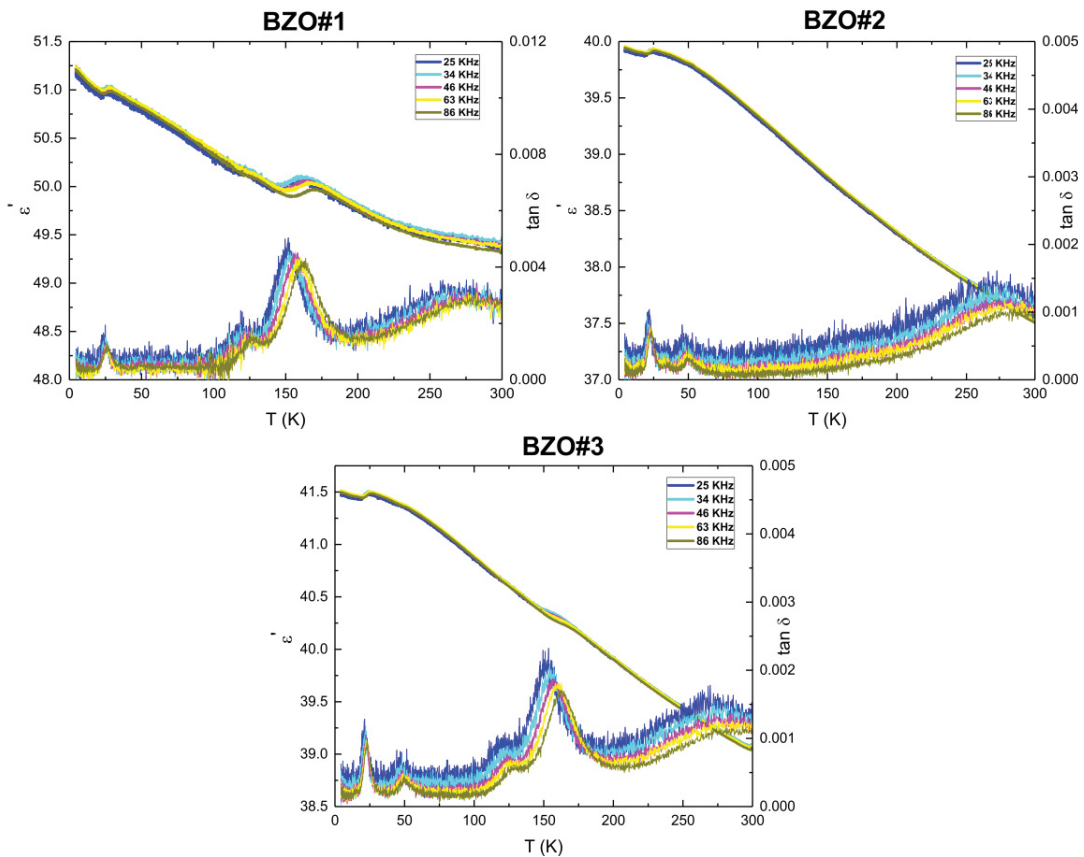


Fig. 6.10: Frequency dependence of real part of dielectric constant and dielectric loss for BZO#1, BZO#2 and BZO#3 samples at different temperatures.

### 6.3.3 Raman Spectroscopy Analysis

As BaZrO<sub>3</sub> is cubic with the space group  $Pm\bar{3}m$  which has no first-order Raman-active phonon mode. In spite of this, an intense Raman spectrum is usually observed [193, 194, 219], in a way that is reminiscent of other cubic perovskites (SrTiO<sub>3</sub> [220], KTaO<sub>3</sub> [221]). It is usually explained by second-order scattering processes involving combinations of two phonons.

Fig. 6.11 (a) shows the Raman spectra of BZO#1, BZO#2 and BZO#3 single crystals measured at ambient conditions in parallel scattering geometry. The spectra present a comparable signature, which is similar to spectra reported in the literature [193-195]. However, the spectra features observed on our samples are much sharper and better defined, even compared to the single crystal spectrum reported in [209], which is an indication of the good quality of the crystals obtained with both growth methods.

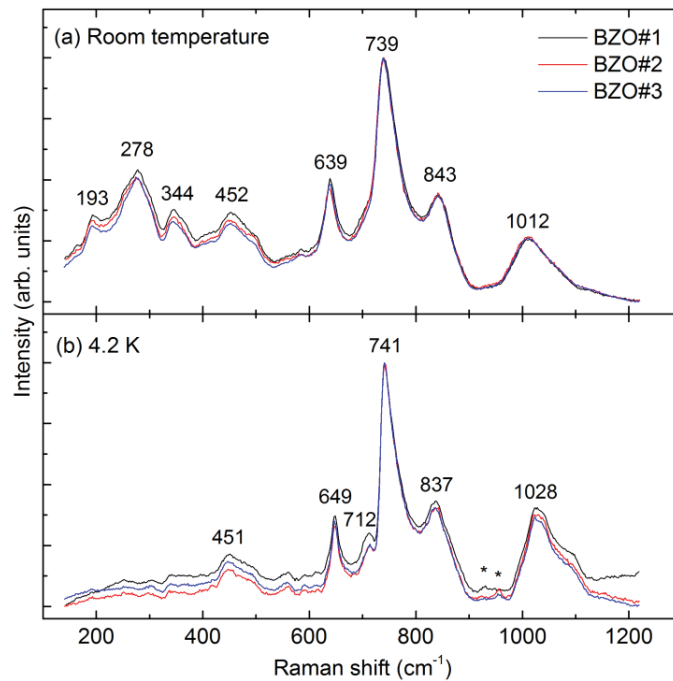


Fig. 6.11: Raman scattering spectra of BaZrO<sub>3</sub> single crystals at (a) ambient temperatures and (b) at 4.2 K. The positions of the main peaks are indicated. The stars mark the weak lines emerging at low temperatures and discussed in the text.

Raman spectra were collected upon cooling down to 4.2 K (Fig. 6.11 (b)). The similarity of the low-temperature and room-temperature spectra confirm the absence of any structural phase transition in the investigated temperature range. Slight changes, such as a subtle sharpening of the bands, and very small shifts in their positions are attributed to thermal expansion. The emergence of a couple of very weak and thin peaks can be noticed, but have to be attributed to extrinsic effects and defects. This is demonstrated by the observation that they are found at different positions in BZO#1 of the present work and in the commercial BZO#2 and BZO#3 samples. Such spurious Raman lines are not uncommon in perovskites [222], but cannot be assigned conclusively here.

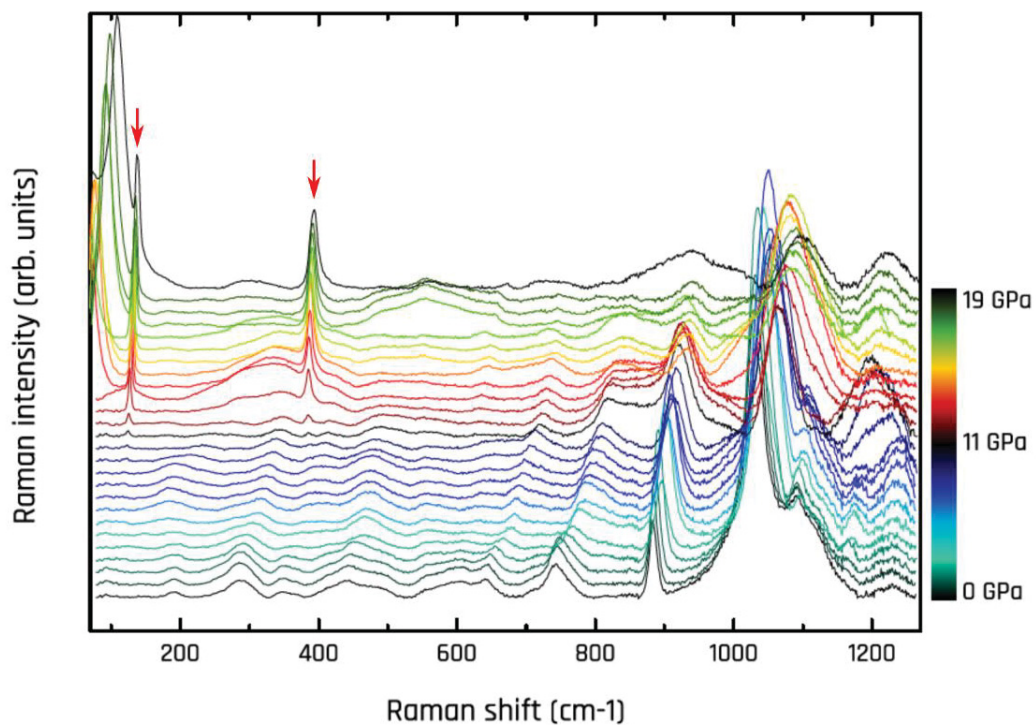


Fig. 6.12 Raman spectra of BZO#2 between 0 and 19 GPa.

Fig. 6.12 present a high-pressure effect on the Raman spectral for BZO#2 sample. The study was performed from ambient pressure up to 19 GPa with a step of about 0.7 GPa. It is obviously observed that a clear spectral change above 11 GPa and can be associated with a phase transition. This changes associated with cubic to tetragonal phase transition, which is in good agreement with what was reported in ceramic sample [194].

---

## 6.4 Conclusion

---

The growth of BaZrO<sub>3</sub> by flux method and optical floating zone technique are reported for the first time. The flux method using BaB<sub>2</sub>O<sub>4</sub> solvent enables to grow 150-200 μm-sized single crystals at half the melting point (1350 °C) of BaZrO<sub>3</sub>. Crystals size and quality are restricted by the formation of BaZr(BO<sub>3</sub>)<sub>3</sub>, which has been revealed by Raman spectroscopy and XRD diffraction. BaZrO<sub>3</sub> boules have been successfully grown by optical floating zone technique with single crystal sizes up to 6 mm long. They are transparent, colorless and have been shaped as millimeter-sized plate oriented along (100) direction. Four dominant impurities were observed through GDMS and SIMS analysis: Ca, Ti, Sr and Hf. Optical measurements performed on BaZrO<sub>3</sub> single crystal exhibit an optical band gap energy of ~4.8 eV, but we could not conclude on the direct or indirect character of the gap, where most calculations predict it to be indirect. Dielectric anomalies were observed both at low and high temperature, indicating that inherent intrinsic and extrinsic properties, respectively. Raman study revealed a second-order spectrum, with sharper features than in the spectra reported so far in the literature. This Raman spectrum does not change significantly down to the lowest temperature measured (4.2 K), which confirms the absence of phase transition. Furthermore, a high-pressure Raman spectrum indicates a phase transition from cubic to tetragonal at 11 GPa at room temperature. The availability of large single crystals opens the possibility for fundamental studies of BaZrO<sub>3</sub>, notably its dynamics at the macroscopic and local scales in perovskite BaTiO<sub>3</sub>-based systems.

# 7 Growth and Characterization of BCTZ Crystals

---

## 7.1 Crystal Growth of BCTZ Crystals

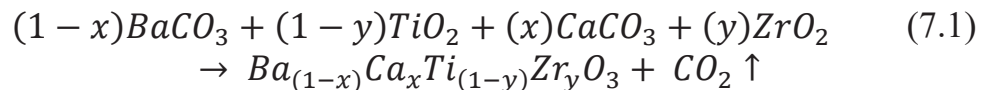
---

Over the last decade, lead-free piezoelectric ceramics of the BCTZ solid solution system were identified as a promising potential candidate to replace lead-containing piezoelectrics because of its high piezoelectric response of up to 620 pC.N<sup>-1</sup> for Ba(Zr<sub>0.2</sub>Ti<sub>0.8</sub>)O<sub>3</sub>-50(Ba<sub>0.7</sub>Ca<sub>0.3</sub>)TiO<sub>3</sub> (BZT-50BCT) compositions [12, 86]. Single crystals are expected to have even better electromechanical properties than ceramics and it has been proposed that BCTZ single crystals could exhibit a giant piezoelectric response around 1500-2000 pC.N<sup>-1</sup> as predicted by Liu *et al.* [12]. Based on previous works reported in literature [12, 83], we focus in this chapter on the growth and the characterization of BCTZ single crystals with various zirconium (Zr) and calcium (Ca) contents close to the BZT-50BCT composition, where high piezoelectric performances are expected.

### 7.1.1 Growth by Top-Seeded Solution Growth Technique

---

The starting materials were prepared from raw powders BaCO<sub>3</sub> (99.99%), CaCO<sub>3</sub> (99.99%), ZrO<sub>2</sub> (99.99%) and TiO<sub>2</sub> (99.99%) from Fox-Chemicals GmbH. The initial oxide compounds were weighed in the desired ratio, mixed and placed into an Ir crucible with 40 mm in diameter and 40 mm in height. The solid state reaction was performed by thermal treatment as described by Benabdallah *et al* [15] and Prakasam *et al.* [75]. The solid-state reaction process is described by the following equation:



Afterward, the calcined resulting powder [75] was analyzed through XRD experiment in order to determine the phase purity and crystallographic structure, as shown in Fig. 7.1. It is observed that all the calcined powders exhibit single perovskite phase without secondary phase and they are well crystallized.

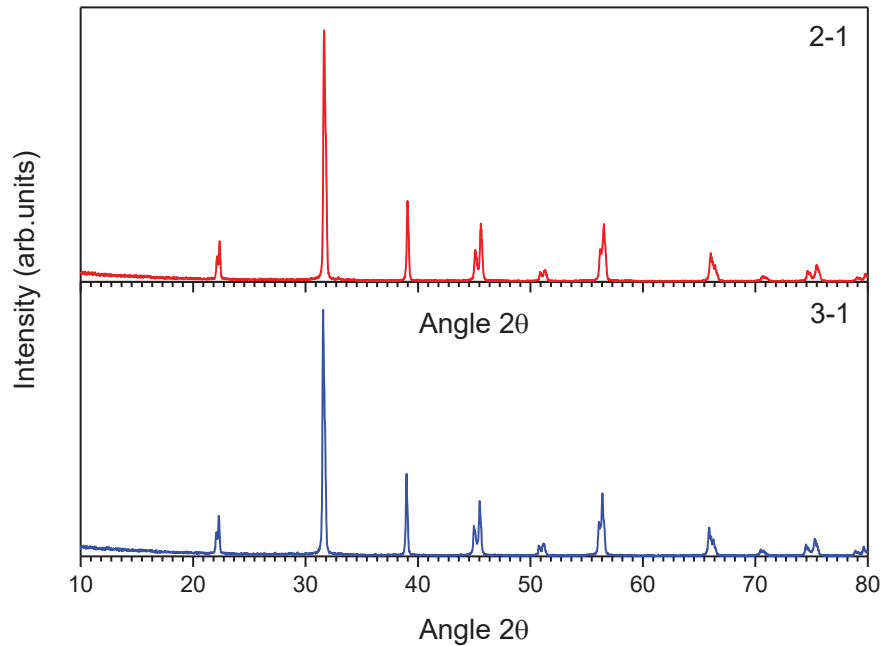


Fig. 7.1 XRD patterns of some BCTZ calcined powders 2-1 and 3-1.

Seven growth attempts of BCTZ crystals with different compositions were carried out with a self-flux method using the Top-Seeded Solution Growth (TSSG) technique. In some cases, after a first growth run, the load was re-used once or twice for further growths without reloading the crucible. As mentioned previously, Cyberstar Oxypuller induction furnace was used for the growth attempts. Growth atmosphere was Argon. Since no suitable seed with BCTZ composition was available, an iridium rod with 3 mm in diameter was used as a cold thermal point to initiate the nucleation and the growth of crystals, except for BCTZ No.1 where a  $\text{BaTiO}_3$  single crystal seed was used. Once the solution became homogeneous, the Ir rod was dipped into the solution for 24 hours above the saturation temperature. The solution was then cooled slowly with a cooling rate between 0.5 and 1.5

$^{\circ}\text{C}\cdot\text{h}^{-1}$ . The crystal started to grow in the supersaturated solution while the temperature decreased steadily. A rotation speed in between 5 rpm and 10 rpm and a pulling rate in between 0.01 to 1.5  $\text{mm}\cdot\text{h}^{-1}$  were applied. The growing crystal mass was monitored during the whole process. At the end of the growth, the as-grown crystal was completely pulled out from the liquid solution, and set 5mm above the liquid surface to reduce the thermal stress during the cooling down to room temperature which was performed for 72 hours.

---

### 7.1.2 Initial Compositions and Crystals Growth Results

---

The initial concentration of starting liquid solutions are listed in Table 7.1. For comparison, those of the previous works of Benabdallah *et al.* [15] and Buse *et al.* [88] are also given. The initial load compositions are considered as the global solution composition, including those of both the solvent and the solute to be grown. Moreover, the sum of molar percentages of Ba and Ca cations is taken as 100% for the A site, and that of Ti and Zr cations is taken as 100% in B site.

Table 7.1 Initial concentrations of the global solution for each growth attempt.

Attempt number	Corresponding figure	Amount on A site (mol%)		Amount on B site (mol%)	
		Ba	Ca	Ti	Zr
1-1	a	77.34	22.66	97.91	2.09
1-2	b	X	X	X	X
1-3	c	X	X	X	X
2-1	d	88.67	11.33	98.66	1.34
2-2	e	X	X	X	X
3-1	f	92.46	7.54	98.66	1.34
3-2	g	X	X	X	X
Benabdallah <i>et al.</i> (BCTZ 1)	X	85.00	15.00	90.00	10.00

Benabdallah <i>et al.</i> (BCTZ 2)	X	77.00	23.00	98.00	2.00
Benabdallah <i>et al.</i> (BCTZ 3)	X	76.46	23.54	97.55	2.45
Buse <i>et al.</i> (BCTZ 4)	X	76.80	23.20	97.79	2.21

The nomenclature of the table 7.1 for each attempt is written ‘x-y’ where ‘x’ labels the composition of the solution used for the growth ‘x’, and ‘y’ enumerates the growth attempts performed from the ‘x’ solution. For instance, it means that for 1-1 to 1-3 attempts, the solution with first (x=1) composition was used 3 times (y=1 to 3) without refilling the crucible in between each run. Each new attempt (y=2 and 3) performed from the first solution (x=1) is carried out from the same solution (x=1) from which is subtracted the mass of the crystal grown in the previous attempt and the volatilization loss. This aimed at growing several crystals from the same first initial solution with various compositions since segregation of elements occurs during the growth.

For comparison with previous attempts from the first solution, the 2-1 attempt was prepared with half concentration of Ca cations in A site and a slightly decreased concentration of Zr cation in B site. The 3-1 and 3-2 attempts were slightly different compared to previous attempts (2-1 and 2-2). A decreased concentration of Ca cations in A site and same concentration of Zr cations in B site were prepared. We note that all growth attempts are targeted to be closed to  $\text{Ba}(\text{Zr}_{0.2}\text{Ti}_{0.8})\text{O}_3\text{-}50(\text{Ba}_{0.7}\text{Ca}_{0.3})\text{TiO}_3$  (BZT-50BCT) composition.

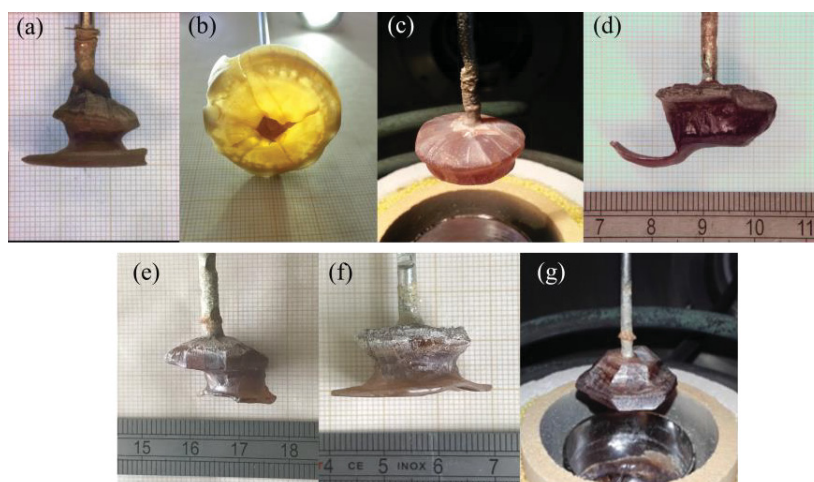


Fig. 7.2 Photographs of BCTZ boules grown on BaTiO<sub>3</sub> seed and Ir rod. (a) 1-1 boule obtained on an oriented (001)-BaTiO<sub>3</sub> seed, is covered by the solidified solution that crept along the rod. (b) 1-2 boule exhibiting radial cracks around the Ir rod and large clear region. (c) 1-3 boule clearly showing the creeping of solution along the Ir rod. (d) 2-1 centimeter-sized BCTZ polycrystalline boule exhibiting an expanded foot. (e) 2-2 centimeter-sized BCTZ polycrystalline boule exhibiting an extra-foot. (f) 3-1 centimeter-sized BCTZ polycrystalline boule. (g) 3-2 centimeter-sized single crystal boules exhibiting visible natural facets.

As shown in Fig. 7.2, 1-1 boule attempt was performed on (001)-oriented BaTiO<sub>3</sub> seed. Due to the 1<sup>st</sup> order hexagonal-cubic phase transition of BaTiO<sub>3</sub> around 1460°C [223] which occurs in the temperature range of BCTZ growth, the boule exhibits both mm-sized grains as well as large single crystal zones without defects. In order to replace unsuitable BaTiO<sub>3</sub> seed for BCTZ growth, CaTiO<sub>3</sub> may have been considered as a potential candidate as a seed for BCTZ growth, even if it displays a high temperature orthorhombic-tetragonal phase transition [224]. Indeed, crack-free CaTiO<sub>3</sub> single crystal can be grown directly from its liquid phase [110, 171]. An Ir rod was used as the nucleation site (1-2 to 3-2 attempts). Hence, large polycrystalline boules with millimeter-sized single crystals were produced by TSSG technique, except attempt 7-2 which led to a centimeter-sized single crystal in the bottom part. Almost all the BCTZ boules were observed with rough facets when viewed from the top of the boules. The polycrystalline boules exhibit polyhedral-like facets as shown in Fig.7.2 (g) and reflect the crystal habits in the thermal configuration of the furnace. Transparent and light-brownish single crystals without cracks were successfully extracted from the boules. Additionally, we note that the creeping of the solution all along the Ir rod or BaTiO<sub>3</sub> seed and a substantial volatilization of the flux (2-5% weigh loss of the crucible load) were both observed during the growth. These phenomena have been detrimental to the good control of the growth on the Ir rod or seed and affected directly the boules quality.

---

### 7.1.3 Distribution of Elements and Effective Segregation Coefficients

---

#### a) Effective segregation coefficients of elements

Generally speaking, the concentrations of the elements in crystallized boules strongly differ from those of the initial liquid solution from which the crystals are grown and highlight the elemental segregation in the BCTZ solid solution crystals [225, 226]. The segregation phenomenon is quantified by the ratio of the concentration of a given ion in the solid phase at the early beginning of the crystallization process (i.e. in the crystal on the iridium rod or seed, see table 7.2) with respect to that in the initial liquid solution (see table 7.1) [227]. This ratio  $k_{eff}$  is called the effective segregation coefficient and is described simply by Scheil's equation [228]:

$$k_{eff} \equiv \frac{C_s}{C_L} \quad (7.2)$$

where  $C_s$  is the element concentration in the solid phase that is formed at the very beginning of the growth, measured by EPMA, and  $C_L$  is the element concentration in the initial liquid solution.

Table 7.2 Element concentrations at the early beginning of the crystals.

Attempt number	Content in A site (mol%)		Content in B site (mol%)	
	Ba	Ca	Ti	Zr
1-1 (also Buse <i>et al.</i> BCTZ 5)	86.24	13.76	81.54	18.46
2-1 (also Buse <i>et al.</i> BCTZ 6)	92.79	7.21	80.69	19.31
3-1	96.26	3.74	77.45	22.55
Benabdallah <i>et al.</i> (BCTZ 1)	93.13	6.87	31.91	68.09
Benabdallah <i>et al.</i> (BCTZ 2)	85.65	14.35	79.77	20.23
Benabdallah <i>et al.</i> (BCTZ 3)	83.78	16.22	85.38	14.62
Buse <i>et al.</i> (BCTZ 4)	86.43	13.57	81.44	18.56

We point out that the initial liquid solution composition remains unknown for the second and third growth attempts ( $y=2$  and  $3$ ) for each solution ( $x=1$  to  $3$ ) because of the already as-grown crystal amount removed from solution (boules  $x-1$  with  $x=1$  to  $3$ ) and due to the unknown volatilized amount of the solution during the first growth attempt ( $y=1$ ). So that, only the first attempt can be considered for the calculation of the effective segregation coefficient. All segregation coefficients of individual element for the three solutions (1-1, 2-1 and 3-1) and those calculated from as-grown crystals of ICMCB which were grown during the previous works of Benabdallah *et al.*[15] and Buse *et al.*[229], are listed in Table 7.3. The segregation coefficients of each element rely on the relative contents of the elements in the perovskite site (A- or B-site).

Table 7.3 Effective segregation coefficients of individual element for different growth attempts.

Attempt number	$k_{\text{eff}}$ in A site		$k_{\text{eff}}$ in B site	
	Ba	Ca	Ti	Zr
1-1 (also Buse <i>et al.</i> BCTZ 5)	1.12	0.61	0.83	8.85
2-1 (also Buse <i>et al.</i> BCTZ 6)	1.05	0.64	0.82	14.41
3-1	1.04	0.50	0.79	16.83
Benabdallah <i>et al.</i> (BCTZ 1)	1.10	0.46	0.35	6.81
Benabdallah <i>et al.</i> (BCTZ 2)	1.11	0.62	0.81	10.12
Benabdallah <i>et al.</i> (BCTZ 3)	1.10	0.69	0.88	5.97
Buse <i>et al.</i> (BCTZ 4)	1.13	0.58	0.83	8.40

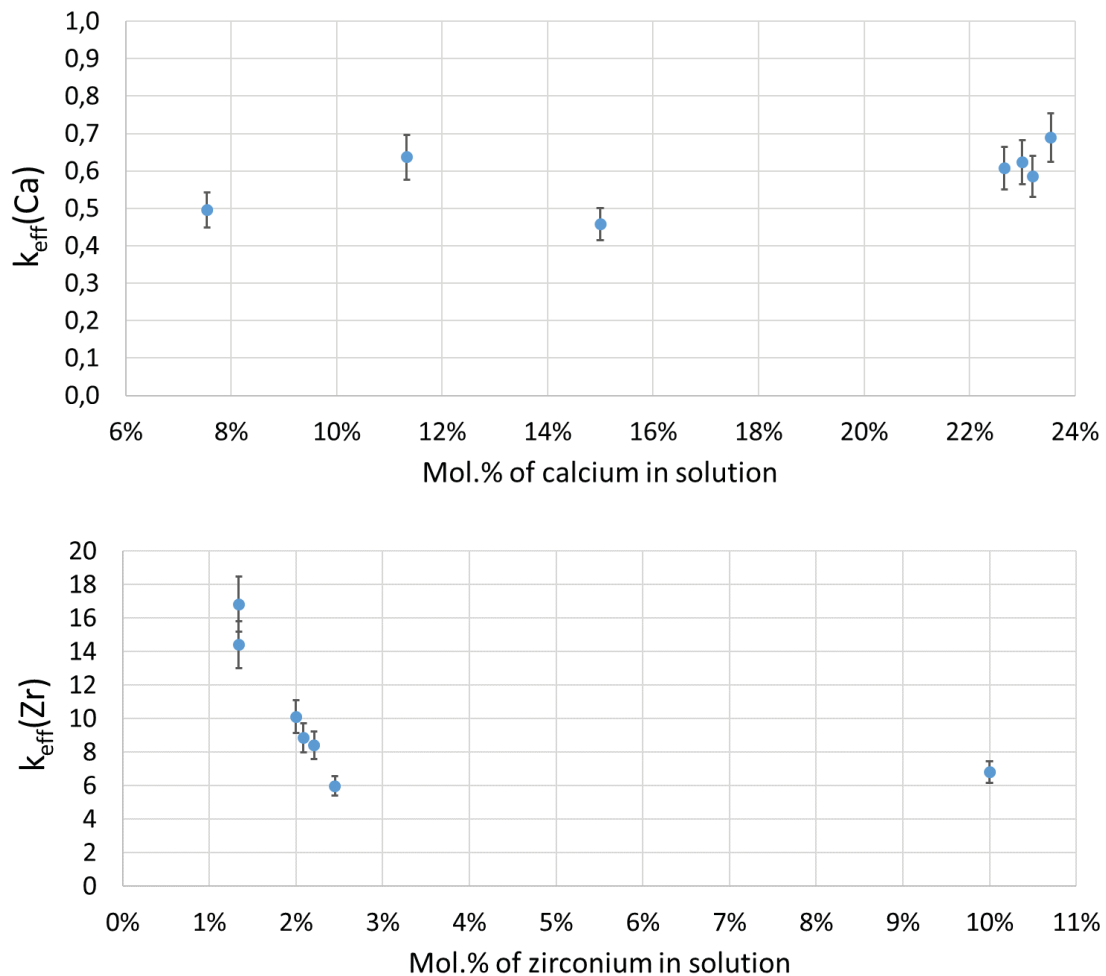


Fig. 7.3  $k_{\text{eff}}$  of Ca and Zr substitution element as a function of their concentration in the initial liquid solution analyzed by EPMA.

The segregation coefficient of Zr is significantly higher than 1. On the contrary,  $k_{\text{eff}}$  of Ca remains lower than 1. If  $k_{\text{eff}}$  of an element is lower than 1 as for Ca, the element is rejected by the growing crystal, which leads to a higher element concentration in the melt in front of the growth interface. On the other hand, the element with  $k_{\text{eff}}$  is higher than 1 as for Zr, the element is preferentially absorbed by the propagating solid-liquid interface, forming a depleted element boundary layer in front of the growth interface. While  $k_{\text{eff}}$  for Ca evolves steadily from 0.5 to 0.69 with its content in the liquid solution, that of Zr evolves significantly with its liquid content and reaches the outstanding values around 15 to 17 for

lower Zr content in the liquid (1.34%). This feature makes it difficult to obtain thereafter BCTZ samples with constant composition throughout their volume for reliable further electrical characterization. In the following, we present a more detailed study about quantitative analysis along transversal and longitudinal sections of the 2-1 boule where EPMA analysis allowed the measurement of the distribution of the Ca and Zr ion contents within the entire boule.

### b) Distribution of element contents in transversal section of as-grown boules

Fig. 7.4 (a), (b) and (c) show the locations of the EPMA analysis performed on the transversal section of the top of 2-1 boule. Four vertical analysis lines (X1 to X4) and four horizontal analysis lines (Y1 to Y4) for each crystal sample were performed with 150-300 $\mu\text{m}$  analysis step. The direction of four vertical scans along Y-axis were performed with fixed X position. On the contrary, the direction of four horizontal scans along X-axis were performed with fixed Y position.

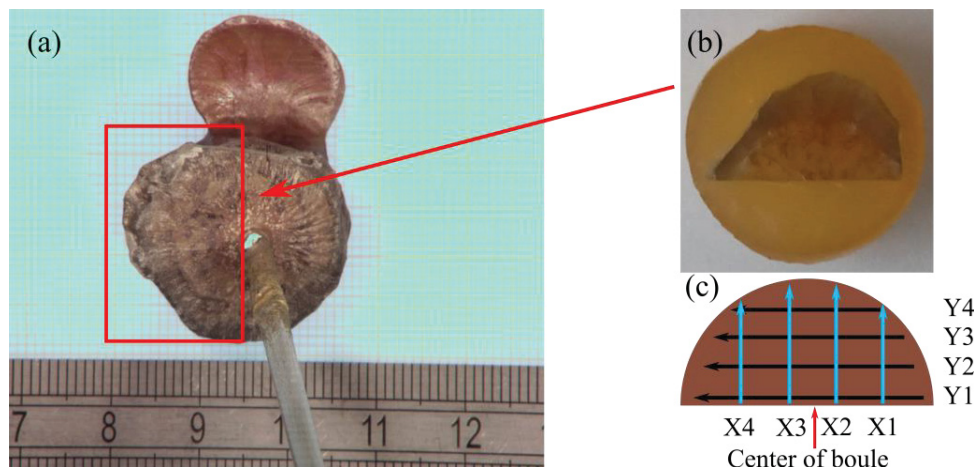


Fig. 7.4 (a) View from the top of the 2-1 BCTZ boule. (b) Photograph of the transversal section of the sample for EPMA analysis. (c) Schematic of four vertical lines and four horizontal lines for the study.

The distribution of Ca and Zr ion concentrations from the transversal section are plotted in Fig. 7.5. We note that the Ca concentrations increase from the center of boule to the periphery due to segregation  $k_{\text{eff}}(\text{Ca}) < 1$ . On the contrary, Zr concentrations show a reverse trend, because of the segregation coefficient  $k_{\text{eff}}(\text{Zr}) > 1$ . In addition, both Ca and Zr ion concentrations are nearly constant in the center of the boule for each scanning lines over a 6000-7000  $\mu\text{m}$  length of the sample.

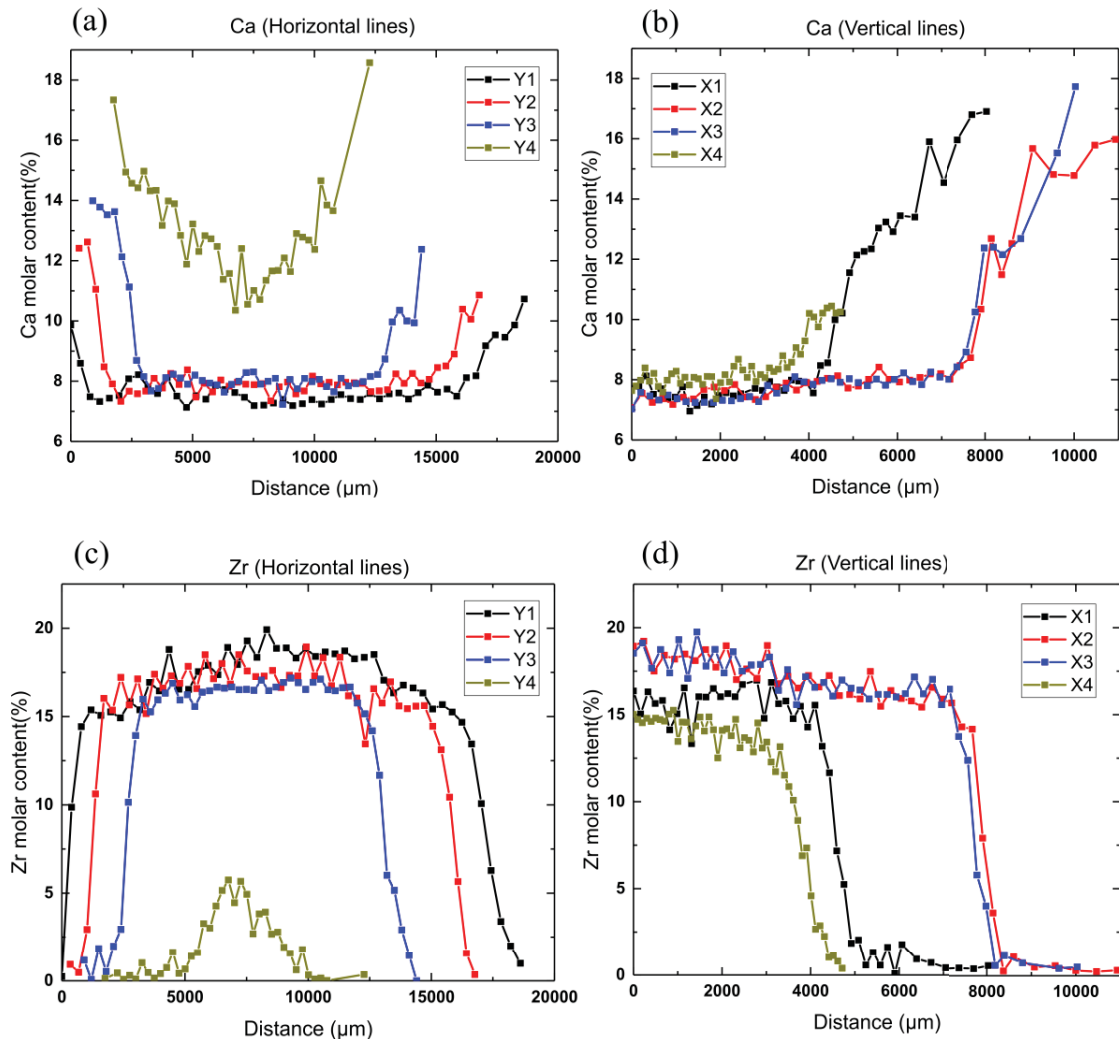


Fig. 7.5 The distribution of element concentrations in the transversal section of the top of the 3-1 BCTZ boule. (a) and (b) Ca element. (c) and (d) Zr element.

It is worth noticing that we observed at the extreme periphery of every boule a low Zr content over a 500-1000 $\mu\text{m}$  average thickness roughly. We attribute this feature to the

climbing (see Fig 7.2) of the solution and/or to the volatilized amount of the solution, which solidified above the already as-grown BCTZ boule. EPMA analysis highlighted that this solidified material presents a different composition than that of the liquid solution. Indeed, we observed that the BCTZ boules and Ir rod are always coated by a thin layer of BCT-like compound with a sudden concentration drop up to 18-25% for Ca and down to 1%-2% for Zr.

Concerning the volatilization origin of this material that solidified on the as-grown BCTZ boule, the deposited material is likely Ti-rich as it usually observed for pure BaTiO<sub>3</sub> flux growth with highly volatile TiO<sub>2</sub> flux [174, 230]. We also assumed that it is probably the same trend for Ca volatilization. On the other hand, concerning the origin of climbing of this material that solidified on the as-grown BCTZ boule, we note that the Ca concentration tends to be always up to 18-25%. This percentage values comes likely from the fact that there is an eutectic point in BaTiO<sub>3</sub>-CaTiO<sub>3</sub> (BCT) system (congruent composition) around 23% of CaTiO<sub>3</sub> [231, 232]. As we have a few amounts of Zr (around 1%-2%) in the solidified material on as-grown BCTZ boule, this eutectic point is slightly different than that in BCT system and is, thus, found to be around 18-25%.

### c) Distribution of element contents in longitudinal section of as-grown boules

A longitudinal section is analyzed and the evolution of Ca and Zr concentrations along the growth direction is characterized. The analysis parameters for longitudinal section are the same than those for the transversal section.

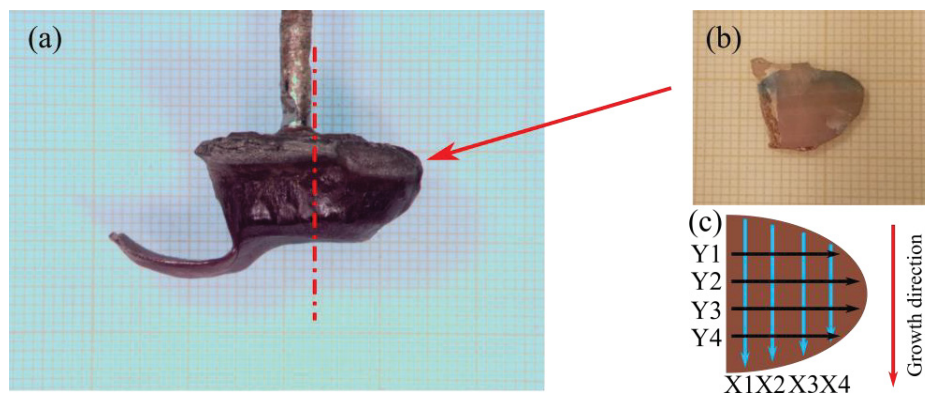


Fig. 7.6 (a) View from the side of the 2-1 boule. (b) Photograph of the sample for EPMA analysis. (c) Schematic of scanning lines for the study.

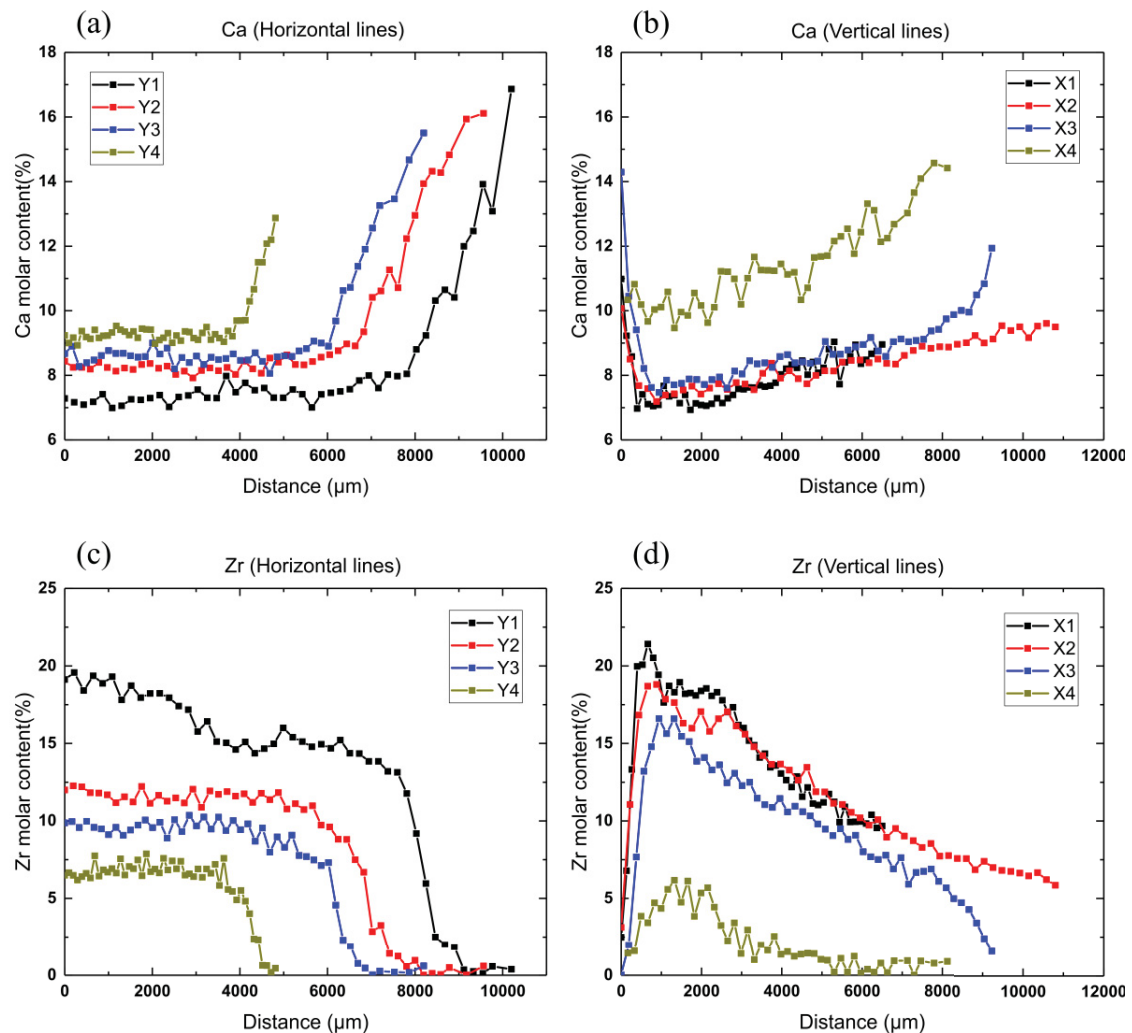


Fig. 7.7 The distribution of element concentrations in the longitudinal section of 2-1 BCTZ boule. (a) and (b) Ca element. (c) and (d) Zr element.

It can be observed in Fig. 7.7 that Ca and Zr concentrations increase and decrease with the growth direction, respectively. The element Ca is rejected by the growing crystal, which leads to a lower element concentration in the crystal. Additionally, the excess Ca diffuses away from the interface, leading to an increasing of its concentration within the crystal along the growth direction. On the other hand, due to the Zr segregation coefficient higher

than 1, Zr element is preferentially absorbed by the growing crystal, leading to a decreasing of the concentration within the crystal during the growth process. We note that the evolution of the distribution of elements within the crystals is more significant along the longitudinal section than in the transversal one. This is probably due to the fact of the pulling rate applied during the crystal growth. The speeds of crystallization being different from a longitudinal and transverse directions, this led thus to different element distribution of elements regarding the growth axis.

### 7.1.4 Periodical Fluctuations of Composition

Chemical analysis systematically reveals periodical fluctuations of the Zr content and, to a lower extent, of Ca content with amplitudes well beyond the accuracy limit (e.g. 0.3 mol.%) of the EPMA analysis (see Fig. 7.8). This phenomenon is reported by Buse *et al* [88].

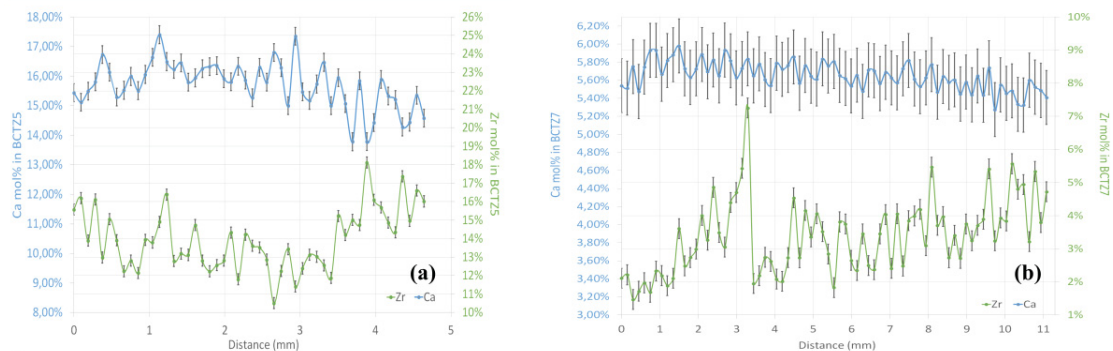


Fig. 7.8 Schematic of Ca and Zr element fluctuations measured by EPMA.

That suggests strongly the existence of two solid solutions with close compositions as already observed in  $\text{BaZrO}_3\text{-CaZrO}_3$  and  $\text{BaTiO}_3\text{-CaTiO}_3$  systems from which the BCTZ solid solution derives, a miscibility gap allows for the coexistence of two solid solutions through a phase segregation mechanism. Investigated BCTZ compositions range exhibits the same trend where two Ca- and Zr-substituted  $\text{BaTiO}_3$  solid solutions are coexisting through a very likely spinodal decomposition at high temperature. Such a phenomenon has not been observed in BCTZ ceramics of same compositions because the synthesis time and

temperature (~15H and 1350°C) are drastically lower to those (~ up to 2 weeks and 1570 °C) of single crystal growths and prevent then the ceramics from phase separation. As the BCTZ compositional disorder implies Ca and Zr low amplitude concentrations fluctuations through the boules, the system becomes unstable at high temperature and finally decomposes. Hence, the spinodal demixion is favored by the resulting continuous annealing of the already-as-grown crystal during the whole growth process. This out of equilibrium process leads to pseudo-periodic distribution of the precipitated phases when interrupted before end. This is similar in some respect to Ostwald ripening of precipitate particles but with uphill diffusion since the diffusion takes place against the concentration gradient.

---

## 7.2 Dielectric and Electromechanical Properties

---

Seven crystals with Ca and Zr compositions approaching the desired  $(1-x)\text{Ba}(\text{Zr}_{0.2}\text{Ti}_{0.8})\text{O}_3-x(\text{Ba}_{0.7}\text{Ca}_{0.3})\text{TiO}_3$  (red line in Fig. 7.9) have been selected for dielectric and electromechanical characterization. The crystals were extracted from within the boules along suitable directions chosen so as to minimize the chemical inhomogeneities due to the segregation described in previous section. The final crystals are mm-sized, and have a relative composition accuracy about  $\pm 1.5$  mol.% for Zr and  $\pm 0.5$  mol.% for Ca. Their average compositions are shown in Table 7.4 and Fig. 7.9.

Table 7.4 Selected crystals with average element concentrations.

Crystal number	Chemical formula	Ca (mol.%)	Zr (mol.%)
#1	$(\text{Ba}_{0.784}\text{Ca}_{0.216})(\text{Ti}_{0.966}\text{Zr}_{0.034})\text{O}_3$	21.6	3.4
#2	$(\text{Ba}_{0.805}\text{Ca}_{0.195})(\text{Ti}_{0.948}\text{Zr}_{0.052})\text{O}_3$	19.5	5.2
#3	$(\text{Ba}_{0.806}\text{Ca}_{0.194})(\text{Ti}_{0.885}\text{Zr}_{0.115})\text{O}_3$	19.4	11.5
#4	$(\text{Ba}_{0.776}\text{Ca}_{0.224})(\text{Ti}_{0.911}\text{Zr}_{0.089})\text{O}_3$	22.4	8.9
#5	$(\text{Ba}_{0.815}\text{Ca}_{0.185})(\text{Ti}_{0.906}\text{Zr}_{0.094})\text{O}_3$	18.5	9.4
#6	$(\text{Ba}_{0.826}\text{Ca}_{0.174})(\text{Ti}_{0.843}\text{Zr}_{0.157})\text{O}_3$	17.4	15.7
#7	$(\text{Ba}_{0.772}\text{Ca}_{0.228})(\text{Ti}_{0.965}\text{Zr}_{0.035})\text{O}_3$	22.8	3.5

---

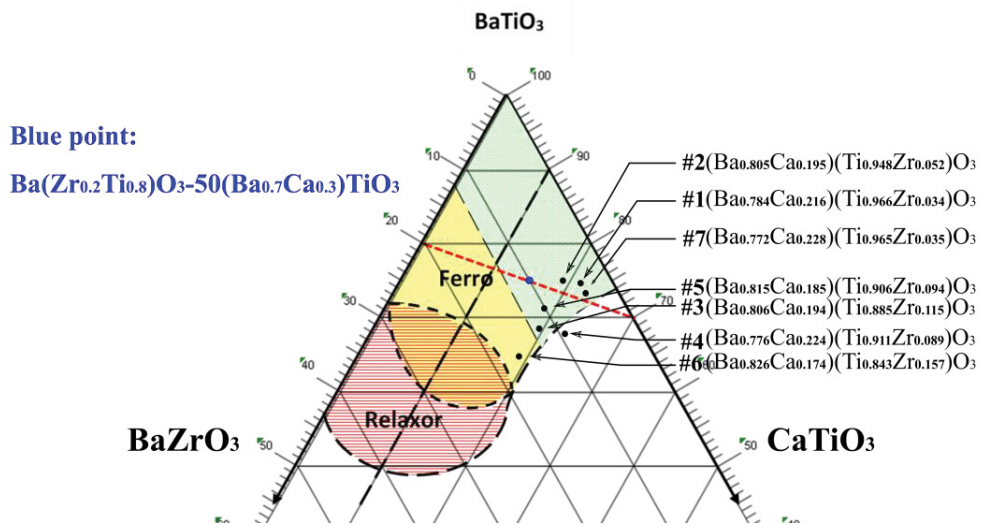


Fig. 7.9 Pseudo-ternary phase diagram of  $\text{BaTiO}_3\text{-CaTiO}_3\text{-BaZrO}_3$ .

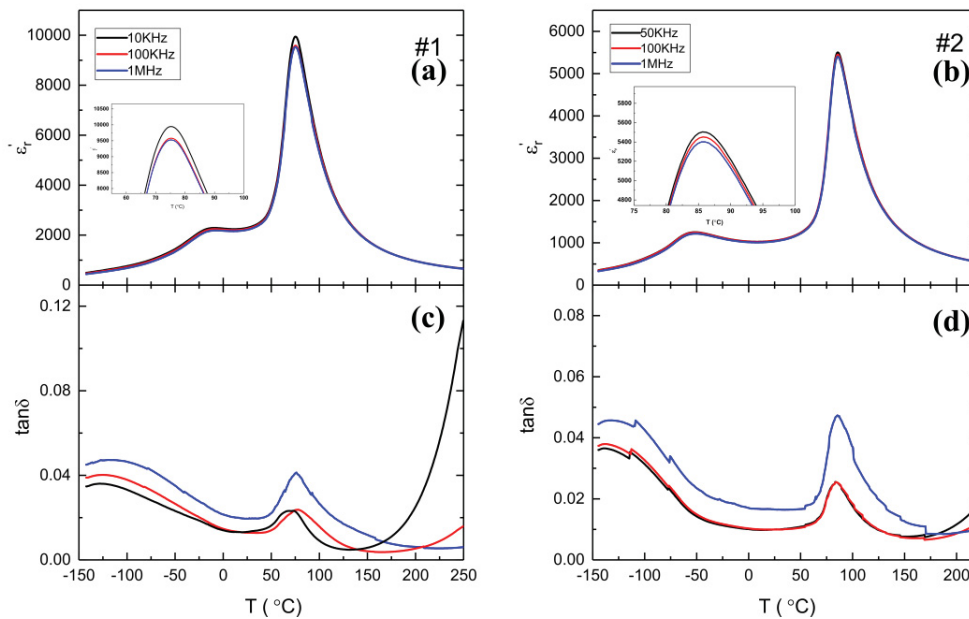


Fig. 7.10 (a) and (c) temperature-dependent dielectric permittivity and losses for #1 sample. (b) and (d) for #2 crystal.

The temperature-dependent dielectric permittivity and losses for the #1 sample at various frequencies, is shown in Fig. 7.10 (a) and (c). Two anomalies are observed, and we note that no shift of dielectric peaks under the three different frequencies is observed, indicating

that the #1 sample is a normal ferroelectric material regarding previous investigations performed on (1-x)BZT-xBCT ceramics and crystals [12, 86, 233, 234]. The anomaly at the highest temperature is identified as the Curie temperature ( $T_c$ ), corresponding to the cubic-tetragonal phase transition (C-T). It is relatively sharp and the value of  $T_c$  is not dependent on the frequency. The other one at lower temperature denotes the tetragonal to orthorhombic phase transition (T-O). For #2 sample, the small and large peaks in Fig. 7.10 (b) reveal similar behavior like the two peaks in Fig. 7.10 (a), due to the almost same amount of Ca and Zr concentrations.

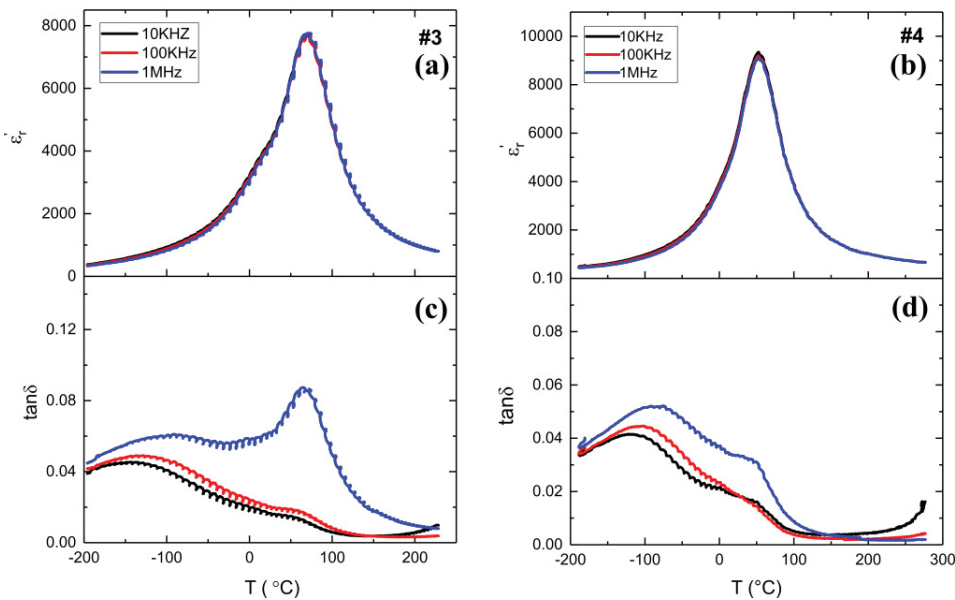


Fig. 7.11 (a) and (c) temperature-dependent dielectric permittivity and losses for #3 sample. (b) and (d) for #4 crystal.

Fig. 7.11 (a) and (c) reveal temperature-dependent dielectric permittivity and losses for the #3 sample, respectively. A peak can be observed in the temperature range from -196  $^{\circ}\text{C}$  to 200  $^{\circ}\text{C}$ . There is no obvious shift of dielectric peaks under the three different frequencies, indicating the #3 sample is a normal ferroelectric material with no relaxation. In this case, it is characteristic of the paraelectric phase to ferroelectric phase transition. The dielectric permittivity and dielectric losses of the #4 sample are observed in Fig. 7.11 (b) and (d). The peak reveals similar behavior with the #3 sample.

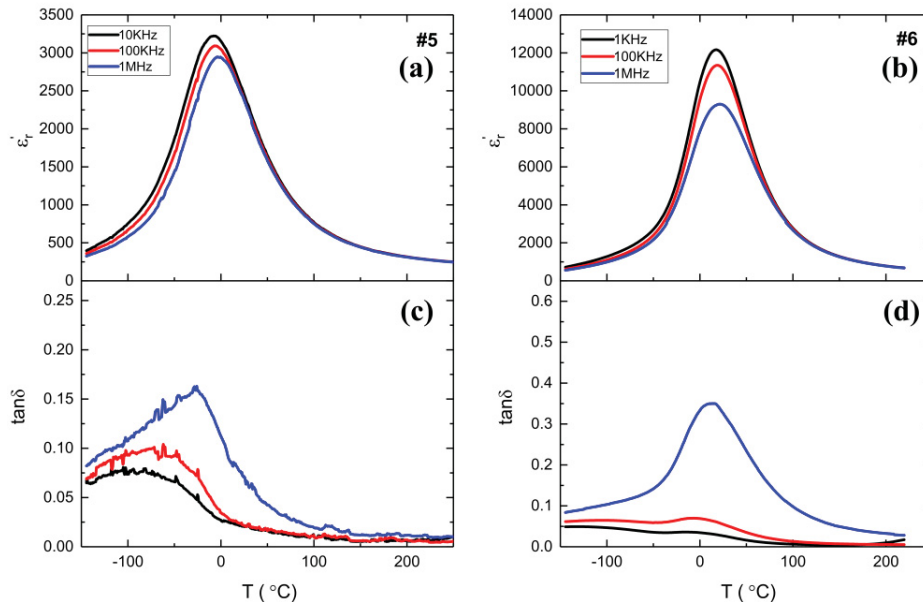


Fig. 7.12 (a) and (c) temperature-dependent dielectric permittivity and losses for #5 sample. (b) and (d) for #6 crystal.

Fig. 7.12 (a) and (c) present the temperature-dependent dielectric permittivity and dielectric losses of the #5 sample. It is observed in Fig. 7.12 (a) that there is one very broad peak occurring at  $T_{\max}$  ( $T_{\max}$  is the temperature of the peak of the relative real permittivity  $\epsilon'_r$  vs. temperature) with frequency dispersion for temperature ( $T < T_{\max}$ ) and a shift of  $T_{\max}$  with a frequency. This behavior was also reported [18, 76, 82, 83] in both BCTZ ceramics and crystals with larger amount of Zr ions. The value of  $T_{\max}$  is dependent on the frequency unlike that of the Curie temperature ( $T_c$ ). In addition, there is an increasing in  $T_{\max}$  when frequency increases. This behavior is of relaxor type. Moreover, with decreasing temperature, the frequency dispersion decreases in comparison with a frequency observed at a temperature close to  $T_{\max}$ . The dielectric loss significantly increases, when the frequency is increasing. Fig. 7.12 (b) show similar behavior of  $\epsilon'_r$  for the #6 sample similarly to the peak in Fig. 7.12 (a). There is a relatively sharp peak of  $\epsilon'_r$  at  $T_{\max}$ . In addition, there is an increasing in  $T_{\max}$  when frequency increases. Again, this signals a relaxor behavior.

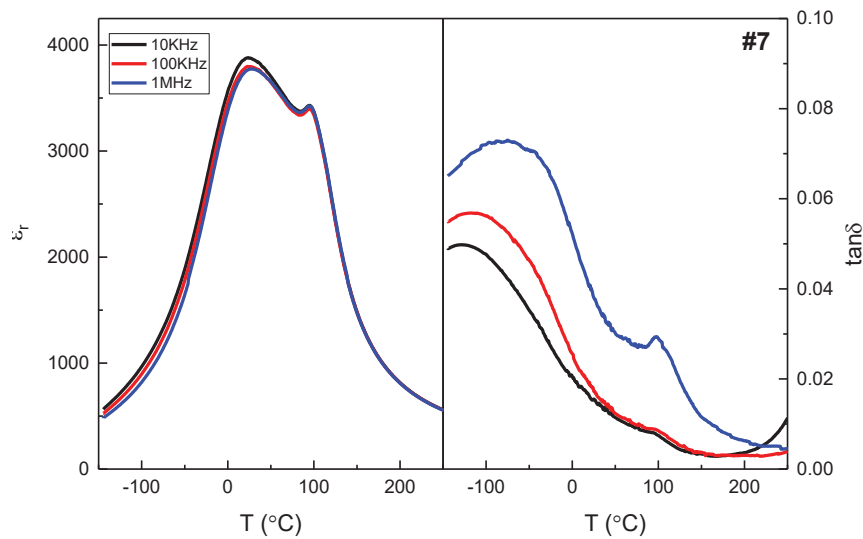


Fig. 7.13 Temperature-dependent dielectric permittivity and dielectric loss of #7 sample.

As shown in Fig. 7.13, crystal #7 has two sharp peaks in its dielectric constant and  $T_c$  is not dependent on the frequency. More interestingly, an abnormal behavior is observed, where the value of  $T_{max}$  is higher than  $T_c$ . There is no clear reason why the experimental observations show an abnormal peak.

Due to relaxor properties and cracks inside some of the crystals, electromechanical properties of samples #1, #2 and #7 only were investigated. The ferroelectric hysteresis loop of #1, #2 and #7 samples at room temperature are presented in Fig. 7.14. For sample #1, the remanent polarization is approximately  $10.7 \mu\text{C}\cdot\text{cm}^{-2}$  and the coercive field is  $0.7 \text{ kV}\cdot\text{mm}^{-1}$ . Sample #2 has a remanent polarization approximately around  $8.7 \mu\text{C}\cdot\text{cm}^{-2}$  which is smaller than #1. The coercive field of #2 is  $0.8 \text{ kV}\cdot\text{mm}^{-1}$ . For sample #7, the coercive field is  $0.49 \text{ kV}\cdot\text{mm}^{-1}$ . It has a remanent polarization approximately around  $3.3 \mu\text{C}\cdot\text{cm}^{-2}$ . Moreover, the piezoelectric coefficient  $d_{33}$  was measured by the Berlincourt method after being poled at  $2 \text{ kV}\cdot\text{mm}^{-1}$ . They are  $191 \text{ pC}\cdot\text{N}^{-1}$  for sample #1,  $185 \text{ pC}\cdot\text{N}^{-1}$  for sample #2 and  $20 \text{ pC}\cdot\text{N}^{-1}$  for sample #7. These are smaller values than that expected and mentioned by Liu *et al* for ceramics [12].

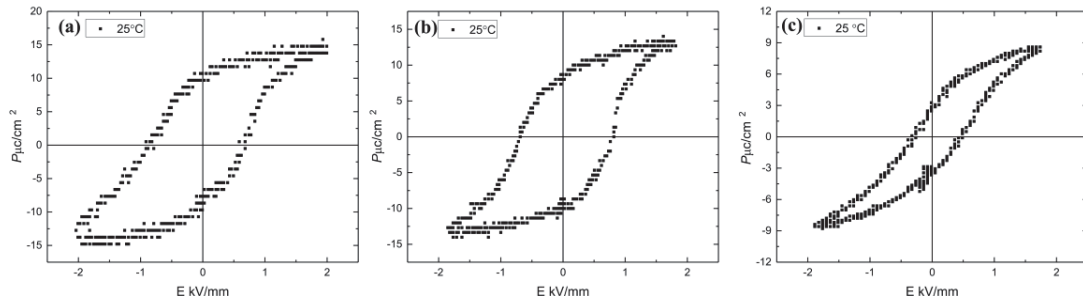


Fig. 7.14 Room temperature FE hysteresis loops at  $f=10\text{Hz}$  for (a) #1 sample, (b) #2 sample and (c) #7 sample.

---

### 7.3 Double Hysteresis Loop in BCTZ Crystal

---

Fig. 7.15 shows the plots of polarization  $P$  vs. electrical field  $E$  at high temperature for  $(\text{Ba}_{0.776}\text{Ca}_{0.224})(\text{Ti}_{0.911}\text{Zr}_{0.089})\text{O}_3$  sample. The PE loop reveals a double hysteresis loop which suggests the possibility of a field-induced phase transition. Additionally, when the temperature increases, the hysteresis loop is not detected. This behavior (double hysteresis loop) have been observed in literature, such as in  $\text{BaTiO}_3$  [235-238],  $(\text{Ba,Sr})\text{TiO}_3$  [239],  $\text{BiFeO}_3$  [240] and other  $\text{PbZrO}_3$ -based perovskite [58]. Based on literature, there are several physical origins leading to double PE loops in perovskite structured materials [241]: i) an antiferroelectric behavior, whereby it is the signature of a field-induced phase transition from an antiferroelectric (non-polar) phase to a polar phase. ii) a pinching effect of the ferroelectric hysteresis loop due to polar defects in the material iii) a field induced transition from a paraelectric to a polar phase in a ferroelectric above  $T_c$ , as for  $\text{BaTiO}_3$  crystal. In this case, the PE relationship is unlike normal BCTZ ferroelectrics materials which were reported in literature [12, 83]. In order to understand whether this phenomenon is a typical antiferroelectric behavior or not, dielectric and high voltage hysteresis loop have been performed.

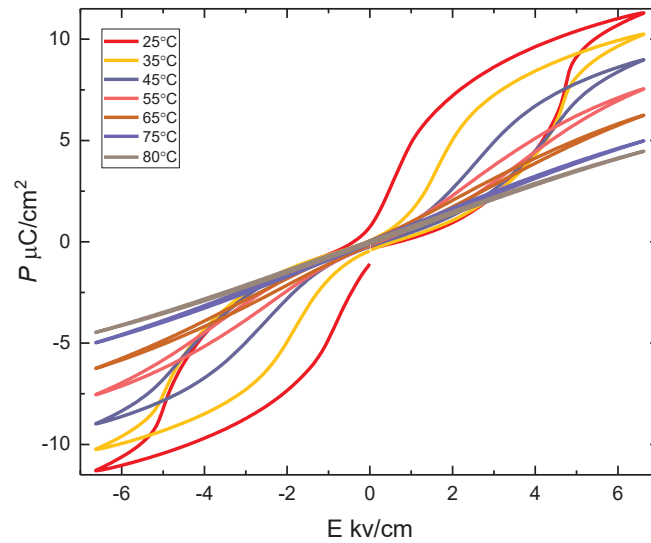


Fig. 7.15 The electrical field dependence of polarization at elevated temperature.

The temperature-dependent of the dielectric permittivity and losses of  $(\text{Ba}_{0.776}\text{Ca}_{0.224})(\text{Ti}_{0.911}\text{Zr}_{0.089})\text{O}_3$  sample is shown in Fig. 7.16. From the results, only one sharp peak can be observed, corresponding to the paraelectric to ferroelectric phase transition. In the meantime, the value of peak is not dependent on the frequency, what is classically attributed to a pure ferroelectric behavior.

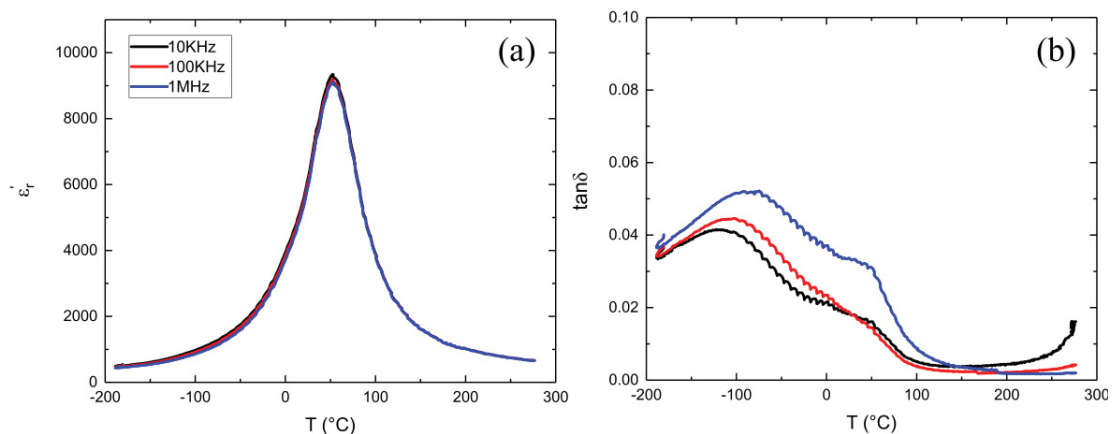


Fig. 7.16 Temperature-dependent of the dielectric permittivity (a) and losses (b) for this sample.

The  $(\text{Ba}_{0.776}\text{Ca}_{0.224})(\text{Ti}_{0.911}\text{Zr}_{0.089})\text{O}_3$  sample was poled in a silicone oil bath by high voltage to check further whether there is an aging effect. The poling electric field was selected  $2 \text{ kV}\cdot\text{mm}^{-1}$ . The temperature was hold at  $80 \text{ }^\circ\text{C}$  for 30 minutes, then a cooling (rate  $1 \text{ }^\circ\text{C}\cdot\text{min}^{-1}$ ) to room temperature. The PE hysteresis loop was then measured at room temperature, as shown in Fig. 7.17, with several maximum voltages, At the highest maximum voltage, we observe a hysteresis loop corresponding to the ferroelectric state. We conclude that, the double PE hysteresis loop in this BCTZ sample indicates neither an antiferroelectric behavior nor an electrical field induced paraelectric to ferroelectric phase transition near Curie temperature, but is an irreversible effect linked to the as-grown state of the crystal, and which disappears after poling.

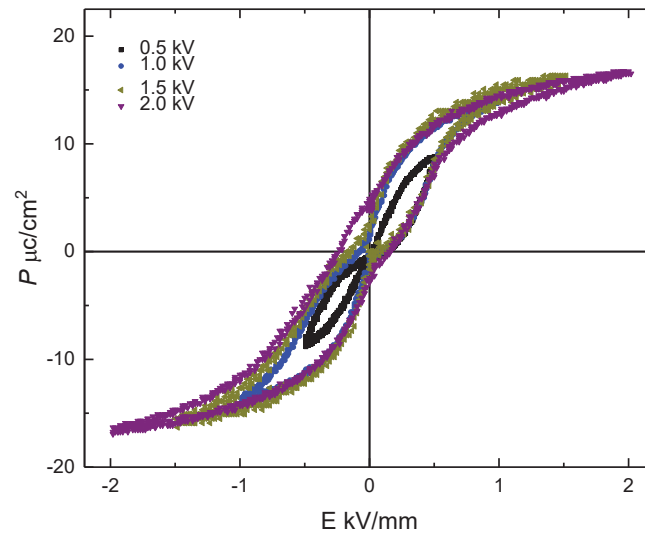


Fig. 7.17 Hysteresis loop for  $(\text{Ba}_{0.776}\text{Ca}_{0.224})(\text{Ti}_{0.911}\text{Zr}_{0.089})\text{O}_3$  sample at room temperature.

---

## 7.4 Optical Birefringence

---

Almost all of the previous studies in the BCTZ system reported in the literature were made on ceramics samples [12, 83, 86]. Hence, it is interesting to investigate the in-situ

temperature dependent optical birefringence on crystals. It can allow to probe structural phase changes, as birefringence is sensitive to changes of the crystalline system.

We performed optical birefringence measurement on a  $(\text{Ba}_{0.776}\text{Ca}_{0.224})(\text{Ti}_{0.911}\text{Zr}_{0.089})\text{O}_3$  sample for a temperature range from 25 °C to 150 °C. All the observations and measurements were carried out between crossed polarizers and 20 × objective lens. Some smaller bright spots due to dust particles could be observed on the sample surface. As described in the previous section, the Curie temperature of  $(\text{Ba}_{0.776}\text{Ca}_{0.224})(\text{Ti}_{0.911}\text{Zr}_{0.089})\text{O}_3$  sample is 52 °C , which corresponds to a phase transition from ferroelectric tetragonal phase to paraelectric cubic phase. The domains in this sample are expected to extinct above the Curie temperature. However, the whole crystal reveals bright and dark region at high temperature. This indicates that there is a lower cubic symmetry phase, as shown in Fig. 7.18 (c), (d), (g) and (h).

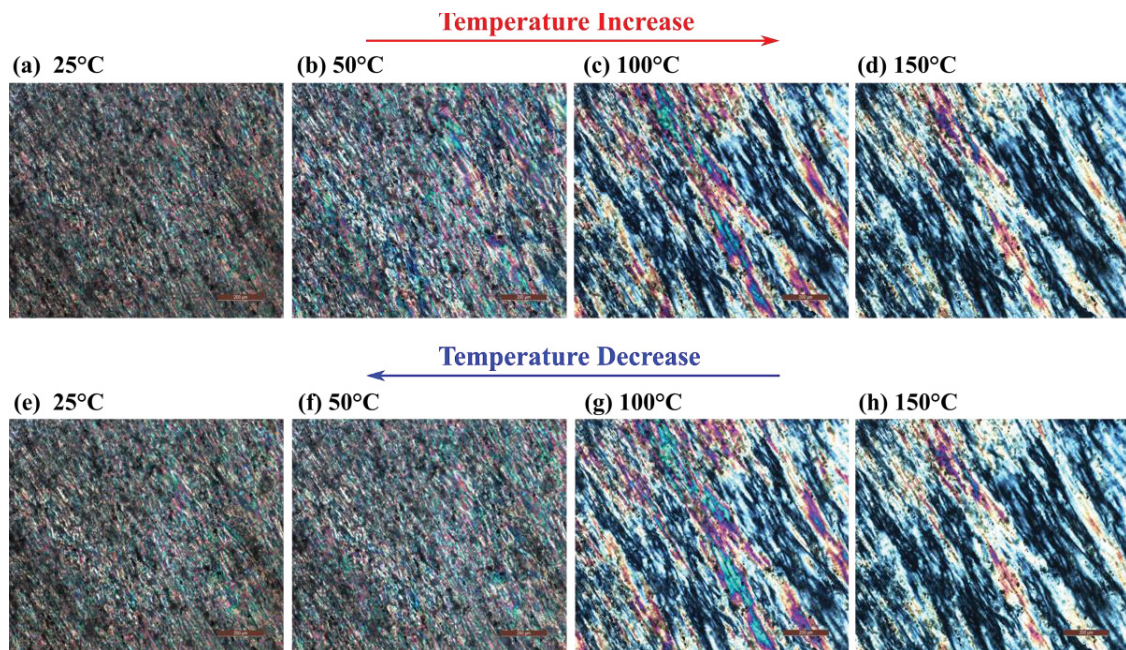


Fig. 7.18 In-situ observation of domain structure during the temperature cycling (scale bar: 200nm).

To summarize, the paraelectric phase to ferroelectric phase transition were not clearly observed in the optical birefringence. In particular, no clear emergence of ferroelectric domains could be observed in the condition of use this experiment, this is likely due to the inhomogeneity of the samples.

---

## 7.5 Conclusion

---

In this chapter, seven growth attempts of BCTZ crystals were carried out by the Top Seeded Solution Growth technique. The relationship between the initial liquid concentrations for both Ca and Zr elements and the effective segregation coefficients is discussed. The Ca and Zr concentrations respectively increase and decrease with the growth direction and the radius of the boules. It is also found that Zr cations are preferentially absorbed by the crystal during the growth process featuring effective segregation coefficients higher than 1. Ca cations show an opposite behavior with effective segregation coefficients lower than 1. Moreover, a very likely spinodal decomposition phenomenon was also pointed out through periodical fluctuation of cations contents in the crystals that is well-beyond the EPMA accuracy limit. That suggests the coexistence of two solid solutions within the crystal with close compositions that may affect the piezoelectric performance of BCTZ crystals compared to that of ceramics. The investigation of dielectric properties, indicate that a relaxor behavior is present for certain BCTZ compositions with high Zr content. Nevertheless, most of BCTZ crystals exhibit a normal ferroelectric behavior for low Zr content with Curie temperature ranging from 53 °C to 95 °C and  $d_{33}$  up to 191 pC.N<sup>-1</sup> in the vicinity of the phase region. Due to these features, it remains an important challenge to produce centimeter-sized single crystals with optimal and steady compositions close to that of Ba(Zr<sub>0.2</sub>Ti<sub>0.8</sub>)O<sub>3</sub>-50(Ba<sub>0.7</sub>Ca<sub>0.3</sub>)TiO<sub>3</sub> (BZT-50BCT). Interestingly, an abnormal double-like PE hysteresis loop was observed in (Ba<sub>0.776</sub>Ca<sub>0.224</sub>)(Ti<sub>0.911</sub>Zr<sub>0.089</sub>)O<sub>3</sub> sample, that was associated to an irreversible effect disappearing upon poling. The inhomogeneity of the crystals did not allow to investigate the phase transitions or domain structure by optical birefringence.

## 8 Conclusion and Prospects

---

In this work, we studied the growth of various single crystals grown in the BaTiO<sub>3</sub>-CaTiO<sub>3</sub>-BaZrO<sub>3</sub> pseudo-ternary system, with the general objective to contribute to a better understanding of the outstanding properties of BCTZ solid solution. First, we focused on the end members BaZrO<sub>3</sub> and CaTiO<sub>3</sub>. A particular attention was paid on BaZrO<sub>3</sub> and its intrinsic physical properties, whose influence on the piezoelectric response in BCTZ is poorly understood. Last, crystals of the Ba<sub>1-x</sub>Ca<sub>x</sub>Ti<sub>1-y</sub>Zr<sub>y</sub>O<sub>3</sub> solid solution (BCTZ) were studied with respect to their chemical composition through a broad and various Zr and Ca content range.

CaTiO<sub>3</sub> single crystals were grown by both the flux method and the optical floating zone technique. While the flux method yielded mm-sized crystals, in the case of optical floating zone furnace, centimeter-sized CaTiO<sub>3</sub> crystals were obtained from the melt at 1975 °C. Chemical analysis revealed Al, Mg and Ba as main impurities in the range of 0.01-0.02 at. %. Raman spectra of CaTiO<sub>3</sub> were recorded and were found in good agreement with spectra referenced in the literature.

The growth of BaZrO<sub>3</sub> crystals was the most challenging issue of this work due to its very high melting point around 2700 °C. We used two original techniques never reported so far in order to grow high-quality BaZrO<sub>3</sub> single crystals. On the one hand, BaB<sub>2</sub>O<sub>4</sub> flux was successfully used to produce 150-200 μm-sized BaZrO<sub>3</sub> crystals at half its melting point temperature. On the other hand, bulk centimeter-sized BaZrO<sub>3</sub> boules were grown from the melt by optical floating zone furnace at 2700 °C. The quality of the latter was compared to two commercial crystals grown by the tri-arc method. Sr, Hf, Ca and Ti were detected by both GDMS and SIMS as minor impurities in the range of 0.3-0.5 at. %. The optical band gap determined by UV-visible spectroscopy was found to be ~4.8 eV and indicates the high quality of the BaZrO<sub>3</sub> crystals grown by the optical floating zone technique. Dielectric anomalies were observed both at low and high temperatures, featuring inherent intrinsic

and extrinsic electrical properties. Raman spectra were recorded both at ambient temperature and at low temperature down to 4.2 K, revealing a relatively sharp second-order spectrum. The temperature evolution of the spectral signature has confirmed the absence of any structural phase transition.

Finally, BCTZ crystal growth attempts were carried out using the Top Seeded Solution Growth (TSSG) technique. Polycrystals and single crystals were obtained in the temperature range 1450 °C-1600 °C. The segregation coefficients of Ca and Zr elements during the growth of BCTZ compounds were investigated and found to be highly dependent on their initial concentrations in the liquid solution. In particular, the significant segregation coefficient of zirconium makes the growth of BCTZ crystals tricky, when targeting a steady composition in the vicinity of those corresponding to the phase convergence region. Furthermore, a spinodal decomposition phenomenon was evidenced, with the coexistence of two solid solutions with close compositions in BCTZ crystals. These two phenomena make it difficult to control precisely the final concentration of crystals, and are likely responsible for the low piezoelectric performance of the obtained BCTZ single crystals as compared to expectations.

Dielectric studies of the obtained crystals, have shown a relaxor behavior with high Zr content but most of BCTZ crystals reveal a normal ferroelectric behavior. More interestingly, an abnormal double-like PE hysteresis loop was observed in  $(\text{Ba}_{0.776}\text{Ca}_{0.224})(\text{Ti}_{0.911}\text{Zr}_{0.089})\text{O}_3$  sample, that was associated to an irreversible effect disappearing upon poling. Optical birefringence measurement did not enable the observation of the paraelectric phase to ferroelectric phase transition. No clear emergence of ferroelectric domains could be observed in the condition of the use of this experiment.

The principal perspective for future works based on those results can be divided into two parts.

In the case of BaZrO<sub>3</sub>, the availability of large, good quality single crystals opens the possibility for fundamental studies of its intrinsic properties, building on the preliminary results reported here on the dielectric anomalies, the optical properties and the Raman spectra. Notably, the Raman spectra display features that are sharper and more clearer than the literature, and a detailed work on its interpretation and a detailed assignment has been started, in combination with lattice dynamical calculations by DFT. Furthermore, a high-pressure Raman experiment has also been performed and has provided evidence for a phase transition from cubic to tetragonal at 11 GPa at room temperature, and a more detailed analysis is being carried out. Other physical measurements are also being discussed (lattice dynamics by inelastic neutron scattering and hyper-Raman spectroscopy, elastic properties by Brillouin spectroscopy etc.).

In the case of the BCTZ system, the improved understanding and control of both segregation and spinodal decomposition phenomena will be highly required. Further studies by decreasing the Zr and Ca contents could be undertaken in order to approach Ba(Zr<sub>0.2</sub>Ti<sub>0.8</sub>)O<sub>3</sub>-50(Ba<sub>0.7</sub>Ca<sub>0.3</sub>)TiO<sub>3</sub> composition in order to reach a giant piezoelectric response with relatively high Curie temperatures, that can compete with PZT.

## References

---

- [1]. Shirane, G. and Suzuki, K., *Crystal structure of Pb(Zr-Ti)O<sub>3</sub>*. Journal of the Physical Society of Japan, 1952. **7**(3): p. 333-333.
- [2]. Shirane, G., Suzuki, K., and Takeda, A., *Phase transitions in solid solutions of PbZrO<sub>3</sub> and PbTiO<sub>3</sub> (II) X-ray study*. Journal of the Physical Society of Japan, 1952. **7**(1): p. 12-18.
- [3]. Jaffe, B., Roth, R., and Marzullo, S., *Piezoelectric properties of lead zirconate-lead titanate solid-solution ceramics*. Journal of Applied Physics, 1954. **25**(6): p. 809-810.
- [4]. Jaffe, B., Roth, R., and Marzullo, S., *Properties of piezoelectric ceramics in the solid-solution series lead titanate-lead zirconate-lead oxide: tin oxide and lead titanate-lead hafnate*. Journal of research of the National Bureau of Standards, 1955. **55**(5): p. 239-254.
- [5]. Patrick, L., *Lead Toxicity, a review of the literature. Part I: Exposure, Evaluation, and treatment*. Alternative medicine review, 2006. **11**(1).
- [6]. Directive, R., *Directive 2002/95/EC of the European Parliament and of the Council of 27 January 2003 on the restriction of the use of certain hazardous substances in electrical and electronic equipment*. Official Journal of the European Union, 2003. **13**: p. L37.
- [7]. Regulation, E., *No 1907/2006 of the European Parliament and of the Council of 18 December 2006 concerning the Registration, Evaluation, Authorisation and Restriction of Chemicals (REACH), establishing a European Chemicals Agency, amending Directive, 1999*. **45**: p. 1-849.
- [8]. Goodship, V. and Stevels, A., *Waste electrical and electronic equipment (WEEE) handbook*. 2012: Elsevier.
- [9]. Park, S.-E. and Shrout, T. R., *Ultrahigh strain and piezoelectric behavior in relaxor based ferroelectric single crystals*. Journal of Applied Physics, 1997. **82**(4): p. 1804-1811.
- [10]. Rödel, J., Jo, W., Seifert, K. T. P., Anton, E.-M., Granzow, T., and Damjanovic, D., *Perspective on the development of lead-free piezoceramics*. Journal of the American Ceramic Society, 2009. **92**(6): p. 1153-1177.
- [11]. Rödel, J. and Li, J.-F., *Lead-free piezoceramics: Status and perspectives*. MRS Bulletin, 2018. **43**(8): p. 576-580.
- [12]. Liu, W. and Ren, X., *Large piezoelectric effect in Pb-free ceramics*. Physical Review Letters, 2009. **103**(25): p. 257602.
- [13]. Benabdallah, F., Simon, A., Khemakhem, H., Elissalde, C., and Maglione, M., *Linking large piezoelectric coefficients to highly flexible polarization of lead free BaTiO<sub>3</sub>-CaTiO<sub>3</sub>-BaZrO<sub>3</sub> ceramics*. Journal of Applied Physics, 2011. **109**(12): p. 124116.
- [14]. Wang, P., Li, Y., and Lu, Y., *Enhanced piezoelectric properties of (Ba<sub>0.85</sub>Ca<sub>0.15</sub>)(Ti<sub>0.9</sub>Zr<sub>0.1</sub>)O<sub>3</sub> lead-free ceramics by optimizing calcination and sintering temperature*. Journal of the European Ceramic Society, 2011. **31**(11): p. 2005-2012.

- [15]. Benabdallah, F., Veber, P., Prakasam, M., Viraphong, O., Shimamura, K., and Maglione, M., *Continuous cross-over from ferroelectric to relaxor state and piezoelectric properties of BaTiO<sub>3</sub>-BaZrO<sub>3</sub>-CaTiO<sub>3</sub> single crystals*. Journal of Applied Physics, 2014. **115**(14): p. 144102.
- [16]. Sun, Y., Liu, D., Li, Q., Shim, J., He, W., Fang, H., and Yan, Q., *Piezoelectric property of a tetragonal (Ba,Ca)(Zr,Ti)O<sub>3</sub> single crystal and its fine-domain structure*. ACS Applied Materials & Interfaces, 2018. **10**(15): p. 12847-12853.
- [17]. Liu, D., Shim, J., Sun, Y., Li, Q., and Yan, Q., *Growth of Ca, Zr co-doped BaTiO<sub>3</sub> lead-free ferroelectric single crystal and its room-temperature piezoelectricity*. AIP Advances, 2017. **7**(9): p. 095311.
- [18]. Zeng, Y., Zheng, Y., Tu, X., Lu, Z., and Shi, E., *Growth and characterization of lead-free Ba<sub>(1-x)</sub>CaxTi<sub>(1-y)</sub>Zr<sub>y</sub>O<sub>3</sub> single crystal*. Journal of Crystal Growth, 2012. **343**(1): p. 17-20.
- [19]. Zhao, X., Fang, B., Cao, H., Guo, Y., and Luo, H., *Dielectric and piezoelectric performance of PMN-PT single crystals with compositions around the MPB: influence of composition, poling field and crystal orientation*. Materials Science and Engineering: B, 2002. **96**(3): p. 254-262.
- [20]. Lim, L. C., Shanthi, M., Rajan, K. K., and Lim, C. Y. H., *Flux growth of high-homogeneity PMN-PT single crystals and their property characterization*. Journal of Crystal Growth, 2005. **282**(3): p. 330-342.
- [21]. Valasek, J., *Piezo-electric activity of Rochelle salt under various conditions*. Physical Review, 1922. **19**(5): p. 478.
- [22]. Rabe, K. M., Ahn, C. H., and Triscone, J.-M., *Physics of ferroelectrics: a modern perspective*. Vol. 105. 2007: Springer Science & Business Media.
- [23]. Landau, L. D., *On the theory of phase transitions*. Ukr. J. Phys., 1937. **11**: p. 19-32.
- [24]. Fatuzzo, E. and Merz, W. J., *Ferroelectricity*. Vol. 7. 1967: North-Holland Pub. Co.
- [25]. Lines, M. E. and Glass, A. M., *Principles and applications of ferroelectrics and related materials*. 2001: Oxford university press.
- [26]. Smolenskii, G., Isupov, V., Agranovskaya, A., and Popov, S., *Ferroelectrics with diffuse phase transitions*. Soviet Physics-Solid State, 1961. **2**(11): p. 2584-2594.
- [27]. Chu, F., Reaney, I. M., and Setter, N., *Role of defects in the ferroelectric relaxor lead scandium tantalate*. Journal of the American Ceramic Society, 1995. **78**(7): p. 1947-1952.
- [28]. Schulze, W. A., Biggers, J. V., and Cross, L. E., *Aging of dielectric dispersion in PLZT relaxor ceramics*. Journal of the American Ceramic Society, 1978. **61**(1-2): p. 46-49.
- [29]. Smolenskii, G. A. and Isupov, V. A., *Ferroelectric characteristics of solid solutions of barium stannate in barium titanate*. Zh. Tekh. Fiz, 1954. **24**: p. 1375.
- [30]. Maiti, T., Guo, R., and Bhalla, A. S., *Structure-property phase diagram of BaZr<sub>x</sub>Ti<sub>1-x</sub>O<sub>3</sub> system*. Journal of the American Ceramic Society, 2008. **91**(6): p. 1769-1780.
- [31]. Shvartsman, V. V. and Lupascu, D. C., *Lead-free relaxor ferroelectrics*. Journal of the American Ceramic Society, 2012. **95**(1): p. 1-26.
- [32]. Goldschmidt, V. M., *Die gesetze der krystallochemie*. Naturwissenschaften, 1926. **14**(21): p. 477-485.

- [33]. Abramov, Y. A., Tsirelson, V., Zavodnik, V., Ivanov, S., and Brown, I., *The chemical bond and atomic displacements in SrTiO<sub>3</sub> from X-ray diffraction analysis*. Acta Crystallographica Section B, 1995. **51**(6): p. 942-951.
- [34]. Megaw, H. D. and Templeton, D. H., *Crystal structures: A working approach*. Physics Today, 1974. **27**: p. 53.
- [35]. Glazer, A., *The classification of tilted octahedra in perovskites*. Acta Crystallographica Section B: Structural Crystallography and Crystal Chemistry, 1972. **28**(11): p. 3384-3392.
- [36]. Sasaki, S., Prewitt, C. T., Bass, J. D., and Schulze, W., *Orthorhombic perovskite CaTiO<sub>3</sub> and CdTiO<sub>3</sub>: structure and space group*. Acta Crystallographica Section C, 1987. **43**(9): p. 1668-1674.
- [37]. Megaw, H. D., *Origin of ferroelectricity in barium titanate and other perovskite-type crystals*. Acta Crystallographica, 1952. **5**(6): p. 739-749.
- [38]. Megaw, H. D. and Darlington, C., *Geometrical and structural relations in the rhombohedral perovskites*. Acta Crystallographica Section A: Crystal Physics, Diffraction, Theoretical and General Crystallography, 1975. **31**(2): p. 161-173.
- [39]. Glazer, A., *Simple ways of determining perovskite structures*. Acta Crystallographica Section A: Crystal Physics, Diffraction, Theoretical and General Crystallography, 1975. **31**(6): p. 756-762.
- [40]. Woodward, P. M., *Octahedral tilting in perovskites. I. Geometrical considerations*. Acta Crystallographica Section B, 1997. **53**(1): p. 32-43.
- [41]. Lufaso, M. W. and Woodward, P. M., *Jahn–Teller distortions, cation ordering and octahedral tilting in perovskites*. Acta Crystallographica Section B: Structural Science, 2004. **60**(1): p. 10-20.
- [42]. Howard, C. J. and Stokes, H. T., *Group-theoretical analysis of octahedral tilting in perovskites*. Acta Crystallographica Section B, 1998. **54**(6): p. 782-789.
- [43]. Woodward, P. M., *Octahedral tilting in perovskites. II. Structure stabilizing forces*. Acta Crystallographica Section B, 1997. **53**(1): p. 44-66.
- [44]. Rhodes, R., *Structure of BaTiO<sub>3</sub> at low temperatures*. Acta Crystallographica, 1949. **2**(6): p. 417-419.
- [45]. Kay, H. F. and Vousden, P., *XCV. Symmetry changes in barium titanate at low temperatures and their relation to its ferroelectric properties*. The London, Edinburgh, and Dublin Philosophical Magazine and Journal of Science, 1949. **40**(309): p. 1019-1040.
- [46]. Okazaki, A. and Suemune, Y., *The crystal structure of KCuF<sub>3</sub>*. Journal of the Physical Society of Japan, 1961. **16**(2): p. 176-183.
- [47]. Merz, W. J., *The electric and optical behavior of BaTiO<sub>3</sub> single-domain crystals*. Physical Review, 1949. **76**(8): p. 1221.
- [48]. Waser, R., Böttger, U., and Tiedke, S., *Polar oxides: properties, characterization, and imaging*. 2006: John Wiley & Sons.
- [49]. Kwei, G., Lawson, A., Billinge, S., and Cheong, S., *Structures of the ferroelectric phases of barium titanate*. The Journal of Physical Chemistry, 1993. **97**(10): p. 2368-2377.

- [50]. Mitsui, T., Nomura, S., Adachi, M., Harada, J., Ikeda, T., Nakamura, E., Sawaguchi, E., Shigenari, T., Shiozaki, Y., and Tatsuzaki, I., *Landolt-Börnstein*. Springer-Verlag, Berlin) Group, 1981. **3**: p. 153.
- [51]. Harada, J. and Axe, J., *J. Harada, JD Axe, and G. Shirane, Acta Crystallogr., Sect. A: Cryst. Phys., Diffr., Theor. Gen. Crystallogr.* 26, 608 (1970). *Acta Crystallogr., Sect. A: Cryst. Phys., Diffr., Theor. Gen. Crystallogr.*, 1970. **26**: p. 608.
- [52]. Khatib, D., Lifsal, L., Toumanari, A., and Kinase, W., *Theory of ferroelectricity in the tetragonal phase of PbTiO<sub>3</sub> due to the lattice deformation*. *Ferroelectrics Letters Section*, 1996. **22**(1-2): p. 9-13.
- [53]. Shirane, G. and Hoshino, S., *On the phase transition in lead titanate*. *Journal of the Physical Society of Japan*, 1951. **6**(4): p. 265-270.
- [54]. Shirane, G., Hoshino, S., and Suzuki, K., *X-ray study of the phase transition in lead titanate*. *Physical Review*, 1950. **80**(6): p. 1105.
- [55]. Hewat, A., *Soft modes and the structure, spontaneous polarization and Curie constants of perovskite ferroelectrics: tetragonal potassium niobate*. *Journal of Physics C: Solid State Physics*, 1973. **6**(6): p. 1074.
- [56]. Jaffe, B., Cook, W., and Jaffe, H., *Piezoelectric Ceramics*. Academic, New York, 1967: p. 135.
- [57]. Shirane, G., Sawaguchi, E., and Takeda, A., *On the phase transition in lead zirconate*. *Physical Review*, 1950. **80**(3): p. 485.
- [58]. Sawaguchi, E., *Ferroelectricity versus antiferroelectricity in the solid solutions of PbZrO<sub>3</sub> and PbTiO<sub>3</sub>*. *Journal of the physical society of Japan*, 1953. **8**(5): p. 615-629.
- [59]. Noheda, B., Gonzalo, J. A., Cross, L. E., Guo, R., Park, S. E., Cox, D. E., and Shirane, G., *Tetragonal-to-monoclinic phase transition in a ferroelectric perovskite: The structure of PbZr<sub>0.52</sub>Ti<sub>0.48</sub>O<sub>3</sub>*. *Physical Review B*, 2000. **61**(13): p. 8687-8695.
- [60]. Jaffe, H. and Berlincourt, D., *Piezoelectric transducer materials*. *Proceedings of the IEEE*, 1965. **53**(10): p. 1372-1386.
- [61]. Isupov, V., *Phases in the PZT Ceramics*. *Ferroelectrics*, 2002. **266**(1): p. 91-102.
- [62]. Davis, M., *Picturing the elephant: Giant piezoelectric activity and the monoclinic phases of relaxor-ferroelectric single crystals*. *Journal of Electroceramics*, 2007. **19**(1): p. 25-47.
- [63]. Takenaka, T. and Nagata, H., *Current status and prospects of lead-free piezoelectric ceramics*. *Journal of the European Ceramic Society*, 2005. **25**(12): p. 2693-2700.
- [64]. Directive, E., *Directive 2011/65/EU of the European Parliament and of the Council of 8 June 2011, on the restriction of the use of certain hazardous substances in electrical and electronic equipment (recast)*. *Official Journal of the European Communities*, 2011.
- [65]. Panda, P., *Environmental friendly lead-free piezoelectric materials*. *Journal of materials science*, 2009. **44**(19): p. 5049-5062.
- [66]. Rödel, J., Webber, K. G., Dittmer, R., Jo, W., Kimura, M., and Damjanovic, D., *Transferring lead-free piezoelectric ceramics into application*. *Journal of the European Ceramic Society*, 2015. **35**(6): p. 1659-1681.

- [67]. Shrout, T. R. and Zhang, S. J., *Lead-free piezoelectric ceramics: Alternatives for PZT?* Journal of Electroceramics, 2007. **19**(1): p. 113-126.
- [68]. Gupta, S., Maurya, D., Yan, Y., and Priya, S., *Development of KNN-based piezoelectric materials*, in *Lead-Free Piezoelectrics*. 2012, Springer. p. 89-119.
- [69]. Malič, B., Benčan, A., Rojac, T., and Kosec, M., *Lead-free piezoelectrics based on alkaline niobates: synthesis, sintering and microstructure*. Acta chimica slovenica, 2008. **55**(4).
- [70]. Liu, H., *Growth and characterization of lead-free (K,Na)NbO<sub>3</sub>-based piezoelectric single crystals*. 2016, Université de Bordeaux.
- [71]. Liu, H., Veber, P., Koruza, J., Rytz, D., Josse, M., Rödel, J., and Maglione, M., *Influence of Ta<sup>5+</sup> content on the crystallographic structure and electrical properties of [001]<sub>PC</sub>-oriented (Li,Na,K)(Nb,Ta)O<sub>3</sub> single crystals*. CrystEngComm, 2016. **18**(12): p. 2081-2088.
- [72]. Liu, H., Koruza, J., Veber, P., Rytz, D., Maglione, M., and Rödel, J., *Orientation-dependent electromechanical properties of Mn-doped (Li,Na,K)(Nb,Ta)O<sub>3</sub> single crystals*. Applied Physics Letters, 2016. **109**(15): p. 152902.
- [73]. Liu, H., Veber, P., Zintler, A., Molina-Luna, L., Rytz, D., Maglione, M., and Koruza, J., *Temperature-dependent evolution of crystallographic and domain structures in (K,Na,Li)(Ta,Nb)O<sub>3</sub> piezoelectric single crystals*. IEEE Transactions on Ultrasonics, Ferroelectrics, and Frequency Control, 2018.
- [74]. Liu, H., Veber, P., Rödel, J., Rytz, D., Fabritchnyi, P. B., Afanasov, M. I., Patterson, E. A., Frömling, T., Maglione, M., and Koruza, J., *High-performance piezoelectric (K,Na,Li)(Nb,Ta,Sb)O<sub>3</sub> single crystals by oxygen annealing*. Acta Materialia, 2018. **148**: p. 499-507.
- [75]. Prakasam, M., Veber, P., Viraphong, O., Etienne, L., Lahaye, M., Pechev, S., Lebraud, E., Shimamura, K., and Maglione, M., *Growth and characterizations of lead-free ferroelectric KNN-based crystals*. Comptes Rendus Physique, 2013. **14**(2-3): p. 133-140.
- [76]. Veber, P., Benabdallah, F., Liu, H., Buse, G., Josse, M., and Maglione, M., *Growth and characterization of lead-free piezoelectric single crystals*. Materials, 2015. **8**(11): p. 7962-7978.
- [77]. Elkechai, O., Manier, M., and Mercurio, J., *Na<sub>0.5</sub>Bi<sub>0.5</sub>TiO<sub>3</sub>-K<sub>0.5</sub>Bi<sub>0.5</sub>TiO<sub>3</sub> (NBT-KBT) system: A structural and electrical study*. physica status solidi (a), 1996. **157**(2): p. 499-506.
- [78]. Yang, Z., Liu, B., Wei, L., and Hou, Y., *Structure and electrical properties of (1-x)Bi<sub>0.5</sub>Na<sub>0.5</sub>TiO<sub>3</sub>-xBi<sub>0.5</sub>K<sub>0.5</sub>TiO<sub>3</sub> ceramics near morphotropic phase boundary*. Materials Research Bulletin, 2008. **43**(1): p. 81-89.
- [79]. Nagata, H., Yoshida, M., Makiuchi, Y., and Takenaka, T., *Large piezoelectric constant and high Curie temperature of lead-free piezoelectric ceramic ternary system based on bismuth sodium titanate-bismuth potassium titanate-barium titanate near the morphotropic phase boundary*. Japanese journal of applied physics, 2003. **42**(12R): p. 7401.
- [80]. Panda, P. and Sahoo, B., *PZT to lead free piezo ceramics: a review*. Ferroelectrics, 2015. **474**(1): p. 128-143.

- [81]. McQuarrie, M. and Behnke, F. W., *Structural and dielectric studies in the system (Ba,Ca)(Ti,Zr)O<sub>3</sub>*. Journal of the American Ceramic Society, 1954. **37**(11): p. 539-543.
- [82]. Ravez, J., Broustera, C., and Simon, A., *Lead-free ferroelectric relaxor ceramics in the BaTiO<sub>3</sub>-BaZrO<sub>3</sub>-CaTiO<sub>3</sub> system*. Journal of Materials Chemistry, 1999. **9**(7): p. 1609-1613.
- [83]. Benabdallah, F., *Evolution des propriétés diélectriques, ferroélectriques et électromécaniques dans le système pseudo-binaire (1-x)BaTi<sub>0.8</sub>Zr<sub>0.2</sub>O<sub>3</sub>-xBa<sub>0.7</sub>Ca<sub>0.3</sub>TiO<sub>3</sub>/Corrélations structures et propriétés*. 2013, Université Sciences et Technologies-Bordeaux I.
- [84]. Tian, Y., Wei, L., Chao, X., Liu, Z., and Yang, Z., *Phase transition behavior and large piezoelectricity near the morphotropic phase boundary of lead-free (Ba<sub>0.85</sub>Ca<sub>0.15</sub>)(Zr<sub>0.1</sub>Ti<sub>0.9</sub>)O<sub>3</sub> ceramics*. Journal of the American Ceramic Society, 2013. **96**(2): p. 496-502.
- [85]. Zhang, L., Zhang, M., Wang, L., Zhou, C., Zhang, Z., Yao, Y., Zhang, L., Xue, D., Lou, X., and Ren, X., *Phase transitions and the piezoelectricity around morphotropic phase boundary in Ba(Zr<sub>0.2</sub>Ti<sub>0.8</sub>)O<sub>3</sub>-x(Ba<sub>0.7</sub>Ca<sub>0.3</sub>)TiO<sub>3</sub> lead-free solid solution*. Applied Physics Letters, 2014. **105**(16): p. 162908.
- [86]. Keeble, D. S., Benabdallah, F., Thomas, P. A., Maglione, M., and Kreisel, J., *Revised structural phase diagram of (Ba<sub>0.7</sub>Ca<sub>0.3</sub>TiO<sub>3</sub>)-(BaZr<sub>0.2</sub>Ti<sub>0.8</sub>O<sub>3</sub>)*. Applied Physics Letters, 2013. **102**(9): p. 092903.
- [87]. Acosta, M., Novak, N., Jo, W., and Rödel, J., *Relationship between electromechanical properties and phase diagram in the Ba(Zr<sub>0.2</sub>Ti<sub>0.8</sub>)O<sub>3</sub>-x(Ba<sub>0.7</sub>Ca<sub>0.3</sub>)TiO<sub>3</sub> lead-free piezoceramic*. Acta Materialia, 2014. **80**: p. 48-55.
- [88]. Buse, G., Xin, C., Marchet, P., Borta-Boyon, A., Pham-Thi, M., Cabane, H., Veron, E., Josse, M., Velazquez, M., Lahaye, M., Lebraud, E., Maglione, M., and Veber, P., *Spinodal decomposition in lead-free piezoelectric BaTiO<sub>3</sub>-CaTiO<sub>3</sub>-BaZrO<sub>3</sub> crystals*. Crystal Growth & Design, 2018.
- [89]. Dhanaraj, G., Byrappa, K., Prasad, V., and Dudley, M., *Crystal growth techniques and characterization: An overview*, in *Handbook of Crystal Growth* Govindhan, Kullaiiah, Vishwanath, and Michael, Editors. 2010, Springer-Verlag Berlin Heidelberg: Berlin. p. 3-15.
- [90]. Fukuda, T. and Chani, V. I., *Shaped crystals: growth by micro-pulling-down technique*. Vol. 8. 2007: Springer Science & Business Media.
- [91]. Sekerka, R., *A stability function for explicit evaluation of the Mullins-Sekerka interface stability criterion*. Journal of Applied Physics, 1965. **36**(1): p. 264-268.
- [92]. Mullins, W. W. and Sekerka, R., *Stability of a planar interface during solidification of a dilute binary alloy*, in *Dynamics of Curved Fronts*. 1988, Elsevier. p. 345-352.
- [93]. Czochralski, J., *Ein neues Verfahren zur Messung der Kristallisationsgeschwindigkeit der Metalle*, in *Zeitschrift für Physikalische Chemie*. 1918. p. 219.
- [94]. Reed, T. B. and Pollard, E. R., *Tri-arc furnace for Czochralski growth with a cold crucible*. Journal of Crystal Growth, 1968. **2**(4): p. 243-247.

- [95]. V.I. Aleksandrav, V. V. O., H.M. Prokhorov, V.M. Tatarintsev, *A new method for obtaining refractory single crystals and fused ceramics*. Vestnik Acad. Nauk SSR, 1973. **12**: p. 29.
- [96]. Paun, M. S., *Single crystal growth of high melting oxide materials by means of induction skull melting*. 2015.
- [97]. Elwell, D., Scheel, H., and Kaldis, E., *Crystal growth from high temperature solutions*. Journal of The Electrochemical Society. Vol. 123. 1976.
- [98]. Aggarwal, M. D., Batra, A. K., Lal, R. B., Penn, B. G., and Frazier, D. O., *Bulk single crystals grown from solution on earth and in microgravity*, in *Handbook of Crystal Growth 2010*, Springer-Verlag Berlin Heidelberg: Berlin. p. 567.
- [99]. Goto, Y. and Cross, L., *Phase diagram of the BaTiO<sub>3</sub>-BaB<sub>2</sub>O<sub>4</sub> system and growth of BaTiO<sub>3</sub> crystals in the melt*. Yogyo-Kyokai-Shi, 1969. **77**(11): p. 355-357.
- [100]. Linz, A., Belruss, V., and Naiman, C., *Solution-grown perovskites*. J. electrochem. Soc., 1965. **112**(6): p. 60C.
- [101]. Belruss, V., Kalnajs, J., Linz, A., and Folweiler, R. C., *Top-seeded solution growth of oxide crystals from non-stoichiometric melts*. Materials Research Bulletin, 1971. **6**(10): p. 899-905.
- [102]. Pfann, W. G., *Principles of zone-melting*. JOM, 1952. **4**(7): p. 747-753.
- [103]. Balbashov, A. M. and Egorov, S. K., *Apparatus for growth of single crystals of oxide compounds by floating zone melting with radiation heating*. Journal of Crystal Growth, 1981. **52**: p. 498-504.
- [104]. Kimura, M. and Kitamura, K., *Floating zone crystal growth and phase equilibria: A review*. Journal of the American Ceramic Society, 1992. **75**(6): p. 1440-1446.
- [105]. Moest, B., Glebovsky, V. G., Brongersma, H. H., Bergmans, R. H., Denier van der Gon, A. W., and Semenov, V. N., *Study of Pd single crystals grown by crucibleless zone melting*. Journal of Crystal Growth, 1998. **192**(3): p. 410-416.
- [106]. Revcolevschi, A. and Jegoudez, J., *Growth of large high-Tc single crystals by the floating zone method: A review*. Progress in materials science, 1997. **42**(1-4): p. 321-339.
- [107]. Shindo, I., *Determination of the phase diagram by the slow cooling float zone method: The system MgO-TiO<sub>2</sub>*. Journal of Crystal Growth, 1980. **50**(4): p. 839-851.
- [108]. Cröll, A., *German association crystal growth (DGKK)*. Newsletter, 1997. **65**: p. 13.
- [109]. Saifi, M., Dubois, B., Vogel, E., and Thiel, F., *Growth of tetragonal BaTiO<sub>3</sub> single crystal fibers*. Journal of Materials Research, 1986. **1**(3): p. 452-456.
- [110]. Jiang, Y., Guo, R., and Bhalla, A. s., *Growth and properties of CaTiO<sub>3</sub> single crystal fibers*. Journal of Electroceramics, 1998. **2**(3): p. 199-203.
- [111]. Lai, Y. J., Chen, J. C., and Liao, K. C., *Investigations of ferroelectric domain structures in the MgO:LiNbO<sub>3</sub> fibers by LHPG*. Journal of Crystal Growth, 1999. **198-199**: p. 531-535.
- [112]. Luh, Y. S., Feigelson, R. S., Fejer, M. M., and Byer, R. L., *Ferroelectric domain structures in LiNbO<sub>3</sub> single-crystal fibers*. Journal of Crystal Growth, 1986. **78**(1): p. 135-143.

- [113]. Matsukura, M., Chen, Z., Adachi, M., and Kawabata, A., *Growth of potassium lithium niobate single-crystal fibers by the laser-heated pedestal growth method*. Japanese Journal of Applied Physics, 1997. **36**(9S): p. 5947.
- [114]. Haggerty, J., *Production of fibers by a floating zone fiber drawing technique*. 1972.
- [115]. Feigelson, R. S., *Pulling optical fibers*. Journal of Crystal Growth, 1986. **79**(1, Part 2): p. 669-680.
- [116]. Edmonds, W. R., *The reflexicon, a new reflective optical element, and some applications*. Applied Optics, 1973. **12**(8): p. 1940-1945.
- [117]. Remeika, J. P. and Jackson, W. M., *A method for growing barium titanate single crystals*. Journal of the American Chemical Society, 1954. **76**(3): p. 940-941.
- [118]. Eustache, H., *Production de monocristaux de titanate de baryum*. Comptes rendus hebdomadaires des seances de l'academie des sciences, 1957. **244**(8): p. 1029-1031.
- [119]. Nassau, K. and Broyer, A., *Application of Czochralski crystal-pulling technique to high-melting oxides*. Journal of the American Ceramic Society, 1962. **45**(10): p. 474-478.
- [120]. Brown, F. and Todt, W. H., *Floating-Zone BaTiO<sub>3</sub>: preparation and properties*. Journal of Applied Physics, 1964. **35**(5): p. 1594-1598.
- [121]. Arend, H. and Kihlberg, L., *Phase composition of reduced and reoxidized barium titanate*. Journal of the American Ceramic Society, 1969. **52**(2): p. 63-65.
- [122]. Schunemann, P., Temple, D. A., Hathcock, R. S., Tuller, H., Jenssen, H. P., Gabbe, D., and Warde, C., *Role of iron centers in the photorefractive effect in barium titanate*. JOSA B, 1988. **5**(8): p. 1685-1696.
- [123]. Jun, F. and Takeyo, T., *BaTiO<sub>3</sub> single crystal growth by travelling solvent floating zone technique*. Japanese Journal of Applied Physics, 1991. **30**(9S): p. 2391.
- [124]. Ito, F., Kitayama, K. i., and Tomomatsu, K., *Observation of the photorefractive effect in single-domain BaTiO<sub>3</sub> crystal fibers*. Applied Physics Letters, 1992. **61**(18): p. 2144-2146.
- [125]. Lee, Y.-C. and Chen, J.-C., *The effects of temperature distribution on the barium titanate crystal growth in an LHPG system*. Optical Materials, 1999. **12**(1): p. 83-91.
- [126]. Helal, M., Mori, T., and Kojima, S., *Softening of infrared-active mode of perovskite BaZrO<sub>3</sub> proved by terahertz time-domain spectroscopy*. Applied Physics Letters, 2015. **106**(18): p. 182904.
- [127]. Teague, J. R., Gerson, R., and James, W. J., *Dielectric hysteresis in single crystal BiFeO<sub>3</sub>*. Solid State Communications, 1970. **8**(13): p. 1073-1074.
- [128]. Kubel, F. and Schmid, H., *Structure of a ferroelectric and ferroelastic monodomain crystal of the perovskite BiFeO<sub>3</sub>*. Acta Crystallographica Section B: Structural Science, 1990. **46**(6): p. 698-702.
- [129]. Lebeugle, D., Colson, D., Forget, A., Viret, M., Bonville, P., Marucco, J. F., and Fusil, S., *Room-temperature coexistence of large electric polarization and magnetic order in BiFeO<sub>3</sub> single crystals*. Physical Review B, 2007. **76**(2): p. 024116.

- [130]. Lebeugle, D., Colson, D., Forget, A., and Viret, M., *Very large spontaneous electric polarization in BiFeO<sub>3</sub> single crystals at room temperature and its evolution under cycling fields*. Applied Physics Letters, 2007. **91**(2): p. 022907.
- [131]. Haumont, R., Saint-Martin, R., and Byl, C., *Centimeter-size BiFeO<sub>3</sub> single crystals grown by flux method*. Phase Transitions, 2008. **81**(9): p. 881-888.
- [132]. Ito, T., Ushiyama, T., Yanagisawa, Y., Kumai, R., and Tomioka, Y., *Growth of highly insulating bulk single crystals of multiferroic BiFeO<sub>3</sub> and their inherent internal strains in the domain-switching process*. Crystal Growth & Design, 2011. **11**(11): p. 5139-5143.
- [133]. Kay, H. F. and Bailey, P. C., *Structure and properties of CaTiO<sub>3</sub>*. Acta Crystallographica, 1957. **10**(3): p. 219-226.
- [134]. Watts, B. E., Dabkowska, H., and Wanklyn, B. M., *The flux growth of perovskites (CaTiO<sub>3</sub>, CdTiO<sub>3</sub>, SrZrO<sub>3</sub>, and LaGaO<sub>3</sub>, PrGaO<sub>3</sub>, NdGaO<sub>3</sub>)*. Journal of Crystal Growth, 1989. **94**(1): p. 125-130.
- [135]. Nomura, S. and Sawada, S., *Ferroelectricity of PbTiO<sub>3</sub>*. Todai Rikoken Houkoku, 1952. **6**: p. 191.
- [136]. Rogers, H. H., *The growing of lead titanate crystals and some of their properties*. 1952, MASSACHUSETTS INST OF TECH CAMBRIDGE LAB FOR INSULATION RESEARCH.
- [137]. Kobayashi, J., *Growing of ferroelectric PbTiO<sub>3</sub> crystals*. Journal of Applied Physics, 1958. **29**(5): p. 866-867.
- [138]. Bhide, V. G., Deshmukh, K. G., and Hegde, M. S., *Ferroelectric properties of PbTiO<sub>3</sub>*. Physica, 1962. **28**(9): p. 871-876.
- [139]. Remeika, J. P. and Glass, A. M., *The growth and ferroelectric properties of high resistivity single crystals of lead titanate*. Materials Research Bulletin, 1970. **5**(1): p. 37-45.
- [140]. Grabmaier, B. C., *PbTiO<sub>3</sub> grown from the melt*. Ferroelectrics, 1976. **13**(1): p. 501-503.
- [141]. Oka, K., Unoki, H., Yamaguchi, H., and Takahashi, H., *Crystal growth of PbTiO<sub>3</sub> by the top-seeded solution-growth method*. Journal of Crystal Growth, 1996. **166**(1): p. 380-383.
- [142]. Maffei, N. and Rossetti, G. A., *Float-Zone growth and properties of ferroelectric lead titanate*. Journal of Materials Research, 2011. **19**(3): p. 827-833.
- [143]. Jona, F., Shirane, G., and Pepinsky, R., *Optical study of PbZrO<sub>3</sub> and NaNbO<sub>3</sub> single crystals*. Physical Review, 1955. **97**(6): p. 1584.
- [144]. Scott, B. A. and Burns, G., *Crystal growth and observation of the ferroelectric phase of PbZrO<sub>3</sub>*. Journal of the American Ceramic Society, 1972. **55**(7): p. 331-333.
- [145]. Whatmore, R. W. and Glazer, A. M., *Structural phase transitions in lead zirconate*. Journal of Physics C: Solid State Physics, 1979. **12**(8): p. 1505.
- [146]. Roleder, K. and Dee, J., *The defect-induced ferroelectric phase in thin PbZrO<sub>3</sub> single crystals*. Journal of Physics: Condensed Matter, 1989. **1**(8): p. 1503.
- [147]. Glazer, A., Roleder, K., and Dec, J., *Structure and disorder in single-crystal lead zirconate, PbZrO<sub>3</sub>*. Acta Crystallographica Section B: Structural Science, 1993. **49**(5): p. 846-852.

- [148]. Tokukō, S., Shuzo, H., and Gisaku, O., *Growth of strontium titanate single crystals from molten salts*. Japanese Journal of Applied Physics, 1968. **7**(4): p. 358.
- [149]. Robbins, C. R., *Growth of strontium titanate from a silica flux*. Journal of Crystal Growth, 1968. **2**(6): p. 402-404.
- [150]. Aleksandrov, V., Vishnyakova, M., Voron'ko, Y. K., Kalabukhova, V., Lomonova, E., Myzina, V., and Osiko, V., *Growing SrTiO<sub>3</sub> monocrystals by the Czochralski method from a cold container*. Izv. Akad. Nauk SSSR, Neorg. Mater, 1983. **19**(1): p. 104-107.
- [151]. Reyes Ardila, D., Andreetta, M., Cuffini, S., Hernandez, A., Andreetta, J., and Mascarenhas, Y., *Single-crystal SrTiO<sub>3</sub> fiber grown by laser heated pedestal growth method: influence of ceramic feed rod preparation in fiber quality*. Materials Research, 1998. **1**(1): p. 11-17.
- [152]. Nabokin, P. I., Souptel, D., and Balbashov, A. M., *Floating zone growth of high-quality SrTiO<sub>3</sub> single crystals*. Journal of Crystal Growth, 2003. **250**(3): p. 397-404.
- [153]. Souptel, D., Behr, G., and Balbashov, A. M., *SrZrO<sub>3</sub> single crystal growth by floating zone technique with radiation heating*. Journal of Crystal Growth, 2002. **236**(4): p. 583-588.
- [154]. Chiang, Y.-M., Birnie, D. P., Kingery, W. D., and Newcomb, S., *Physical ceramics: principles for ceramic science and engineering*. Vol. 409. 1997: Wiley New York.
- [155]. Sinclair, D. C., Skakle, J. M., Morrison, F. D., Smith, R. I., and Beales, T. P., *Structure and electrical properties of oxygen-deficient hexagonal BaTiO<sub>3</sub>*. Journal of Materials Chemistry, 1999. **9**(6): p. 1327-1331.
- [156]. Wada, S., Suzuki, S., Noma, T., Suzuki, T., Osada, M., Kakihana, M., Park, S.-E., Cross, L. E., and Shrout, T. R., *Enhanced piezoelectric property of barium titanate single crystals with engineered domain configurations*. Japanese journal of applied physics, 1999. **38**(9S): p. 5505.
- [157]. Ouladdiaf, B., Archer, J., McIntyre, G., Hewat, A., Brau, D., and York, S., *OrientExpress: A new system for Laue neutron diffraction*. Physica B: Condensed Matter, 2006. **385**: p. 1052-1054.
- [158]. Becker, J. S. and Dietze, H.-J., *Inorganic trace analysis by mass spectrometry*. Spectrochimica Acta Part B: Atomic Spectroscopy, 1998. **53**(11): p. 1475-1506.
- [159]. Reed, S. J. B., *Electron microprobe analysis and scanning electron microscopy in geology*. 2005: Cambridge University Press.
- [160]. Mahoney, C. M., *Cluster secondary ion mass spectrometry: principles and applications*. Vol. 44. 2013: John Wiley & Sons.
- [161]. Stevie, F., *Secondary ion mass spectrometry: Applications for depth profiling and surface characterization*. 2015: Momentum Press.
- [162]. Bhatt, R., Bhaumik, I., Ganesamoorthy, S., Karnal, A., Swami, M., Patel, H., and Gupta, P., *Urbach tail and bandgap analysis in near stoichiometric LiNbO<sub>3</sub> crystals*. physica status solidi (a), 2012. **209**(1): p. 176-180.
- [163]. Sawyer, C. B. and Tower, C. H., *Rochelle salt as a dielectric*. Physical Review, 1930. **35**(3): p. 269-273.
- [164]. Raman, C. V. and Krishnan, K. S., *A new type of secondary radiation*. Nature, 1928. **121**: p. 501.

- [165]. Wilson, E. B., Decius, J. C., and Cross, P. C., *Molecular vibrations: the theory of infrared and Raman vibrational spectra*. 1955: Courier Corporation.
- [166]. Ferraro, J. R., *Introductory Raman spectroscopy*. 2003: Academic press.
- [167]. Porto, S., Giordmaine, J., and Damen, T., *Depolarization of Raman scattering in calcite*. Physical Review, 1966. **147**(2): p. 608.
- [168]. Merker, L., *Synthesis of calcium titanate single crystals by Flame Fusion Technique*. Journal of the American Ceramic Society, 1962. **45**(8): p. 366-369.
- [169]. Liu, X. and Liebermann, R. C., *X-ray powder diffraction study of CaTiO<sub>3</sub> perovskite at high temperatures*. Physics and Chemistry of Minerals, 1993. **20**(3): p. 171-175.
- [170]. Gillet, P., Guyot, F., Price, G. D., Tournier, B., and Le Cleach, A., *Phase changes and thermodynamic properties of CaTiO<sub>3</sub>. Spectroscopic data, vibrational modelling and some insights on the properties of MgSiO<sub>3</sub> perovskite*. Physics and Chemistry of Minerals, 1993. **20**(3): p. 159-170.
- [171]. Guennou, M., Bouvier, P., Krikler, B., Kreisel, J., Haumont, R., and Garbarino, G., *High-pressure investigation of CaTiO<sub>3</sub> up to 60 GPa using X-ray diffraction and Raman spectroscopy*. Physical Review B, 2010. **82**(13): p. 134101.
- [172]. Linz Jr, A. and Herrington, K., *Electrical and optical properties of synthetic calcium titanate crystal*. The Journal of Chemical Physics, 1958. **28**(5): p. 824-825.
- [173]. Boldú O, J., Abraham, M., and Boatner, L., *EPR characterization of Er<sup>3+</sup> and Yb<sup>3+</sup> in single crystals of synthetic perovskite (CaTiO<sub>3</sub>)*. The Journal of chemical physics, 1987. **86**(10): p. 5267-5272.
- [174]. Godefroy, G., Lompre, P., Dumas, C., and Arend, H., *Pure and doped barium titanate. Crystal growth and chemical composition*. Materials Research Bulletin, 1977. **12**(2): p. 165-169.
- [175]. DeVRIES, R. C., *Observations on growth of BaTiO<sub>3</sub> crystals from KF solutions*. Journal of the American Ceramic Society, 1959. **42**(11): p. 547-558.
- [176]. Guennou, M., Bouvier, P., Chen, G. S., Dkhil, B., Haumont, R., Garbarino, G., and Kreisel, J., *Multiple high-pressure phase transitions in BiFeO<sub>3</sub>*. Physical Review B, 2011. **84**(17): p. 174107.
- [177]. Genet, F., Loridant, S., Ritter, C., and Lucazeau, G., *Phase transitions in BaCeO<sub>3</sub>: neutron diffraction and Raman studies*. Journal of Physics and Chemistry of Solids, 1999. **60**(12): p. 2009-2021.
- [178]. Iliev, M., Abrashev, M., Lee, H.-G., Popov, V., Sun, Y., Thomsen, C., Meng, R., and Chu, C., *Raman spectroscopy of orthorhombic perovskitelike YMnO<sub>3</sub> and LaMnO<sub>3</sub>*. Physical Review B, 1998. **57**(5): p. 2872.
- [179]. G. Fateley, W., T. McDevitt, N., and F. Bentley, F., *Infrared and raman selection rules for lattice vibrations: the correlation method*. Vol. 25. 1971. 155-173.
- [180]. McMillan, P. and Ross, N., *The Raman spectra of several orthorhombic calcium oxide perovskites*. Physics and Chemistry of Minerals, 1988. **16**(1): p. 21-28.
- [181]. Balachandran, U. and Eror, N. G., *Laser-induced Raman scattering in calcium titanate*. Solid State Communications, 1982. **44**(6): p. 815-818.
- [182]. Hirata, T., Ishioka, K., and Kitajima, M., *Vibrational spectroscopy and X-Ray diffraction of perovskite compounds Sr<sub>1-x</sub>M<sub>x</sub>TiO<sub>3</sub> (M= Ca, Mg; 0 ≤ x ≤ 1)*. Journal of Solid State Chemistry, 1996. **124**(2): p. 353-359.

- [183]. Qin, S., Wu, X., Seifert, F., and Becerro, A. I., *Micro-Raman study of perovskites in the  $\text{CaTiO}_3\text{-SrTiO}_3$  system*. Journal of the Chemical Society, Dalton Transactions, 2002(19): p. 3751-3755.
- [184]. Vassen, R., Cao, X., Tietz, F., Basu, D., and Stöver, D., *Zirconates as new materials for thermal barrier coatings*. Journal of the American Ceramic Society, 2000. **83**(8): p. 2023-2028.
- [185]. Davies, P. K., Tong, J., and Negas, T., *Effect of ordering-induced domain boundaries on low-loss  $\text{Ba}(\text{Zn}_{1/3}\text{Ta}_{2/3})\text{O}_3\text{-BaZrO}_3$  perovskite microwave dielectrics*. Journal of the American Ceramic Society, 1997. **80**(7): p. 1727-1740.
- [186]. Akbarzadeh, A., Kornev, I., Malibert, C., Bellaiche, L., and Kiat, J., *Combined theoretical and experimental study of the low-temperature properties of  $\text{BaZrO}_3$* . Physical Review B, 2005. **72**(20): p. 205104.
- [187]. Acosta, M., Novak, N., Rojas, V., Patel, S., Vaish, R., Koruza, J., Rossetti Jr., G. A., and Rödel, J.,  *$\text{BaTiO}_3$ -based piezoelectrics: Fundamentals, current status, and perspectives*. Applied Physics Reviews, 2017. **4**(4): p. 041305.
- [188]. Amoroso, D., Cano, A., and Ghosez, P., *First-principles study of  $(\text{Ba,Ca})\text{TiO}_3$  and  $\text{Ba}(\text{Ti,Zr})\text{O}_3$  solid solutions*. Physical Review B, 2018. **97**(17): p. 174108.
- [189]. Nahas, Y., Akbarzadeh, A., Prokhorenko, S., Prosandeev, S., Walter, R., Kornev, I., Íñiguez, J., and Bellaiche, L., *Microscopic origins of the large piezoelectricity of leadfree  $(\text{Ba,Ca})(\text{Zr,Ti})\text{O}_3$* . Nature Communications, 2017. **8**: p. 15944.
- [190]. Yang, T., Ke, X., and Wang, Y., *Mechanisms Responsible for the Large Piezoelectricity at the Tetragonal-Orthorhombic Phase Boundary of  $(1-x)\text{BaZr}_{0.2}\text{Ti}_{0.8}\text{O}_3\text{-xBa}_{0.7}\text{Ca}_{0.3}\text{TiO}_3$  System*. Scientific Reports, 2016. **6**: p. 33392.
- [191]. Azad, A.-M., Subramaniam, S., and Dung, T. W., *On the development of high density barium metazirconate ( $\text{BaZrO}_3$ ) ceramics*. Journal of Alloys and Compounds, 2002. **334**(1): p. 118-130.
- [192]. Deyra, L., Maillard, A., Maillard, R., Sangla, D., Salin, F., Balembois, F., Kokh, A., and Georges, P., *Impact of  $\text{BaB}_2\text{O}_4$  growth method on frequency conversion to the deep ultra-violet*. Solid State Sciences, 2015. **50**: p. 97-100.
- [193]. Helal, M. A., Mori, T., and Kojima, S., *Terahertz time-domain spectroscopy and Raman scattering studies of incipient ferroelectric  $\text{BaZrO}_3$* . Ferroelectrics, 2016. **499**(1): p. 107-114.
- [194]. Chemarin, C., Rosman, N., Pagnier, T., and Lucazeau, G., *A high-pressure Raman study of mixed perovskites  $\text{BaCe}_x\text{Zr}_{1-x}\text{O}_3$  ( $0 \leq x \leq 1$ )*. Journal of Solid State Chemistry, 2000. **149**(2): p. 298-307.
- [195]. Mączka, M., Szymborska-Małek, K., Gağor, A., and Majchrowski, A., *Growth and characterization of acentric  $\text{BaHf}(\text{BO}_3)_2$  and  $\text{BaZr}(\text{BO}_3)_2$* . Journal of Solid State Chemistry, 2015. **225**: p. 330-334.
- [196]. Jing-Lin, Y., Guo-Chang, J., Huai-Yu, H., Yong-Quan, W., Hui, C., and Kuang-Di, X., *Temperature-dependent Raman spectra and microstructure of barium metaborate crystals and its melts*. Chinese physics letters, 2002. **19**(2): p. 205.
- [197]. Ishigame, M. and Sakurai, T., *Temperature dependence of the Raman spectra of  $\text{ZrO}_2$* . Journal of the American Ceramic Society, 1977. **60**(7-8): p. 367-369.
- [198]. Albino, M., Veber, P., Castel, E., Velázquez, M., Schenk, K., Chapuis, G., Lahaye, M., Pechev, S., Maglione, M., and Josse, M., *Growth and characterization of*

- centimeter-sized Ba<sub>2</sub>LaFeNb<sub>4</sub>O<sub>15</sub> crystals from high-temperature solution under a controlled atmosphere.* European Journal of Inorganic Chemistry, 2013. **2013**(15): p. 2817-2825.
- [199]. Hornebecq, V., Gravereau, P., Chaminade, J. P., and Lebraud, E., *BaZr(BO<sub>3</sub>)<sub>2</sub>: a non-centrosymmetric dolomite-type superstructure.* Materials Research Bulletin, 2002. **37**(13): p. 2165-2178.
- [200]. Jacobson, N. S., *Thermodynamic properties of some metal oxide-zirconia systems.* 1989, National aeronautics and space administration cleveland oh lewis research center.
- [201]. Fisher, J., Kim, D.-H., Lee, S., Nguyen, D., and Lee, J.-S., *Reactive sintering of BaY<sub>0.1</sub>Zr<sub>0.9</sub>O<sub>3-δ</sub> proton conducting ceramics with CuO liquid phase sintering aid.* Vol. 14. 2013. 703~706.
- [202]. Gonçalves, M. D., Maram, P. S., Muccillo, R., and Navrotsky, A., *Enthalpy of formation and thermodynamic insights into yttrium doped BaZrO<sub>3</sub>.* Journal of Materials Chemistry A, 2014. **2**(42): p. 17840-17847.
- [203]. Velázquez, M., Veber, P., Buşe, G., Petit, Y., Goldner, P., Jubera, V., Rytz, D., Jaffres, A., Peltz, M., Wesemann, V., Aschehough, P., and Aka, G., *Spectroscopic properties of newly flux grown and highly Yb<sup>3+</sup>-doped cubic RE<sub>2</sub>O<sub>3</sub> (RE=Y, Gd, Lu) laser crystals.* Optical Materials, 2015. **39**: p. 258-264.
- [204]. Veber, P., Velázquez, M., Gadret, G., Rytz, D., Peltz, M., and Decourt, R., *Flux growth at 1230 °C of cubic Tb<sub>2</sub>O<sub>3</sub> single crystals and characterization of their optical and magnetic properties.* CrystEngComm, 2015. **17**(3): p. 492-497.
- [205]. Veber, P., Velázquez, M., Jubera, V., Péchev, S., and Viraphong, O., *Flux growth of Yb<sup>3+</sup>-doped RE<sub>2</sub>O<sub>3</sub> (RE=Y, Lu) single crystals at half their melting point temperature.* CrystEngComm, 2011. **13**(16): p. 5220-5225.
- [206]. Haumont, R., Saint-Martin, R., Chaigneau, J., Devant, M., Hermet, J., Neela Sekhar, B., Uesu, Y., Itoh, M., and Kiat, J. M., *Growth of quantum paraelectric La<sub>1/2</sub>Na<sub>1/2</sub>TiO<sub>3</sub> single crystals using optical floating zone technique.* Journal of Crystal Growth, 2011. **321**(1): p. 36-39.
- [207]. Kouchaksaraie, L. S., *Theoretical calculation of electrical and optical properties of BaZrO<sub>3</sub>.* World Academy of Science, Engineering and Technology, International Journal of Mathematical, Computational, Physical, Electrical and Computer Engineering, 2011. **5**(11): p. 1680-1683.
- [208]. Yang, X., Wang, Y., Song, Q., Chen, Y., and Xue, Y. H., *Pressure effects on structural, electronic, elastic, and optical properties of cubic and tetragonal phases of BaZrO<sub>3</sub>.* Acta Physica Polonica, A., 2018. **133**(5).
- [209]. Cavalcante, L. S., Sczancoski, J. C., Longo, V. M., De Vicente, F. S., Sambrano, J. R., de Figueiredo, A. T., Dalmaschio, C. J., Li, M. S., Varela, J. A., and Longo, E., *Intense violet–blue photoluminescence in BaZrO<sub>3</sub> powders: A theoretical and experimental investigation of structural order–disorder.* Optics Communications, 2008. **281**(14): p. 3715-3720.
- [210]. Terki, R., Feraoun, H., Bertrand, G., and Aourag, H., *Full potential calculation of structural, elastic and electronic properties of BaZrO<sub>3</sub> and SrZrO<sub>3</sub>.* Physica status solidi (b), 2005. **242**(5): p. 1054-1062.

- [211]. Bennett, J. W., Grinberg, I., and Rappe, A. M., *Effect of symmetry lowering on the dielectric response of BaZrO<sub>3</sub>*. Physical Review B, 2006. **73**(18): p. 180102.
- [212]. Alay-e-Abbas, S. M., Nazir, S., and Shaukat, A., *Formation energies and electronic structure of intrinsic vacancy defects and oxygen vacancy clustering in BaZrO<sub>3</sub>*. Physical Chemistry Chemical Physics, 2016. **18**(34): p. 23737-23745.
- [213]. Volkova, H., *Ferroelectric perovskite oxides for photovoltaics and photocatalysis*. 2018, MINES, ParisTech.
- [214]. Lee, S., Levi, R. D., Qu, W., Lee, S. C., and Randall, C. A., *Band-gap nonlinearity in perovskite structured solid solutions*. Journal of Applied Physics, 2010. **107**(2): p. 023523.
- [215]. Stetson, H. and Schwartz, B., *Dielectric properties of zirconates*. Journal of the American Ceramic Society, 1961. **44**(8): p. 420-421.
- [216]. Salce, B., Gravil, J., and Boatner, L., *Disorder and thermal transport in undoped KTaO<sub>3</sub>*. Journal of Physics: Condensed Matter, 1994. **6**(22): p. 4077.
- [217]. Bidault, O., Maglione, M., Actis, M., Kchikech, M., and Salce, B., *Polaronic relaxation in perovskites*. Physical Review B, 1995. **52**(6): p. 4191.
- [218]. Samara, G. A., *The relaxational properties of compositionally disordered ABO<sub>3</sub> perovskites*. Journal of Physics: Condensed Matter, 2003. **15**(9): p. R367.
- [219]. Colomban, P. and Slodczyk, A., *Raman intensity: an important tool in the study of nanomaterials and nanostructures*. Acta Physica Polonica-Series A General Physics, 2009. **116**(1): p. 7.
- [220]. Nilsen, W. and Skinner, J., *Raman spectrum of strontium titanate*. The Journal of Chemical Physics, 1968. **48**(5): p. 2240-2248.
- [221]. Nilsen, W. and Skinner, J., *Raman spectrum of potassium tantalate*. The Journal of Chemical Physics, 1967. **47**(4): p. 1413-1418.
- [222]. Saha, S., Cao, B.-C., Motapothula, M., Cong, C.-X., Sarkar, T., Srivastava, A., Sarkar, S., Patra, A., Ghosh, S., Ariando, Coey, J. M. D., Yu, T., and Venkatesan, T., *Magnetic modes in rare earth perovskites: A magnetic-field-dependent inelastic light scattering study*. Scientific Reports, 2016. **6**: p. 36859.
- [223]. Glaister, R. and Kay, H., *An investigation of the cubic-hexagonal transition in barium titanate*. Proceedings of the Physical Society, 1960. **76**(5): p. 763.
- [224]. Redfern, S. A., *High-temperature structural phase transitions in perovskite*. Journal of Physics: Condensed Matter, 1996. **8**(43): p. 8267.
- [225]. Rudolph, P., *Defect formation during crystal growth from the melt*, in *Springer Handbook of Crystal Growth*. 2010, Springer. p. 159-201.
- [226]. Scheel, H. J. and Fukuda, T., *Crystal growth technology*. 2005: John Wiley & Sons.
- [227]. Jackson, K. A., *Kinetic Processes: crystal growth, diffusion, and phase transformations in materials*. 2006: John Wiley & Sons.
- [228]. Jackson, K., *Kinetic Processes: Crystal Growth. Diffusion, and Phase Transformations in Materials* Wiley Verlag, 2004.
- [229]. BUSE, G., XIN, C., Marchet, P., Borta-Boyon, A., Pham-Thi, M., Cabane, H., Véron, E., Josse, M., Velazquez, M., and Lahaye, M., *Spinodal decomposition in lead-free piezoelectric BaTiO<sub>3</sub>-CaTiO<sub>3</sub>-BaZrO<sub>3</sub> crystals*. Crystal Growth & Design.
- [230]. Garrett, M. and Mnushkina, I., *Techniques for top-seeded solution growth of BaTiO<sub>3</sub>*. Journal of crystal growth, 1996. **166**(1-4): p. 550-557.

- [231]. DeVRIES, R. C. and ROY, R., *Phase equilibria in the system BaTiO<sub>3</sub>-CaTiO<sub>3</sub>*. Journal of the American Ceramic Society, 1955. **38**(4): p. 142-146.
- [232]. Barbosa, L., Ardila, D. R., and Andreetta, J., *Crystal growth of congruent barium calcium titanate by LHPG*. Journal of Crystal Growth, 2001. **231**(4): p. 488-492.
- [233]. Liu, H., Li, Q., Li, Y., Luo, N., Shim, J., Gao, J., Yan, Q., Zhang, Y., and Chu, X., *Structure evolution and electrical properties of Y<sup>3+</sup>-doped Ba<sub>1-x</sub>Ca<sub>x</sub>Zr<sub>0.07</sub>Ti<sub>0.93</sub>O<sub>3</sub> ceramics*. Journal of the American Ceramic Society, 2014. **97**(7): p. 2076-2081.
- [234]. Gurvinderjit, S., Indranil, B., Ganesamoorthy, S., Bhatt, R., Karnal, A. K., Tiwari, V. S., and Gupta, P. K., *Electro-caloric effect in 0.45BaZr<sub>0.2</sub>Ti<sub>0.8</sub>O<sub>3</sub>-0.55Ba<sub>0.7</sub>Ca<sub>0.3</sub>TiO<sub>3</sub> single crystal*. Applied Physics Letters, 2013. **102**(8): p. 082902.
- [235]. Merz, W. J., *Double Hysteresis Loop of BaTiO<sub>3</sub> at the Curie Point*. Physical Review, 1953. **91**(3): p. 513.
- [236]. Ren, X., *Large electric-field-induced strain in ferroelectric crystals by point-defect-mediated reversible domain switching*. Nature Materials, 2004. **3**: p. 91.
- [237]. Zhang, L. and Ren, X., *In situ observation of reversible domain switching in aged Mn-doped BaTiO<sub>3</sub> single crystals*. Physical Review B, 2005. **71**(17): p. 174108.
- [238]. Zhang, L. and Ren, X., *Aging behavior in single-domain Mn-doped BaTiO<sub>3</sub> crystals: implication for a unified microscopic explanation of ferroelectric aging*. Physical Review B, 2006. **73**(9): p. 094121.
- [239]. Zhang, L., Chen, W., and Ren, X., *Large recoverable electrostrain in Mn-doped (Ba,Sr)TiO<sub>3</sub> ceramics*. Applied Physics Letters, 2004. **85**(23): p. 5658-5660.
- [240]. Yuan, G., Yang, Y., and Or, S. W., *Aging-induced double ferroelectric hysteresis loops in BiFeO<sub>3</sub> multiferroic ceramic*. Applied physics letters, 2007. **91**(12): p. 122907.
- [241]. Yun, S., *Double hysteresis loop in BaTiO<sub>3</sub>-based ferroelectric ceramics*. 2011.